ITER PHYSICS BASIS

CHAPTER 6: PLASMA AUXILIARY HEATING AND CURRENT DRIVE

ITER Expert Group on Energetic Particles, Heating, and Current Drive*
ITER Physics Basis Editors**

ITER EDA, Garching Work Site, D-85748 Garching, GERMANY

ABSTRACT. Heating and current drive (H&CD) systems must fulfill several roles in ITER operating scenarios: heating through the H-mode transition and to ignition, plasma burn control, current drive and current profile control in steady-state scenarios, and control of MHD instabilities. They must also perform ancillary functions, such as assisting plasma start-up and wall conditioning. It is recognized that no one system can satisfy all of these requirements with the degree of flexibility which ITER will require. Four heating and current drive systems are therefore under consideration for ITER: electron cyclotron waves (ECW) at a principal frequency of 170GHz, fast waves (FW) operating in the range 40-70MHz (ion cyclotron waves, ICW), lower hybrid waves (LHW) at 5GHz, and neutral beam injection using negative ion beam technology for operation at 1MeV energy. It is likely that several of these systems will be employed in parallel. The systems have been chosen on the basis of the maturity of physics understanding and operating experience in current experiments and on the feasibility of applying the relevant technology to ITER. Here the fundamental physics describing the interaction of these heating systems with the plasma is reviewed, the relevant experimental results in the exploitation of the heating and current drive capabilities of each system is discussed, key aspects of its application to ITER are outlined, and the major technological developments required in each area are summarized.

LIST OF AUTHORS FOR CHAPTER 6

* ITER Expert Group on Energetic Particles, Heating, and Current Drive:
J. Jacquinot[1], S. Putvinski, G. Bosia, A. Fukuyama[2], S. Konovalov[3], T. Nagashima[4], W.M. Nevins[5], K.A. Razumova[3], F. Romanelli[6], K. Tobita[4], K. Ushigusa[4], J. van Dam[7], V. Vdovin[3], S. Zweben[8]

Additional contributing authors: M. Makowski, R. Koch[9], J.-G. Wégrowe[10], V.V. Alikaev[3], B. Beaumont[10], A. Bécoulet[10], S. Bernabei[8], V.P. Bhatnagar[11], S. Brémond[10], M.D. Carter[12], C.D. Challis[1], A. Côté[13], D.A. D'Ippolito[14], F. Engelmann[15], L.-G. Eriksson[10], N. Fujisawa, G. Giruzzi[10], C. Gormezano[1], R. Harvey[16], J. Heikkinen[17], T. Hellsten[18], Y. Ikeda[4], T.T.C. Jones[1], H. Kimura[4], B. Lloyd[19], T. Luce[20], D. Moreau[10], O. Naito[4], F. Nguyen[10], J.-M. Noterdaeme[21], W. Ott[21], C.C. Petty[20], A. Polevoi[3], R. Prater[20], J. Rogers[22], F. Santini[6], F.-X. Söldner[1], D. Stork[1], E. Thompson, G Tonon[10], A. Tuccillo[6], E. Westerhof[23], H. Zohm[24]

** ITER Physics Basis Editors: F.W. Perkins, D.E. Post, N. A. Uckan[12], M. Azumi[4], D.J. Campbell[15], N. Ivanov[3], N.R. Sauthoff[8], M. Wakatani[25]

Additional contributing Editor: E. Righi[15]

IPB-CHAPTER 6

PLASMA AUXILIARY HEATING AND CURRENT DRIVE

TABLE OF CONTENTS

6. PLASMA AUXILIARY HEATING AND CURRENT DRIVE..... 5

6.1. INTRODUCTION 5
6.2. ECRF PHYSICS.....9
6.2.1. Introduction.....9
6.2.2. Heating and Current Drive 10
6.2.2.1. Propagation and absorption..... 10
6.2.2.2. Up-shifted/down-shifted ECCD scenarios..... 11
6.2.2.3. Codes..... 12
6.2.2.4. Experimental results 13
6.2.2.5. Transport studies..... 14
6.2.3. Plasma Heating and H-Mode Access 15
6.2.4. Start-Up and Wall Conditioning..... 15
6.2.5. MHD Stabilization with ECRF 17
6.2.6. Other Results..... 20
6.2.6.1. ELMs..... 20
6.2.6.2. Effect of ECH on sawteeth 20
6.2.7. Application to ITER..... 21
6.2.7.1. Technological issues..... 21
6.2.7.2. Heating and current drive in the ITER reference discharge 22
6.3. FAST WAVE HEATING AND CURRENT DRIVE..... 24
6.3.1. Introduction..... 24
6.3.2. Physics and Performance of Power Coupling..... 26
6.3.3. Modeling 29
6.3.4. Heating Scenarios and Database..... 31
6.3.4.1. General ICRH database..... 32
6.3.4.2. Scenarios for basic ITER applications..... 33
6.3.4.3. ICRF in advanced scenarios..... 35
6.3.4.4. Other ICRH scenarios..... 36
6.3.5. Current Drive 37
6.3.6. Plasma Production 38
6.3.7. The Functions of the ICRF System in ITER..... 39
6.4. LOWER-HYBRID HEATING AND CURRENT DRIVE..... 41
6.4.1. Introduction and Basic Physics..... 41
6.4.2. LH Current Drive Efficiency..... 44
6.4.3. Current Profile Control and Improved Plasma Performance with LHCD..... 46
6.4.4. LH Power Coupling 48
6.4.5. LHW and H-mode Plasmas..... 50
6.4.6. Interaction of LHW with Fast Ions..... 50
6.4.7. Theoretical Progress and Model Validation 51
6.4.8. Heating and Current Drive in ITER 53
6.4.9. Technological Issues..... 54
6.5. NEUTRAL BEAM HEATING AND CURRENT DRIVE..... 55
6.5.1. Introduction..... 55
6.5.2. Interaction of Neutral Beams with Plasmas 57
6.5.2.1. Neutral beam ionization cross-section..... 58
6.5.3. Neutral Beam Current Drive 63

6.5.3.1. Introduction.....63
6.5.3.2. Theory of NB current drive.....64
6.5.3.3. NB current drive experiments.....67
6.5.3.4. ITER predictions for NB current drive.....71
6.5.4. Plasma Rotation Induced by Neutral Beam.....71
6.5.4.1. Momentum transfer from beam ions to bulk plasma.....72
6.5.4.2. Observed time variation of plasma rotation with NB.....73
6.5.4.3. Projected toroidal rotation from NBI momentum input in ITER.....73
6.5.5. Negative-Ion Based Neutral Beam Development.....74
6.5.5.1. N-NB on JT-60U.....74
6.5.5.2. Development program.....75
6.5.6. Conclusion.....76
REFERENCES.....78
LIST OF TABLES.....91
LIST OF FIGURES.....91
AUTHORS' AFFILIATIONS.....94

6. PLASMA AUXILIARY HEATING AND CURRENT DRIVE

6.1. INTRODUCTION

The need for external heating power in addition to the Ohmic heating power resulting from the tokamak plasma current has been recognized since the early days of tokamak research. As plasma temperature rises, the plasma resistivity decreases as $T_e^{3/2}$ and the role played by the Ohmic heating gradually becomes less important. The auxiliary heating systems in ITER have to perform several tasks. The fundamental role is to deliver sufficient central heating power to access the H-mode confinement regime; to control the plasma temperature as the density is increased to bring the plasma to the desired operating point; and to control excursions about this operating point after it has been achieved. There are secondary requirements such as non-inductive central current drive (> 0.2 MAm^{-2}) and an off-axis current drive capability (> 2 MA) for current profile control. Auxiliary heating systems are also required to heat non-fusion plasmas in early operating phases (for example, while commissioning the divertor target plates) and to achieve a "soft-landing" during the current termination phase while avoiding density-limit disruptions (see Chapter 3.3 for a discussion of disruptive density limits). Capabilities to control sawteeth or $m = 2$, $n = 1$ modes, to induce plasma rotation in order to avoid locked modes and to stabilize resistive tearing instabilities are other desirable features. There are also requirements for plasma initiation, start-up assist, and wall conditioning (see Chapter 8).

Four auxiliary heating and current drive methods are considered for ITER. These include electromagnetic waves in three frequency ranges (i) the Electron Cyclotron Resonance Frequency (ECRF), (ii) the Ion Cyclotron Resonance Frequency (ICRF), and (iii) the Lower Hybrid Resonance Frequency (LHRF). In addition we consider heating and current drive by (iv) Neutral Beam Injection (NBI). Auxiliary power systems based on these four heating methods have been successfully used on large, medium and small tokamaks world-wide. Salient features of these

systems are summarized in Table 6.1-I. Power levels close to ITER requirements have already been demonstrated on present large tokamaks. General considerations applying to ITER conditions are given below, while the specific physics basis for each system will be found in the following sections.

(a) Central Power Deposition. The fundamental role of auxiliary heating is to initiate the fusion burn. For diffusive heat transport the maximum confinement, and therefore the minimum power requirement is obtained with central heating. Hence, the auxiliary heating power should be deposited near the plasma center. However, due to the mixing effects of sawteeth in the ITER reference scenario, it is sufficient to deposit power within the sawtooth inversion radius. Three out of four ITER candidate heating methods: ECRF, ICRF and NBI are capable of providing central plasma heating for the reference operation scenarios for ITER. At the reference plasma parameters the LH waves can penetrate only to the outer part of the plasma cross section, $r > 0.5a$, and hence the major objective of LHRF in ITER is off-axis current drive and current profile control.

(b) Current Drive. Steady-state operation of the tokamak requires that at least 20 % of the plasma current is provided by an external source, the remainder being generated by the plasma itself (the bootstrap current). In addition, this current needs to be generated at 2 locations: on (or near) the axis in order to control the central q value, and far off-axis to control plasma stability. The on-axis requirement can easily be met by ECRF, ICRF and NBI. The off-axis requirement involves driving a larger current (> 2 MA) at a lower electron temperature, which implies operating close to the theoretical CD efficiency limit. LHRF and ECRF are considered for this task.

(c) Plasma rotation. It is known from present experiments and theoretical considerations that plasma rotation is beneficial and can play an important role in suppression of plasma instabilities such as locked and error field modes, ideal MHD, tearing modes and others. It is also believed that rotational shear can improve plasma confinement and can help in the transition to the advanced confinement modes which are envisioned to be candidates for steady state operation in ITER (see Chapter 2) - though the relative contributions of external momentum input and local pressure gradients require further clarification. Nevertheless, the provision of plasma rotation is an

important goal for ITER auxiliary systems. It is clear that tangential NBI injection provides momentum input to the plasma core (and has been used, for example, to suppress mode locking and error field modes). Hence NBI is capable of driving toroidal plasma rotation in ITER. Among RF systems only ICRH is proven by present experiments to be capable of inducing a significant plasma rotation. However, the mechanisms of ICRF driven plasma rotation are not fully understood and hence the extrapolation for ITER of ICRH rotation drive capability is questionable.

(d) Direct Ion Heating. The H-mode power threshold is proportional to the plasma density [1] (see also Chapter 2.4 for a discussion of the H-mode power threshold). In ITER operation, it is proposed to produce the transition to H-mode at lower densities so that an L- to H-mode transition can be achieved with no more than 100 MW of auxiliary power. As the density is increased, the H-mode can be maintained because of additional heating from fusion α-particles. In the initial stages, when the α-particle power is small, power directly applied to ions is more effective in increasing the ion stored energy, because power given to electrons can be lost by radiation or radial transport before it is collisionally transferred to the ions.

(e) Future Developments. The above candidate auxiliary heating systems all require further developments to meet ITER needs (see e.g. [2]). ECRF requires development of power sources and windows and a demonstration of off-axis current drive efficiency on medium sized tokamaks. ICRF requires development of ELM-tolerant coupling systems. It is worth noting that significant recent progress has been made in the testing of ITER scenarios in D-T plasmas [3]. LHRF requires launcher development, in particular with a view to coupling in H-mode plasmas. Negative-ion beams require development of sources and power supply systems and further tests on tokamak plasmas both to confirm the current drive efficiency expected in the electron drag regime and to assess the influence of instabilities driven by fast ions.

Undoubtedly, the power required to bring ITER to ignition can be provided by several existing methods. This has been clearly demonstrated on present large tokamaks which reached the required ignition temperature in a D-T environment with both NBI and ICRH methods. However, there is still a need to improve the efficiency and multi-tasking capabilities of the

auxiliary heating systems. With regard to experimental demonstrations, emphasis should be placed on simulating the operating conditions of ITER, namely, regimes with low plasma rotation, moderate ion heating and low particle fueling; and in developing steady-state scenarios which require efficient current drive systems and feedback control of the current density profile.

Table 6.1-I: Salient Features of the Four Auxiliary Heating Systems in use on Tokamaks

System			Frequency/ Energy	Max Inner Power coupled to Plasma	Overall system efficiency	Development/ demonstration required	Remarks
ECRF		Demonstrated in tokamaks	28-157 GHz	2.8 MW, 0.2 s	30-40 %	Power sources and windows, off-axis CD	Provides off-axis CD
		ITER needs	150-170 GHz	50 MW, s-s			
ICRF		Demonstrated in tokamaks	25-120 MHz	22 MW, 3 s (L-mode) 16.5 MW, 3 s (H-mode)	50-60 %	ELM tolerant system,	Provides ion heating and smaller ELMs
		ITER needs	40-75 MHz	50 MW, s-s			
LHRF		Demonstrated in tokamaks	1.3-8 GHz	2.5 MW, 120 s 10 MW, 0.5 s	45-55 %	Launcher, coupling to H-mode	provides off-axis CD
		ITER needs	5 GHz	50 MW, s-s			
NBI	$+v_e$ Ion	Demonstrated in tokamaks	80-140 keV	40 MW, 2 s 20 MW, 8 s	35-45 %	None	not applicable to ITER
		ITER needs	None	None			
	$-v_e$ Ion	Demonstrated in tokamaks	0.35 MeV	5.2 MW, D^-, 0.8 s (from 2 sources)			
		ITER needs	1 MeV	50 MW, s-s	~ 37 %	System, Tests on Tokamak, plasma CD	provides rotation

s-s = steady-state

6.2. ECRF PHYSICS

6.2.1. Introduction

The physics of electron cyclotron (EC) heating and current drive (ECCD) is well developed in both experiment and theory [4,5]. Experiments have been performed over a period of more than two decades in mirror machines, tokamaks [6], and stellarators. These experiments have demonstrated effective plasma heating, with reliable access to the H-mode. Experiments have also demonstrated current drive, plasma start-up, and control of sawteeth, ELMs, locked modes, as well as control of $m = 2$ modes and some types of disruption [7]. EC waves have also proven to be a useful tool for transport studies.

The fundamental properties of EC wave absorption and propagation lead directly to its application as an auxiliary heating and current drive mechanism in fusion plasmas. Electron cyclotron waves can be launched in vacuum and propagate directly into the plasma without attenuation or interaction with the edge. Consequently, the launching structure does not have to be in close proximity to the plasma. The waves continue to propagate smoothly within the plasma until they encounter the resonance and are locally absorbed. Absorption is generally complete and does not lead to the formation of an energetic tail or other non-linear effects. This localized absorption property allows control over the deposition profile and lends this heating method particular flexibility for such applications as on- and off-axis heating and current drive, MHD control, and transport studies.

This heating method is limited primarily by refractive effects as the density cut-off is approached. Low frequency density fluctuations of sufficient amplitude can also lead to scattering and localized random refraction of the wave. Localization of the deposition for these and other reasons discussed below is generally well above the theoretical minimum of a few wavelengths, being of the order of ~ 0.05 of the minor radius. However, this is more than sufficient for heating

and current drive applications envisioned and much more localized in comparison to other heating methods.

In ITER, the heating and current drive functions can be accomplished over the desired operating range using fixed frequency (170 GHz) sources by launching elliptically polarized ordinary-mode (OM) waves from the low-field-side (LFS) of the torus, provided that a modest toroidal steering capability is provided. Steerable injection accommodates the wide variety of plasma equilibria possible in ITER, particularly in the case of advanced tokamak equilibria. Start-up assist can be accomplished using lower frequency sources and does not require steerable injection. Dedicated systems may also be needed for other applications, such as stabilization of neo-classical tearing modes, resulting in specialized system requirements for modulation capability, frequency, peak power, etc.

6.2.2. Heating and Current Drive

6.2.2.1. Propagation and absorption

Two mechanisms are responsible for absorption of electron cyclotron waves [8, 9] by the plasma. Interaction of the wave and particle occurs in the presence of an elliptically polarized electric field rotating in the same direction as the electron at a frequency close to the electron gyrofrequency. A second means of interaction is provided by the Lorentz force arising from the magnetic field component transverse to the static toroidal magnetic field. If the parallel electron velocity, $v_{e||} \neq 0$, then a resonance energy exchange occurs. In both cases the perpendicular energy of the resonant particles is increased.

The resonance condition for the n^{th} harmonic ordinary-mode (OM) is $\omega = n\Omega_e / \gamma + k_{||} v_{e||}$, where $\Omega_e(R)$ is the cyclotron frequency, γ is the relativistic mass factor, and $k_{||}$ is the parallel wavenumber. The width of the absorption region is affected by the angle of incidence, through the broadening of the resonance due to the relativistic Doppler effect, by the electron temperature, and

by the divergence of the wave beam. For normal propagation, the absorption layer is a few centimetres in width, but it can be increased if desired by increasing the beam divergence. For oblique toroidal propagation, as used for current drive applications, the absorption region not only broadens but shifts toward lower magnetic fields. Oblique poloidal propagation also shifts the absorption region in this direction.

Current drive experiments at the fundamental and second harmonic EC resonances have been performed at a number of facilities, for example DIII-D [10], Tosca, W7-AS, T-10 [11], WT3, and JFT-2M. It was shown (DIII-D, T-10) that for the fundamental harmonic and power deposition in the central region, ECCD efficiency is in accordance with the theoretical predictions. In experiments on the W7-AS stellarator, in which there is effectively no toroidal electric field, agreement between experiment and theory was found, taking into account the effect of trapped particles, both for fundamental and second harmonics [12].

Many of the potential applications of ECH waves require off-axis current drive. Here only a few experiments [13] have been carried out and further work is needed to completely validate the models. The current drive efficiency generally decreases with increasing minor radius due to the increasing trapped electron fraction [14].

6.2.2.2. Up-shifted/down-shifted ECCD scenarios

Electron Cyclotron Current Drive (ECCD) is based on the generation of an asymmetric collisionality by the selective heating of electrons moving in a given direction [15]. As a result, the collisionality or resistivity is reduced and a net toroidal current is generated. Two schemes are possible: down-shifted and up-shifted. In the down-shifted scheme, power is absorbed on the high-field-side of the resonance mostly by electrons with $N_{||}p_{||} < 0$, while in the up-shifted scheme, electrons with $N_{||}p_{||} > 0$ are heated on the low-field-side [16]. Here, $N_{||}$ is the parallel index of refraction and $p_{||}$ is the parallel momentum. Both schemes rely on absorption of the power on one side of the resonance and thus require a large optical depth to achieve high efficiency.

The best option for down-shifted frequencies is with extraordinary mode (XM) injection from the high-field-side (HFS) of the resonance. In the case of up-shifted frequencies, the XM is generally cut-off and cannot reach the plasma center, leaving ordinary mode (OM) launch as the only up-shifted option. Top OM launch suffers from a large sensitivity to the injection angle as well as significant second harmonic absorption. Low-field-side OM launch, in contrast, provides good control over the deposition location with significantly reduced second harmonic absorption. Note that simultaneous first and second harmonic absorption is generally unsuitable, since in this case currents are driven at two different locations and in opposite directions [17].

Radial control of the location of the power deposition is obtained through oblique launch of the wave in the toroidal direction. The resonance can be shifted by a large fraction of the plasma cross section [18, 5] by varying $k_{||}$, the limit being due to relativistic effects and reduced wave damping. Additional use of poloidal steering is generally desirable.

6.2.2.3. Codes

The theory of ECCD is highly advanced, and ray tracing/Fokker-Planck codes based on first principles can accurately predict the propagation and absorption of EC waves in a plasma. For current drive or high power density cases, Fokker-Planck codes such as CQL3D [19], ORGAY and BANDIT-3D [20], have proven very effective in understanding experimental results quantitatively. These codes have been benchmarked [21] in several ways. Examples are the calculation of the neoclassical electric conductivity for which analytic expressions exist, or of the low power, linear ECCD efficiency for which adjoint calculations are also available [14]. Another example is a calculation for the parameters of the ECCD experiment in DIII-D [10, 21]. Good agreement is obtained both between code predictions and experiment and between the different codes themselves. These codes provide a predictive capability for present day experiments as well as giving confidence for the applications of EC waves foreseen in ITER.

The code predictions show that non-thermal effects are not to be expected in ITER. Such effects would be expected for $P(\mathrm{MW/m^{-3}})/[n(10^{19}\ \mathrm{m^{-3}})]^2 > 0.5$ [18], whereas the EC power density in ITER will remain well below this critical value.

6.2.2.4. Experimental results

ECCD has been achieved in several tokamaks both in the down-shifted scheme using oblique HFS injection of fundamental X-mode (DIII-D [10], Compass-D [22], RTP [23]) and in the up-shifted scheme using oblique LFS injection of either second harmonic X-mode (T-10 [24], RTP [25]) or fundamental O-mode (T-10 [11]). The last is the proposed scheme for ECCD in ITER. Results from these experiments are difficult to compare directly, since full non-inductive current drive is generally not obtained and different techniques are used to determine the EC driven currents: either by comparison of loop voltages in co- and counter-drive discharges, $I_{\mathrm{ECCD}} = I_{\mathrm{p}}\,(V_{\mathrm{cnt}} - V_{\mathrm{co}})/(V_{\mathrm{cnt}} + V_{\mathrm{co}})$, or by the difference of the sum of the calculated inductive and bootstrap currents and the total plasma current, $I^*_{\mathrm{ECCD}} = I_{\mathrm{p}} - I_{\mathrm{cond}} - I_{\mathrm{boot}}$. The driven currents, I^*_{ECCD}, obtained by the latter analysis contain, besides the purely EC driven current, a synergistic contribution which is caused by an increase in the conductivity due to the EC generated nonthermal electrons.

Maximum measured normalized efficiencies, η_{20} (10^{20} $\mathrm{AW^{-1}m^{-2}}$), range from $\eta_{20} = 0.01$ (RTP, $T_e \approx 3$ keV, up- or down-shifted) and $\eta_{20} = 0.015$ (DIII-D, $T_e \approx 3$ keV, down-shifted including synergy) to $\eta_{20} = 0.03$ (T-10, $T_e \approx 7$ keV, up-shifted). The CD efficiency is defined as $\eta_{20} = \langle n_{e20} \rangle\ I_{\mathrm{ECCD}}\ R_o/P_{\mathrm{launched}}$ where $\langle n_{e20} \rangle$ is the volume averaged electron density in units of 10^{20} $\mathrm{m^{-3}}$, I_{ECCD} is the net current driven by the launched EC wave power, R_o is the major radius measured at the magnetic axis of the target plasma, and P_{launched} is the launched EC wave power. The higher efficiency in T-10 is mainly due to the higher temperature reached in these experiments. These efficiencies are in general agreement with theoretical expectations. The major parametric dependencies as predicted by linear theory have been verified [11], though definitive experimental

data on the quasi-linear power dependence is lacking. Further confirmation of ECCD theory comes from detailed experiments in the W7-AS stellarator [26, 27]. The measurements in DIII-D and T-10, when adjusted by means of code calculations to flatten density profiles and lower Z_{eff}, as expected for ITER, are in line with the temperature dependence of the efficiency as predicted for ITER [28]: this leads to the prediction of a maximum efficiency for ECCD in ITER of $\eta_{20} = 0.3$ at $T_e(0) = 30$ keV (see Fig. 6.2-1).

Full non-inductive ECCD has only been achieved on T-10 in the scheme most relevant to ITER [11]. The low plasma current in these discharges (75 kA) resulted in high β_p such that the bootstrap current accounted for a large fraction of the plasma current (~50 kA) as seen in Fig. 6.2-1, where a comparison of predicted on-axis current drive and experimental results is shown. The curves (marked by O and Δ) are simulations showing the influence of temperature profiles and divergence of the wave due to diffractive effects. Experimental results from T-10 and DIII-D are also shown (marked by ∇ and square box). Corrections for density profiles and Z_{eff} have been made in both cases [28].

6.2.2.5. Transport studies

Because of the highly localized nature of the absorption of electron cyclotron waves, ECH has been used as a perturbative technique to study heat transport in plasmas on a many devices [29-35]. A relatively small power can generate small perturbations in the electron temperature at a desired location on the radial profile of the temperature, and phase sensitive detection can provide information on the location of the heating and on the transport of heat from the deposition site. Detection averaged over a record of many cycles of the perturbation can greatly improve the signal to noise ratio, thereby reducing the requirement on the power used for the perturbation. This technique has been employed on several devices to study the power deposition profile and transport.

6.2.3. Plasma Heating and H-Mode Access

Experiments in many tokamaks using ECH have demonstrated effective plasma heating [6]. Global confinement in the L-mode with solely ECH auxiliary heating has been shown to be consistent with the ITER-89P scaling relation. In direct comparisons with neutral beam heating on the DIII-D tokamak, ECH has been shown to have the same global heating efficiency as neutral beams at the same power, although the range of power for ECH has been limited to a small fraction of the available neutral beam power in experiments so far. For a true benchmark, ECH power at least in the range 5 to 10 MW is needed. Reliable access to the H-mode has also been demonstrated in tokamaks [36-38] and in a stellarator [39] using ECH power alone. The power threshold for the transition from L-mode to H-mode under ECH was found to be about the same for H-mode induced by NBI on the DIII-D tokamak [36]. The improvement in confinement above the L-mode scaling is a full factor of 2 in the DIII-D experiments [40]. The scaling of confinement in the H-mode with ECH has not been studied in depth so far, as the available ECH power has only been slightly above the threshold power. However, some studies do exist, such as those in ELMy H-mode on COMPASS-D generated by using both on- and off-axis ECH [41].

6.2.4. Start-Up and Wall Conditioning

EC wave power has been used effectively for pre-ionization and start-up assist in many tokamaks experiments [4, 42] and is used routinely for plasma production in stellarators [4]. In early tokamak experiments, ECRH pre-ionization typically led to a reduction of a factor of 2–5 in the initial loop voltage together with a somewhat smaller reduction in the overall flux consumption during the current rise phase. Features common to many of these early experiments [4, 42] include an insensitivity to the wave launching scenario (i.e., inboard/outboard launch, XM/OM polarization), effective preionization at the second harmonic and a weak dependence on the resonance location. The effective use of the OM for preionization has been attributed to the

depolarizing effect of wall reflections. Various detailed theoretical descriptions of ECRH preionization in tokamaks have been developed [43-45].

A systematic series of experiments was carried out on DIII-D in order to study low voltage start-up with and without ECRH to provide data which could be readily extrapolated to ITER [42]. It was shown that for low voltage start-up, ECRH not only leads to improved start-up reliability, but permits operation over a greatly extended range of prefill pressure and stray magnetic field and leads to reduced runaway generation. ECRH-assisted start-up with an electric field of ~ 0.15 V/m was demonstrated.

For ECRH-assisted start-up in ITER, the power and pulse length requirements will be essentially determined by the need to ensure burnthrough, i.e. complete ionization of hydrogen and the transition to high ionization states of impurities. A 0-D code (with inclusion of some 1-D effects), incorporating a non-equilibrium impurity model has been developed to study start-up [46]. It has been concluded that control of the deuterium density is the key factor for ensuring successful start-up in ITER. Because of the large ratio of vessel volume to plasma volume during start-up, fueling by the volume outside the ionization region may be an important effect and the role of neutral screening is also crucial. Without ECRH assist, successful start-up may only be possible over a restricted range of parameters. Although there remain uncertainties over exact requirements, it has been estimated that ~3 MW of *absorbed* ECRH power will ensure reasonably robust start-up for a broad range of conditions with up to 5% beryllium impurity [46]. Higher powers are required for carbon impurity, even 5 MW being marginal under some conditions. An ECRH pulse length of a few seconds is adequate to ensure burnthrough.

For the proposed start-up scenario, in which a poloidal field null is established close to the outboard limiter, several frequencies in the range 90–140 GHz must be provided to accommodate the range of toroidal fields envisaged in ITER. OM injection from the LFS may be envisaged. Due to the low initial electron temperature the OM is only weakly damped, but by launching the power at an oblique toroidal angle significant conversion of the OM to the XM will occur upon

reflection from the inner wall. After several reflections over 75% of the launched power is expected to be absorbed by the plasma [46].

ECRH discharge cleaning is one of the wall conditioning methods foreseen in ITER to reduce and control outgassing of impurities and hydrogenic fuel from the plasma facing components, for the achievement of clean and stable plasma operation. The effectiveness of ECRH discharge cleaning has been demonstrated in a number of devices [47]. Both the main ECRH heating system (170 GHz) and the ECRH start-up system may be utilized for this application, but steady state operation of the start-up system would be required in this case.

6.2.5. MHD Stabilization with ECRF

Tearing modes are resistive MHD instabilities that lead to a reconnection of the nested flux surfaces and produce so-called magnetic islands. These lead to regions of enhanced heat diffusivity, producing flat spots in the temperature profile that reduce the stored energy. This mechanism is one of the phenomena possibly limiting β in long pulse collisionless tokamak discharges [48] (see also section 3.2.3). Here, the drive for the instability mainly comes from the reduction of bootstrap current as the island develops and the pressure flattens at the O-point. Besides their role in the β-limit, tearing modes also play a major role in the density limit disruption, when, through excessive edge cooling, the equilibrium current profile shrinks and the free energy in the poloidal magnetic field leads to the formation of magnetic islands [49].

ECRF can be applied in two ways to act on the stability of the plasma. The first involves the shaping of the equilibrium current profile in the vicinity of the resonant surface to decrease the available free energy for the island to grow. The free energy is given by the stability index, $\Delta'(W) = (\psi'/\psi)_{rres+W/2} - (\psi'/\psi)_{rres-W/2}$, where ψ is the poloidal flux, ψ' is its derivative with respect to minor radius, and W is the width of the island: $\Delta'(W) > 0$ means instability, whereas in the case $\Delta'(W) < 0$ the equilibrium configuration resists tearing and there is a saturation width for the neoclassical island, $W_s \sim \beta_p/(-\Delta')$. As this scheme relies on a purely toroidal current, the

injection can be continuous and the method is referred to as the "DC scheme". The other method is to inject directly into the O-point of the island and thus restore the lost current locally. This requires phased injection and is referred to as the "AC-scheme". Current can also be driven outside the island, which will reduce the efficiency of either scheme. Note that heating will also lead to an increase of the local current density through enhanced conductivity.

For current gradient driven tearing modes, the driving energy comes from the gradient in the equilibrium current profile. The DC scheme creates a local peak of positive toroidal current centered around the resonant surface. This decreases the stability index at the resonant surface when no island is present [50]. The DC scheme has successfully been demonstrated in experiments in JFT-2M [37] and T-10 [51]. The AC scheme works on the non-linear stability of the mode, and thus the requirement in current and power differs from the DC scheme by a factor which tends to favor the AC scheme. The effect of phased current drive in a magnetic island has successfully been demonstrated in ASDEX Upgrade [52] and COMPASS-D (where the phase feedback loop was closed, whereas no radial deposition feedback was applied [53]).

Note that for both schemes, one does not have to maximize the total driven current, but rather the number I_{ECCD}/d^2, where d is the ECCD deposition width, because the stabilizing effect depends on gradient of the current density. This allows injection of the ECCD power at relatively small angles from perpendicular, because both driven current and deposition width increase with angle. With the constraint that the absorption has to be at the $q = 2$ surface, calculations find a maximum of the driven current density between 10^o and 20^o at a frequency of 130 GHz. However, the absolute value of the driven current strongly depends on the assumed T_e at the $q = 2$ surface.

For neoclassical tearing modes in the resistive β-limit, the condition $\Delta' < 0$ prevails. With the DC scheme, one makes use of the fact that the critical β_p for non-linear instability scales linearly with Δ'. In ITER, it is expected that the $m = 2$ mode will be the most critical instability for the β-limit. This scheme is in principle capable of avoiding neoclassical tearing modes. The AC scheme again works on the non-linear stability. Note that, similar to the case of the current

gradient driven tearing mode, only a small injection angle, and therefore narrow deposition width, is needed. For the reasons stated above, the AC scheme is favored over the DC scheme. Calculations indicate that stabilization will require a driven current of the order of one percent of the total current [54].

A potential problem for the AC scheme is that the stabilization efficiency rapidly decreases when the deposition width exceeds the island width. In practice, this may mean that the island cannot be completely removed by the AC scheme, but rather that it will be reduced to an island width of the order of the deposition width. This also favors a small injection angle and therefore small deposition width. For complete magnetic island removal, however, other means would have to be invoked.

A special case occurs when the magnetic islands, due to interactions with the conducting vacuum vessel wall and error fields arising from imperfections of the coil system, slow down and reach a stationary (locked) position. In this case, the AC scheme can only work at full efficiency if the EC wave antenna is located in front of an island O-point. As has been shown, counter-drive in the X-point will be less effective in removing the island. Thus, it is advisable to ensure injection from more than one port, or to compensate the error field using external coils that can be used to change the phase of the locked mode. Otherwise, the stabilization of this kind of locked mode is not different from a rotating one.

A different kind of locked mode occurs when external error fields penetrate the plasma and produce a magnetic island. In this case, the equilibrium current profile is stable to tearing, i.e. $\Delta'(W) < 0$. This kind of locked mode has successfully been removed in COMPASS-D [5] using ECCD in the island O-point. It was shown that above a critical heating power, the island spins up to its natural rotation frequency and decays, due to the fact that $\Delta'(W) < 0$.

6.2.6. Other Results

6.2.6.1. ELMs

Another MHD instability occurring in tokamak discharges is the Edge Localized Mode (ELM) [55] (see also section 3.2.6). Experiments on DIII-D have shown that ECRF heating of the plasma edge gives rise to a noticeable effect on the type I ELM frequency [56]: heating inside the separatrix increased the ELM frequency (as does any rise in heat flux through the separatrix in the case of type I ELMs), whereas heating outside the separatrix decreased the ELM frequency. This may either be due to a decreased resistivity, and thus a longer current diffusion time, or a softening of the pressure gradient across the separatrix.

No experiments exist for the case of type II ELM control. However, ECH applied to type III ELMs was shown to reduce the ELM frequency, consistent with the other forms of heating power [57]. As the transition from type III to type I ELMs seems to be connected to increasing edge temperature, one might envisage a separate control mechanism for type II ELMs by using edge heating. The usefulness of this effect will depend on the ELM type in ITER, which, at the moment, cannot be predicted accurately.

6.2.6.2. Effect of ECH on sawteeth

As in the case of ELM control, sawtooth (see section 3.2.2) control in ITER will require a tailoring of repetition frequency of sawteeth in order to maximize their beneficial effect in transporting impurities and the He ash out of the plasma center. As in tearing mode control, AC and DC schemes are both possible. The DC scheme operates on the equilibrium profiles, while the AC scheme influences the $m = 1$, $n = 1$ mode connected with the sawtooth. Control of the pressure profile inside the q = 1 surface can in principle control the sawtooth behavior [58]. However, here one has to compete with the 300 MW of α-power, so that this method does not

seem feasible. On the other hand, a localized DC current drive at the q = 1 surface has been successfully demonstrated by ion cyclotron heating in JET [59]. Due to the more localized deposition of EC waves, this heating method will be even better suited to this scheme. An AC scheme for sawtooth control might be possible by local current drive in the O-point of the $m = 1$, $n = 1$ precursor mode in order to change its growth rate and thus prolong or shorten the sawtooth repetition time. Theoretical estimates show that this might be more difficult than for the $m = 2$ because of the almost ideal character of the $m = 1$ resistive kink. However, a way of altering ideal stability in order to make the mode grow like a resistive mode, which can then be stabilized like an $m = 2$ mode, has been proposed in [60]. This area requires further theoretical and experimental work.

6.2.7. Application to ITER

6.2.7.1. Technological issues

Gyrotrons, a type of millimetre wave oscillator [61], are presently unequaled in their ability to generate high power efficiently at the frequencies of interest to ITER. High power millimetre-wave windows are required to form the vacuum envelope on the tube itself, as well as on the torus. Several types of window which are potentially capable of steady-state MW-level operation include room temperature single disk, edge-cooled diamond windows and “chilled” high-resistivity Au-doped silicon windows, cryogenic windows, and distributed windows [62].

The state-of-the-art in gyrotron and window development establishes constraints on the performance which can be expected to be available for ITER. The development goal is the simultaneous demonstration of a 170 GHz, 1 MW, steady-state, 50% efficient tube with the use of a single stage depressed collector [63, 64]. The choice of frequency is a compromise between the state-of-the-art in the technology, the operational range in magnetic field, and the heating and current drive physics requirements. Window performance generally limits the output power to the

1 MW range, although outputs powers of up to 2 MW may be possible with diamond windows [65].

Since electron cyclotron waves propagate in vacuum, the launcher need not be in close proximity to the plasma to efficiently couple to it. However, to provide the required steering capability, neither can the launch point be too distant. As a compromise, the launch location has been chosen at a point behind the blanket/back-plate, about 1 m distant from the plasma. The low field side (LFS) midplane has been chosen for the location of the launchers. Modeling shows that this option is well suited for the intended applications of heating and current drive.

Central heating at full field both in reference discharges and in advanced scenarios is possible. Off-axis current drive is also possible in almost all cases of interest. Thus, in terms of overall flexibility, the proposed single frequency system is well optimized, particularly given the range of parameters and applications of which it is capable and the variety of engineering constraints it satisfies.

6.2.7.2. Heating and current drive in the ITER reference discharge

Studies of core current drive in ITER-like plasmas [16] recommend scenarios based on up-shifted absorption of elliptically polarized ordinary-mode EC waves launched from the LFS midplane [see §6.2.2.2]. Modeling of the ITER reference discharge has shown that the current drive efficiency depends strongly on both the EC wave frequency and launch angle. At the full field of 5.7 T, frequencies suitable for current drive lie in the range 160 - 230 GHz, as shown in Fig. 6.2-2. For each frequency there is an optimal toroidal launch angle. For example, at 230 GHz the predicted central current drive efficiency at full field is in the range $\eta_{20} \sim 0.28–0.33$ $AW^{-1}m^{-2}$ for $T_{e0} \sim 20–30$ keV and requires a toroidal launch angle of $\sim 40^{\circ}$. At the highest temperature, the dependence of the current drive efficiency on temperature is weak.

Effective core heating and core current drive can be provided by a single system at 170 GHz, the choice of the frequency of the gyrotron sources. This places the heating slightly inboard

of the major axis, at $r/a = 0.15$, for perpendicular propagation. Full absorption is obtained, even in the initial Ohmic phase of the discharge ($T_{e0} \sim 5$ keV, $n_{e0} \sim 3 \times 10^{19}$ m^{-3}), and can be maintained after the H-mode transition throughout the density ramp-up and approach to ignition. Between the Ohmic and ignited phases of the discharge the opacity varies between 30 and 300, implying strongly localized deposition. The optimum toroidal angle for CD is relatively insensitive to temperature in the range 5–30 keV. In this case, the predicted current drive efficiency is 0.16 AW^{-1}m^{-2} at $T_{e0} = 20$ keV and increases to 0.19 AW^{-1}m^{-2} at $T_{e0} = 30$ keV. At reduced magnetic field, increased current drive efficiencies are achievable, since this is analogous to increasing the frequency at fixed field. Thus at 170 GHz and $B_\phi \sim 4.2$ T, current drive efficiencies $\eta_{20} \sim 0.3$ AW^{-1}m^{-2} are obtained [28].

Rationalizing the technological constraints with the proposed heating and current drive missions for ITER leads to a system based on 170 GHz fixed frequency gyrotrons. With the current design, approximately 50 MW of elliptically polarized O-mode power can be launched over a range of toroidal angles from a single equatorial port. The resulting system is flexible in that it can fulfill a wide variety of functions under both the reference and advanced tokamak modes of operation.

6.3. FAST WAVE HEATING AND CURRENT DRIVE

6.3.1. Introduction

After the pioneering work of heating in the ion cyclotron range of frequencies (ICRF) in TFR, PLT and a number of smaller machines [66], radio-frequency (RF) heating is now widely used on existing tokamaks, and includes many systems operating at the multi-megawatt level (Table 6.3-I).

Table 6.3-I: The Present ICRF Systems of Various Tokamaks

	Frequency (MHz)	Number of antennas	Generator power (MW)	Max-Coupled power (MW)
ASDEX-Upgrade	30–120	4 (×2 straps)	8	5.7
C-mod	80	2 (×2 straps)	4	3.5
DIII-D	30–120	3 (×4 straps)	6	3.6
HT-6M	14–45	1 (×1 strap)	1	0.6
JET	23–57	4 (×4 straps)	32[(1)]	22
JT-60U	102–131	2 (2×2 straps)	8	7
TEXTOR	25–38	2 (×2 straps)	4	3.6
TFTR	30-76	4 (×2 straps)	14	11.4
Tore Supra	35–80	3 (×2 straps)	14	9.5

[(1)] Losses in long transmission lines 8 MW

The fast magnetosonic wave can experience a large variety of interactions with plasma particles, including ion cyclotron fundamental and harmonic damping, or direct coupling to the electrons' parallel motion, when the general resonance condition

$$\omega = p\,\omega_{cs} + k_{//}\,v_{//s} \qquad (6.3.1)$$

is fulfilled for species s and cyclotron harmonic number p = 0,1,2... (ω is the wave frequency, $\omega_{cs} = Z_s eB/m_s$ is the cyclotron frequency, with $Z_s e$ the charge, m_s the mass, $v_{//s} = \mathbf{v}_s \cdot \mathbf{B}/B$ the component of the particle velocity, $\mathbf{v}_s$, parallel to the magnetic induction, $\boldsymbol{B}$; $\boldsymbol{k}$ is the wavevector with components along and perpendicular to $\boldsymbol{B}$: $k_{//} = \mathbf{k} \cdot \mathbf{B}/B$, $k_\perp = |\boldsymbol{k} - k_{//}\boldsymbol{B}/B|$). The standard interactions are cyclotron heating of ions ($p > 0$, $s = i$) and transit-time magnetic pumping (TTMP) or Landau damping of electrons ($p = 0$, $s = e$). In addition, the fast magnetosonic wave (FW), which is the carrier of the RF energy, can be converted into short wavelength electrostatic waves (e.g. ion Bernstein waves) which damp rapidly on ions or electrons according to the scenario.

In the ion heating regime, the transfer of energy from the wave to the ions causes velocity-space diffusion, i.e. the formation of a tail in the velocity distribution function of the heated species, that can be tailored to some extent by controlling the power deposition profile. The direct power coupling to the ions is a distinct feature of ICRF that can be exploited to control the plasma reactivity. In a reactor, this assists the L-to-H mode transition and/or allows control of the burn [67]. In harmonic heating, the wave interacts preferentially with the more energetic ions. This can be exploited to influence energetic particle populations selectively. The presence of $k_{//}$ in the resonance condition, Eq. (6.3.1), allows the wave to generate current by launching non-toroidally-symmetrical spectra, which favors interaction with particles (electrons or ions) moving toroidally in one or the other toroidal direction. The RF power can also be used to create a plasma inside the vacuum chamber in the presence of a toroidal magnetic field for wall conditioning, depositing coatings, or for start-up assistance. Hence, the ICRF system is a flexible tool which can address a range of tasks for next step machines and reactors. RF systems are based on well-established technology that can be easily extrapolated to reactors.

The processes of wave propagation, damping and velocity-space diffusion are described in textbooks [68, 69, 70], while introductory texts on the application of wave processes to heating and non-inductive current generation in fusion plasmas are available [71, 72, 73]. The subject was recently reviewed [74].

6.3.2. Physics and Performance of Power Coupling

The electromagnetic energy is coupled to the plasma using loop antennas, slots, or waveguides. Except for the possible excitation of short-wavelength electrostatic waves near the ion-cyclotron layers, the coupling and wave propagation problem can be described in the cold-plasma limit. In this limit two generally uncoupled waves co-exist: the fast wave and the slow wave with respective perpendicular refractive index component $n_{\perp F}$ and $n_{\perp S}$ ($\boldsymbol{n} = \boldsymbol{k}/k_0$, $k_0 = \omega/c$)

$$n_{\perp F}^2 = S - n_{//}^2 - \frac{D^2}{S - n_{//}^2} \qquad \text{(fast wave)} \tag{6.3.2}$$

and

$$n_{\perp S}^2 = P\left(1 - \frac{n_{//}^2}{S}\right) \qquad \text{(slow wave)} \tag{6.3.3}$$

following the notations of [69] for the dielectric tensor elements S, D, P. For ICRF in ITER, typical magnitudes of these quantities are (at the plasma center $n = 10^{20}$ m^{-3}, $B_T = 5.7$ T, $f = 2f_{cT}$)

$$S \approx -700, \; D \approx 1400, \; P \approx -2.5 \times 10^6 \tag{6.3.4}$$

The parallel component of the refractive index vector $n_{//}$ is determined by the antenna size, $n_{//} \approx \pi/(k_0 L_z) \approx$ 1-10 (L_z is the toroidal distance between successive straps), i.e. it is significantly smaller than the dielectric tensor components. Accordingly, the slow wave is strongly evanescent ($n_{\perp S}^2 < 0$) with, according to Eq. (6.3.3), a typical evanescence length

$$\lambda_{\perp S} = 1 / | k_\perp | \approx 0.6 \text{ mm} \tag{6.3.5}$$

Its polarization vector has $E_{//}$ as the main component. The wave evanescence reflects the fact that the plasma acts as a very good conductor in the parallel direction and screens out the parallel

electric field by allowing image currents to flow over one skin depth (Eq. (6.3.5)). Inside the plasma the fast wave propagates with typical wavelength

$$\lambda_{\perp F} = 2\pi / k_{\perp} \approx 0.12 \text{ m} \qquad (6.3.6)$$

Note that both scale lengths, Eq. (6.3.5, 6.3.6), are roughly inversely proportional to density, i.e. increase towards the plasma edge. At the very edge, the density falls nearly to zero, $S \approx 1$ and $D \approx 0$, and the fast wave connects to the vacuum wave polarized with electric field perpendicular to the static magnetic field. For a large part of the $n_{//}$ spectrum of usual antennas, this vacuum wave is evanescent ($k_{//} > k_0$) and, if we call $k_{//c}$ the characteristic parallel wavenumber of the antenna, the electromagnetic field decays as $\exp[-k_{//c}\,\Delta r]$ a radial distance Δr away from the antenna in the vacuum or very low density plasma layer. It is therefore harder to couple the FW power for larger distances between antenna and last closed flux surface.

Many ICRF coupling models have been developed. These models rely on a slab approximation, assuming uniformity in the toroidal and poloidal directions and a radiation boundary condition in the radial direction. Image currents induced on conducting surfaces surrounding the powered conductors must be taken into account in the computations because they deform the spectrum and thereby modify the antenna radiation resistance [75]. The most relevant of these models to ITER is the RANT-3D code [76] which allows the plasma to extend to the first wall and for the antennas to be recessed into the first wall. This code is currently used to compute the resistance of the ITER antennas. It has been benchmarked against experimental results [76] and has been shown to predict accurately the loading resistance in TFTR when the computation uses the experimental density profiles measured in front of the antenna by reflectometry.

Many of the early ICRF experiments were plagued with impurity production [66]. This problem has disappeared in present experiments [77] due to improved conditioning and coating of the first wall. In particular, the use of a material, like Be, with a self-sputtering coefficient less than unity limits impurity production from the Faraday screen [78]. The impurity production has been explained on the basis of the RF sheath effects generating fast ions [see Fusion Engineering

and Design **12** (1990) for a review]. RF sheath theory has been applied to ITER antennas [79], indicating that they are properly designed in this respect. The sheath effects are expected to be largest when the antenna arrays are operated with zero-phasing. In this case, image currents on septa or other antenna parts are large and the sheath voltages largest. In most cases, zero-phasing operation is observed to disturb the plasma edge more than π-phasing and, in several instances, to lead to reduced heating efficiency or inhibition of the transition to H-mode [78, 80-82]. Operation with $\pi/2$ phasing, as is required for ICRF current drive, may also lead to a reduction in heating efficiency [83]. In JET H-modes, the energy content is about 20% less using $\pi/2$ phasing as compared to dipole phasing, due either to less power reaching the plasma core, or to a reduction in H-mode quality. The better understanding of RF sheaths has also led to a proposal to remove Faraday shields from ICRF antennas, and experiments with unshielded antennas have been successfully performed in TEXTOR [84] and ASDEX-Upgrade [85] without significant differences as compared to shielded antennas. Although it might be necessary to keep a Faraday shield for other reasons, such as decoupling of thermal and mechanical stresses on plasma facing components (Faraday shield or current strap), in ITER this opens a way to simplified antenna structures.

One of the problems of the ITER antennas is the large distance to the last closed flux surface (15 cm) and the short density scrape-off length (2 cm) assumed in modeling ITER antenna coupling. With such parameters, the required voltage for coupling the 50 MW in ITER (see §6.3.7) would be about 40 kV in $\pi/2$ phasing and would be in excess of 50 kV in π phasing. While several experiments operate, with plasma, at voltages near 40 kV, none is operated routinely at 50 kV. Experiments in JT-60 [86] and ASDEX-Upgrade [87] have shown a more complicated scrape-off layer structure, with a much slower density decay far away from the LCFS. ITER-relevant shots with ICRF heating, at the second harmonic of H, have been performed in JT-60 with a LCFS to antenna distance similar to that expected in ITER (15 cm). Under these conditions, a power density of 4 MWm^{-2} was launched from the antenna with a maximum voltage of 38 kV [88]. This matches ITER requirements, albeit at somewhat higher frequency (102 MHz).

The edge density variations due to ELMs cause fast variations of the antenna coupling resistance that must be compensated to avoid excessive reduction of the average power or generator tripping. One type of compensation uses recombination of the reflected power from two antennas by hybrid couplers and was successfully tested on DIII-D [89] and ASDEX-Upgrade [82]. Other systems are under development based on frequency feedback [90, 91].

6.3.3. Modeling

The coupling, propagation and absorption of the wave are determined by the wave equation

$$\nabla \times \nabla \times \vec{E} - \frac{\omega^2}{c^2} \vec{\vec{\varepsilon}} \vec{E} = \frac{4\pi i \omega}{c^2} \vec{j}_A \tag{6.3.7}$$

where $\vec{j}_A$ is the antenna current and $\vec{\vec{\varepsilon}}$ is the dielectric tensor. In general, $\vec{\vec{\varepsilon}}$ is a complex integral operator acting on the electric field $\boldsymbol{E}$. However, $\vec{\vec{\varepsilon}}$ reduces to a simple matrix for cold plasmas. With the complete hot-plasma $\vec{\vec{\varepsilon}}$, Eq. (6.3.7) is too complex to be solved in full toroidal geometry. Therefore, one resorts to approximation (see [92] for a review). One class of approximation is to solve the system in slab geometry (1-D codes). In this geometry, one can retain the full complexity of Eq. (6.3.7) as an integro-differential system. Alternatively, reduced-order descriptions are available. The advantage of 1-D codes is that they are fast, can correctly treat short wavelength modes, and provide quick insight into the physics of particular scenarios. The second class of approximation is developed by retaining the complexity of both the hot-plasma $\vec{\vec{\varepsilon}}$ and the toroidal geometry, while treating wave propagation in the eikonal approximation. This reduces the integro-differential system, Eq. (6.3.7,) to an algebraic system. The resulting ray tracing codes (see e.g. [93, 94]) determine the deposition profile in the cases where the wavelength is small compared to the dimensions of the machine. This is often the case for large machines like ITER. Ray tracing codes are usually not able to tackle interference effects, sharp reflections, or mode-conversion processes which involve tunneling.

More recently, 2-D global wave codes (e.g., [95-98]) have been developed which resort to a direct numerical solution of reduced-order approximations to Eq. (6.3.7), using finite element or finite difference methods, often combined with poloidal Fourier decomposition. This numerical procedure works for long-wavelength waves, but convergence is much more difficult to achieve if short-wavelength structures are generated or short-wavelength modes are excited. The lowest order approximation retains only the fast wave. More involved codes include the slow wave and sometimes the ion Bernstein and kinetic Alfvén waves. The basic output of these codes is the distribution over magnetic surfaces of the RF power transferred to the different plasma species. Power deposition profiles predicted by eight different codes have been compared and good agreement has been achieved in most cases [99].

The dielectric operator depends on the distribution functions of the plasma species. During intense RF-heating, energetic tails develop on distribution functions of the heated ion species that broaden the deposition profile and increase the absorption strength. The velocity distribution of the resonating ions results from wave-induced velocity-space diffusion and Coulomb collisions. The velocity distribution during ICRH can be obtained by solving a quasi-linear Fokker-Planck equation

$$\partial f / \partial t = C(f) + Q(f), \tag{6.3.8}$$

where C is the collision operator and Q the RF-operator [69]. The velocity distribution becomes highly anisotropic at large velocity. This is because the collision frequency decreases with energy, while the cyclotron interactions, which preferentially heat the ions in the perpendicular direction, do not. Various Fokker-Planck codes for calculating the velocity distribution have been developed [100-102]. Most of them are based on the quasilinear diffusion operator of [103] derived for straight magnetic field lines. More recent models, based on the Monte-Carlo technique, incorporate finite banana width effects and configuration space-diffusion due to RF [104-106], leading to a broadening of the collisional power transfer profiles to the background plasma species.

The last step in the modeling of the effect of RF heating in the plasma consists of incorporating the result of the combined solution of Eq. (6.3.7, 6.3.8) in a transport code in order to compute the changes in temperature and profile modifications due to RF. The RF input comes into the energy balance equations as power deposition profiles into the various plasma species. An additional input is in the contribution of the RF-generated tails to the plasma β and to the non-thermal plasma reactivity. In turn, the plasma equilibrium and profiles are used for the computation of the solutions of Eq. (6.3.7, 6.3.8).

The PRETOR transport code [107] is often used for prediction of ITER plasma evolution. Recently, the PION code has been implemented in PRETOR to study the effects of direct ion heating on the plasma and, in particular, its effect on the H-mode threshold crossing [108]. The power deposition is solved self-consistently by modifying the dielectric tensor as the distribution functions evolves in time. Experimentally measurable quantities, such as the fast ion energy content [109], or the neutron rate, can be compared with model predictions. Figure 6.3-1 shows the good agreement between the measured neutron rate in a JET discharge and that calculated with the PION code [110].

6.3.4. Heating Scenarios and Database

The ITER ICRF system is designed for heating at second harmonic tritium ($2\omega_{cT}$) or fundamental minority ^{3}He (ω_{c^3He}) resonance (57 MHz at full toroidal field), with ω_{cD} (42 MHz) as an alternative minority scheme. The system can operate at constant performance in the frequency range 40-70 MHz, covering the whole ITER toroidal field range ($4.0 < B_\phi < 5.7$ T). The ^{3}He minority scenario can also be used in pure deuterium or hydrogen. During the ignited phase, ICRF can be used for controlling the sawtooth period using minority ion current drive at the q=1 surface either inboard (75 MHz) or outboard (55 MHz). Fast wave Current Drive (CD) scenarios are in the frequency window between $2\omega_{cT}$ and $2\omega_{cD}$, with a maximum CD efficiency around 62 MHz. In this section, we outline high-power ICRF heating and confinement results obtained in a variety

of scenarios including those that are proposed for basic ITER applications. The CD database is discussed in the next section.

6.3.4.1. General ICRH database

Significant levels (up to 22 MW) of ICRF power have been coupled to L-mode plasmas in tokamaks world-wide using FW outboard antennas. This includes 3.6 MW in DIII-D [11], 3.5 MW in Alcator C-Mod [112], 5.7 MW in ASDEX Upgrade [113], 3.6 MW in TEXTOR [114], 7 MW in JT-60U [115], 9.5 MW in Tore-Supra [116], 11.5 MW in TFTR [117] and 22 MW in JET [118]. Central minority ion heating with H or ^{3}He as the minority species in D plasmas has been the most generally used scenario, because fundamental cyclotron absorption is a strong mechanism as long as the polarization of the wave remains good (significant E_+-component), i.e. for not too large minority concentration. Some devices [81, 87, 118] have also carried out second harmonic heating of hydrogen. The antennas consist of 2 or more radiating straps which are generally phased $(0,\pi)$. The power is deposited centrally, including at high plasma density, by locating the ion cyclotron layer in the center of the plasma. Low concentration minority ion heating produces strong tails which relax on electrons leading to higher T_e (1.5-2 times T_i, depending on density) in present devices. While pulse lengths for high-power ICRF heating are typically 2-10 s, Tore Supra has coupled 2 MW for 30 s and JET 3 MW for 60 s, achieving quasi steady-state conditions. H-modes (with energy confinement typically twice that of L-mode) with ICRF heating have been obtained in Alcator C-Mod, ASDEX Upgrade, DIII-D, JT-60U and JET. A major factor in achieving H-mode with ICRH in JET is automatic control of the coupling resistance, which has been achieved by feedback control of the plasma radial position [78]. The maximum power coupled to an ELMy H-mode in highly (edge) radiative JET discharges is about 16.5 MW. Improved confinement (about twice L-mode) has been obtained with combinations of ICRF and NBI at high density with impurity seeding and radiative edge (nearly 100% radiated) in TEXTOR [119].

Some amount of momentum can be transferred from the wave to the plasma if an asymmetric spectrum is launched. As compared, for example, to NBI, this amount of momentum is relatively modest. However, direct momentum transfer is not the only way to induce plasma rotation. Experiments on JET and Alcator C-Mod show that ICRF can indirectly induce a significant amount of toroidal co-rotation, up to 10^5 ms^{-1} in C-Mod [120, 121]. In JET, rotation is explained by the increase in ion pressure gradient following the H-mode transition, but in C-Mod the ∇p contribution is negligible and the rotation might result from the build-up of a radial electric field due to displacement of the fast ion orbits by ICRH.

6.3.4.2. Scenarios for basic ITER applications

All scenarios relevant to ITER have been tested in various existing experiments. With a view to applications to a 50/50 D-T reactor plasma, heating at high minority concentration has been demonstrated at a power level of 10 MW in JET with $n_H/n_{He3} \leq 1$. At high concentrations, minority tails are less energetic and more power is delivered to background ions [122], leading to $T_i > T_e$. ICRF heating at the second harmonic of tritium has been carried out in D-T plasmas in TFTR [117]. In a combined heating experiment with $P_{ICRH} = 5.4$ MW and $P_{NBI} = 23$ MW, it was found that the additional ICRH power increased the T_i from 26 to 36 keV and T_e from 8 to 10 keV. The neutron production rate increased by 10% and the confinement was about 10% better in D-T than D discharges due to the isotope effect. In the absence of beams, tritium is introduced via a gas puff. In such pure-RF experiments, despite a low target temperature of 2 keV, the damping was adequate, due to the rapid formation (100 ms) of an energetic tritium tail (500 keV), and the heating efficiency was comparable to that obtained with NBI [123, 124]. By power modulation experiments, it was deduced that 2/3 of the RF power was going to ions and 1/3 to electrons via direct electron damping.

In JET a wide variety of experiments in D-T have been performed where ICRF alone was used to heat the plasma [125]. The efficiency of second harmonic T heating was less than that of

minority scenarios (enhancement factors $H_{97} = \tau_E/\tau_{E,ITER97H\text{-}P}$ over the H-mode confinement scaling ITER97H-P [126] of about 0.7, compared to 0.85-0.95 for minority scenarios) due to the formation of a very energetic T tail and subsequent loss of fast ions representing a 20% power loss. A second consequence of the highly energetic tail is a predominant transfer of power to the electrons. However, these results are well explained by the PION code, which predicts for the ITER case, where the RF power density is only about one third that in JET, predominant power coupling (70%) to the ions. Addition of about 1% ^{3}He improves the performance dramatically, leading, even with the large power density of JET, to strong ion heating with $T_{i0} \approx T_{e0} \approx 12.5$ keV. Thermal neutrons dominate all ICRH schemes in tritium plasmas except in the (D)-T scenario. In the latter scheme, the optimization of the D-minority tail in T plasmas produced fusion power of 1.7 MW, with Q = 0.22 for a record duration of 2.7 s. In both the (^{3}He)-D-T and (D)-T schemes, the enhancement factor H_{97} was ≥0.9, which is sufficient for ignition in ITER. In D-T plasmas, as in D plasmas, RF-heated discharges often have smaller ELMs (by a factor of 2-3) than NBI-heated discharges [127, 128].

Minority ion current drive physics was first discussed by [129]. The resonant condition $\omega - \omega_{ci} = k_{//}\, v_{//}$ implies that the current is driven in opposite directions on the two sides of the minority cyclotron layer in a tokamak. Since the effect is local, it can be used to modify the gradient of plasma current density, especially near the q = 1 surface, either to stabilize or destabilize sawteeth [130, 131]. Such a control of sawteeth provides some control over the energy confinement inside the q = 1 surface and could possibly be used to advantage for burn control in a reactor.

"Heavy minority" scenarios, relevant to the non-activated phase of ITER in hydrogen, have been investigated both experimentally and theoretically. Experiments have been performed in JET, ASDEX Upgrade and C-Mod. In JET, D-(T), H-(D) and H-(^{3}He) schemes have been used in L-mode (RF power ≤ 3 MW) [132]. These scenarios have somewhat lower confinement than the normal "light minority" scenarios. Minority T (5-10%) in D showed a large neutron production associated with a suprathermal T-tail formation [125]. In ASDEX Upgrade, H-(^{3}He) heats the

electrons more effectively than FW direct electron heating [113, 133]. In C-Mod, H-(^{3}He) has 20-30% lower heating efficiency and lower single pass absorption than D-(H) [134]. Results from a 1-D full wave code [135] indicate that good single pass absorption with dominant ion heating would be obtained for both H-(^{3}He) and H-(D) in ITER at sufficiently low concentration (≤3%) and for usual toroidal mode numbers (n_T=20,40). At larger concentrations and lower n_T, ion absorption drops significantly. In all cases considered, the absorption at the Alfvén resonance located in front of the antenna [132] was negligible (<1%).

6.3.4.3. ICRF in advanced scenarios

Applicability of ICRF minority heating in negative shear discharges is an important subject for ITER steady-state scenarios, where the current profile is hollow because of a high bootstrap current fraction. Attempts at ICRF heating in advanced scenarios were made in several machines [136]. In JET, in optimized shear discharges a substantial part of the ICRF power was coupled to deuterons, especially at high T_e, leading to a neutron yield comparable to that obtained in hot-ion H-modes with less stored energy [137]. In JT-60U, minority and second harmonic heating have been used in negative shear discharges [88, 138]. Second harmonic hydrogen minority ICRF heating was successfully applied to negative shear plasmas, typically with $q_0 \sim 6$, $q_{\min} \sim 2$ and $q_{\text{eff}} \sim 5$. The negative shear configuration was produced by current ramp-up with early beam injection of 13 MW, followed by injection of 4 MW of ICRF power. The electron and ion temperatures in the plasma core increased significantly after start of the ICRF injection and reached ~7 keV and ~12 keV, respectively. A transport barrier was produced near the position of the minimum value of the safety factor. Steep gradient layers appeared in profiles of the electron and ion temperatures and the electron density. The H-factor H_{89} increased from 1.4 before ICRF to 2.0 at the end of the ICRF pulse. A transport barrier was also produced when $P_{\text{IC}} >> P_{\text{NB}}$ (P_{IC} = 4.5 MW, P_{NB} = 1.5 MW) [138]. In these conditions, the electron density profile was not so steep because of the absence of particle fueling. Similar results may be obtained in ITER,

where α-particle heating is dominant. Direct FW electron heating of the "postlude" phase of enhanced reversed shear (ERS) discharges was also demonstrated in TFTR, delaying the transition out of the ERS [123]. In DIII-D, counter-FWCD in discharges with mildly negative shear causes spontaneous appearance of improved confinement [139].

6.3.4.4. Other ICRH scenarios

Other scenarios have been exploited in existing machines which do not directly extrapolate to ITER:

(i) *Heating at 3rd ion-cyclotron harmonic*. In JET and Tore Supra, it was possible to locate the 3rd harmonic of D in the center of the plasma while other cyclotron damping mechanisms, such as fundamental and 2nd harmonic of H, were outside the plasma. In JET, with 12 MW of ICRH power, a very energetic D-tail is produced which cuts-off at about 4 MeV, when the ion orbits reach the limiters. The D-D neutron rate reached 0.9×10^{16} s^{-1}. These results were well reproduced by PION [109] code calculations, giving confidence in the understanding of the production and confinement of energetic tails. Higher harmonic heating experiments were also performed in JT-60U [81], both on ohmic target plasmas and with beam heating for the study of sawtooth stabilization and beam acceleration. 2nd and 3rd harmonic heating of fast ions was studied in TEXTOR to investigate neutron production by beam acceleration and RF-controlled diffusion of fast particles [140].

(ii) *Mode Conversion Heating*. Significant electron heating has been observed by damping of ion-Bernstein waves (IBW) that were accessed by mode conversion of the externally launched fast-waves from the low-field side of the tokamak in mixed-species plasmas [113, 124, 141]. In TFTR and Tore Supra, a peak was observed in the electron temperature profile in the vicinity of the mode conversion layer where the IBW deposits its power into electrons. In TFTR, the location of the mode-conversion layer was deduced from modulation experiments and found to move in

agreement with theory when B_ϕ was varied. Efficient ion heating was obtained in TFTR in the case of a high ion temperature target plasma [142].

(iii) *Direct launch of the IBW* was also attempted with limited success, in terms of coupled power and heating efficiency, but leading in some cases to transport barrier formation [143] or poloidal rotation [144].

6.3.5. Current Drive

A resonant interaction occurs when the parallel velocity of an electron matches the parallel phase velocity of the fast wave. The partly opposite electron Landau damping and transit time magnetic pumping [69] result in fast wave electron heating (FWEH), with, for example, significantly less damping per pass than minority ion heating (one can estimate the FWEH damping per pass as ≈ 10-20% in existing machines and ≈ 50% in ITER). Up to 9.5 MW have been coupled to electrons in Tore Supra in a scenario where the electron damping per pass is about 10% and where the only competing damping is the central $3\omega_{cD}$, for which the damping per pass is estimated a hundred times lower [145]. The behavior with respect to the magnetic field has been explored on DIII-D (1 T and 2 T) and on Tore Supra (from 1.3 T to 3.5 T), confirming that the heating efficiency is independent of B_ϕ (because the fast wave ultimately damps on the electrons over many passes through the device), as long as the coupling to electrons remains the dominant damping process [146].

The power is deposited centrally (typically within r/a ≈ 0.4) [147, 148] and the interaction does not produce suprathermal electrons [149]. The resulting thermal electron pressure profile is peaked enough (although less peaked than e.g. central minority heating) for efficient bootstrap current generation (up to 35 kA/MW observed on Tore Supra) [150].

By asymmetrically phasing the antenna current straps, one directly couples the power to electrons flowing co or counter to the plasma current. This asymmetric absorption results in fast wave current drive (FWCD). The effect has been observed on JFT-2M [152], DIII-D [153] and

Tore Supra [145], with current drive efficiencies in excess of 0.04 10^{20} $AW^{-1}m^{-2}$ and shows a linear dependence with T_{e0}, in very good agreement with theoretical predictions (Fig. 6.3-2). The driven current profile is strongly peaked due to trapped electron effects, as was checked experimentally in DIII-D. The agreement with theory is very good [139]. The extrapolation to ITER leads to an efficiency of the order of 0.15–0.25 10^{20} $AW^{-1}m^{-2}$ (depending on electron temperature), providing an opportunity for the ICRH system to generate a sizable amount of central plasma current. The strong peaking of the driven current may be very effective for driving the central seed current and generating large bootstrap currents, as well as for controlling the central current density. Current drive experiments have also been performed in the mode-conversion regime in TFTR with an efficiency slightly in excess of theoretical predictions [151].

6.3.6. Plasma Production

Non-inductive plasma production will be an indispensable tool for keeping constant wall conditions in superconducting devices. It will also be required for low voltage tokamak start-up in reactor scale fusion devices (for the present ITER start-up scenario, the inductive electric field is limited to $E \approx 0.3$ Vm^{-1}). Early attempts at plasma production with ICRF power were made in stellarators [154]. ICRF plasma production has now been successfully achieved in the tokamaks TEXTOR-94 [155] and Tore Supra [156] using conventional double-loop antennas operated at their normal ICRH frequency. RF discharges have been obtained in pure toroidal magnetic fields in ^{4}He, D and H over a wide range of magnetic field values (ω / ω_{ci} ranging from about 0.5 to 20). RF power at the generator during these experiments ranges from 50 kW to 0.5 MW, with coupling efficiencies ranging from 50% to more than 90%. Central line-averaged densities range from a few 10^{17} m^{-3} to 4×10^{18} m^{-3}, while temperatures are estimated to be in the range 5-50 eV. In TEXTOR, the unshielded antenna [84] is about twice as efficient as the shielded one.

RF-produced discharges in D and ^{4}He have also been used in TEXTOR-94 and Tore Supra, under various conditions of pressure, magnetic field and RF power, to clean the tokamak

first wall. In all cases the performance was reported to be at least as good as that of glow discharge cleaning. In D discharges in Tore-Supra and TEXTOR-94, ions in the keV range were measured, indicating direct power coupling to ions. In TEXTOR-94, RF discharges were also performed in mixtures of ^{4}He and Silane for silicon coating of the walls. Plasma production in the presence of stray poloidal magnetic fields is more delicate than in a purely toroidal magnetic field. Nevertheless reproducible low loop-voltage (3-5 V corresponding to 0.3-0.5 V/m) start-up was realized in TEXTOR-94 using only the screenless antenna at 100 kW (60% coupling efficiency), at gas pressure ~$(4–9) \times 10^{-5}$ mbar and in the presence of 10-15 G residual stray field [157].

6.3.7. The Functions of the ICRF System in ITER

The ITER ICRF system is designed to couple 50 MW to the plasma through four ports. In each port, an array of eight antennas (four toroidal by two poloidal) is installed, with a nominal power of 2 MW/antenna (i.e. total power of 64 MW at the generators). Each antenna is equipped with a semi-transparent Faraday shield, aligned along the total magnetic field, and tuned at both ends by adjustable reactances (pre-tuning stubs) to make it resonant. The maximum operating voltage is < 42 kV under the assumed conditions of rather large distance to the last closed flux surface i.e. rather low plasma coupling (3.5 Ω/m). An important design issue is the array sensitivity to plasma edge density fluctuations (such as those due to ELMs), which cause fast variations in the antenna coupling and may reduce the RF power flow. The pre-tuned antenna design, based on an external adaptive matching system using adjustable mechanical components and frequency modulation, is designed to achieve a maximum tolerance to such variations.

From the technical point of view, the most critical element of the system is the antenna, because it has to operate routinely at high voltage. An ITER antenna prototype has been built and successfully tested in vacuum (up to 72 kV for 0.1s pulses and 62 kV for 2s pulses) [158]. Feedthroughs and pre-tuning stubs have been designed to be mounted on the antenna prototype for a fully integrated test [159]. Existing RF generators have been operated on matched loads for up to

2 hours at a level of 1.5 MW [160]. A generator design at full ITER specification (2 MW CW with a Voltage Standing Wave Ratio (VSWR) of 2 and transients at 2.5) is underway.

The main operating mode of the ICRF system in ITER is second harmonic heating of tritium, possibly with ^{3}He minority. The main asset of the ICRH is that it can couple a large fraction of the power (up to 70%) to the bulk ions, a feature shared by none of the other ITER heating systems. Some simulations indicate that the access to H-mode with pure electron heating may be restricted to very low density, while increased fractions of ion heating broaden the H-mode accessibility domain. The ICRH system is capable of efficient operation over a wide range of toroidal magnetic fields and heating scenarios are available for a physics phase in pure D, ^{4}He or H. The ICRH power can be feedback controlled and is an ideal tool for burn control in driven scenarios due to its strong coupling to ions, or for controlled and safe current ramp down. In advanced scenarios, ICRF can provide a very peaked central current with current drive efficiency 0.15-0.25 10^{20} $AW^{-1}m^{-2}$.

The ICRF system has a number of ancillary functions, such as wall conditioning (tritium desorption), or coating, plasma breakdown and current start-up. It also allows control of the burn, by modifying the sawtooth behavior through off-axis minority current drive, and can generate toroidal rotation.

6.4. LOWER-HYBRID HEATING AND CURRENT DRIVE

6.4.1. Introduction and Basic Physics

Over the last 25 years, slow waves in the lower hybrid (LH) range of frequency have been used for various purposes. The occurrence of a wave resonance, the lower hybrid resonance (LHR), where the wave group velocity in the direction perpendicular to the static magnetic field vanishes for a particular frequency, plasma density and magnetic field strength, was soon anticipated to lead to very strong wave-particle interaction through linear mode conversion to a hot plasma wave (and/or non-linear phenomena), and made lower hybrid waves (LHW) a good candidate for plasma ion heating (LHIH). Later, the large parallel electric field carried by LHW was also shown to lead to strong quasi-linear Landau interaction with electrons, through wave-particle resonance in the direction parallel to the static magnetic field ($\omega = k_{//} v_{//}$), and consequently to electron heating (LHEH) and non-inductive current drive (LHCD). Early experiments, performed on Petula, Wega, Versator, WT-2, ASDEX, JFT-2, Alcator, PLT, FT-1, T-7 and JT-60, yielded important achievements concerning the capability of these waves as far as heating and current drive, as well as plasma start-up and current ramp-up, are concerned [161]. In present-day experiments, the main thrust for using LHW is linked to their significant potential for current drive and profile control, and therefore the frequency and antennas are generally optimized for electron interaction and current drive. Large LH systems now exist on many tokamaks (Table 6.4-I).

The LHR frequency ω_{LH} is of the order of the ion plasma frequency ω_{pi},

$$\omega_{LH} = \omega_{pi} / [1 + (\omega_{pe} / \omega_{ce})^2]^{1/2} \qquad (\omega_{pi} >> \omega_{ci}) \qquad (6.4.1)$$

Table 6.4-I : The present LHW systems on various tokamaks

	Frequency (GHz)	$N_{\|\|}$	Number of waveguides	Generator power (MW)	Coupled power (MW)
COMPASS	1.3	2.1–6.7	8	0.6	0.15
FT-U	8.0	1.4–3.75	72 (6 ant.)	5.5	1.3
HT-6M	2.45	3.0	8	0.12	0.12
JET	3.7	1.4-2.3	384	12	7.3
JT-60U	1.74–2.23	1.3-2.4	24	5.0	2.5
	1.74–2.23	1.5-2.3	48	10	6.0
PBX-M	4.6	4.2	32	2.0	1.5
TdeV	3.7	2.0-3.3	32	1.3	1.0
Tore Supra	3.7	1.4–2.3	256 (2 ant.)	8.0	6.0
TRIAM-1M	2.45	1.0–3.6	4	0.05	0.045
	8.2	1.0–2.8	8	0.2	0.15

This frequency, in the GHz range, is much larger than the ion cyclotron frequency and much smaller than the electron cyclotron frequency. It is of the order of - but always smaller than - the geometric mean between these two. Somewhat higher frequencies (2–10 GHz) are more suitable for present applications, where pure electron interaction is desired, whereas lower frequencies (below 1–2 GHz) were used in early ion heating experiments where the LHR was thought to be essential. In fact, as discussed later, it turns out that even when the LHR does not exist, the perpendicular phase velocity of the LHW will slow down above some critical density, so that the LHW will interact strongly with plasma ions.

For a sufficiently large electron temperature and parallel index of refraction $N_{||} = k_{||}\, c\, /\, \omega$ along the static magnetic field, the parallel phase velocity of the wave, $\omega/k_{||}$ is a few times the thermal speed of the electrons, v_e. As a result, a quasi-linear plateau tends to build up in the electron velocity distribution function over the range of velocities [162],

$$v_{||\min} = c/N_{||\max} < v_e < v_{||\max} = c/N_{||\min} \qquad (6.4.2)$$

corresponding to the local $N_{||}$-spectrum of the absorbed power, with $P(N_{||}) \neq 0$ for $N_{||max} < N_{||} < N_{||min}$.

For high efficiency current drive purposes, the central $N_{||}$ value of the wave spectrum launched by the antenna (and quoted in Table 6.4-I) is chosen in such a way that the wave interacts with a broad range of weakly collisional suprathermal electrons.

A strong interaction of the LHW with the ion population is possible when the perpendicular phase velocity, $\omega/k_{\perp}$, decreases to a few times the ion velocity [163]. It can be seen from the cold electrostatic dispersion relation of the LHW,

$$\omega^2 = \omega_{LH}^2 \, [\, 1 + (m_i / m_e) \, (k_{||} / k_{\perp})^2 \,], \qquad (6.4.3)$$

that the ratio of the perpendicular to the parallel phase velocities depends only on local plasma parameters, through the local LHR frequency, and is independent of $N_{||}$. As a consequence, at a given frequency, the LHW power will be preferentially absorbed, either by the electrons or by the ions, depending mainly on the local plasma parameters encountered during the course of propagation, rather than the launched wave spectrum. The existence of a critical density, which scales roughly proportionally to ω^2, at which a wave damping switches from electrons to ions, follows almost directly from the electrostatic dispersion relation [164].

Another basic feature of LHW physics is the accessibility condition, which has to be met so that the LH waves can propagate far enough inside the plasma to reach the wave absorption layers. When considering the full electromagnetic cold plasma dispersion ($N_{||} \approx$ 1-2), one finds conditions for which the slow LHW merges with a fast wave branch so that linear mode conversion occurs. In order to avoid such a mode conversion between the wave launching point and the wave absorption layer, the following accessibility criterion must be satisfied [165] :

$$N_{||} > N_{||acc} = \omega_{pe}/\omega_{ce} + [1 + (\omega_{pe}/\omega_{ce})^2 - (\omega_{pi}/\omega)^2]^{1/2} \qquad (6.4.4)$$

where ω_{ci} and ω_{ce} are the ion and the electron cyclotron frequencies respectively.

This condition, which mainly depends on the magnetic field and the plasma density, limits the penetration of the wave into the plasma. Strictly speaking, it would apply in a separable geometry where $N_{||}$ is a constant of the propagation. In tokamaks, toroidal effects and magnetic field helicity lead to strong upshifts of the parallel wave index during the course of propagation, and the link between the launched $N_{||}$-spectrum and wave accessibility to the plasma core requires detailed ray-tracing calculations. For ITER parameters, these calculations show that only the outer part of the plasma ($r/a \geq 0.5$) is accessible to the LHW at the plasma densities which are envisaged during the burn. The high electron temperatures, however, lead to strong peripheral Landau damping. Since the main function of the LHW in ITER is off-axis current drive during steady state operation, current profile control in advanced regimes, and assistance of current ramp up during start of the discharge [166], the ITER LH system is optimized for current drive functions.

6.4.2. LH Current Drive Efficiency

Though successful in early experiments in the past [167], ion heating with LHW has not been the object of recent experiments. The use of LHW in present tokamaks is now focused on current drive applications, and for this purpose a higher operating frequency is chosen. Lower Hybrid waves are the most efficient means for non-inductive current drive in both present experiments and in projections to ITER. Fully non-inductive discharges of up to 3.6 MA in JT-60U and 3 MA in JET have been achieved with LHCD [168, 169]. A plasma current of 0.8 MA was also sustained for 2 minutes in Tore Supra (and 30 kA for 1 minute in the smaller superconducting Tokamak TRIAM-1M, where previously a steady-state discharge of one hour was demonstrated at very low density [170]).

Global LHCD efficiencies $\eta = \bar{n}_e R I_{CD} / P_{inj}$ of 0.35 and 0.27 $\times$ 10^{20} $AW^{-1}m^{-2}$ were achieved in JT-60 and JET respectively (see Fig. 6.4-1), and a strong dependence of η on the electron temperature was found. This may be explained by considering competing non-resonant absorption, which can reduce the current drive efficiency at low temperatures; at higher

temperatures the theory predicts a milder, but continuing rise [171]. Saturation effects, however, have been observed for full current drive at low density and high temperature on JET. These have been attributed to a local overdrive of the current and the resulting generation of negative electric fields [172].

A value of $\eta = 0.45 \times 10^{20}$ $AW^{-1}m^{-2}$ was estimated in an experiment combining ICRH and LHCD in JET [173]. Synergetic effects with electron cyclotron waves can also be invoked, but all of these effects are still to be fully assessed. Another type of synergy (LHW amplification using α-particle energy as a pump) was proposed [174], but wave amplification turns out to require very specific conditions, which are probably difficult to meet in ITER. Efficient LHCD at high density has been demonstrated in Alcator-C and recently in FT-U ($\eta_{CD} \approx 0.2 \times 10^{20}$ AW^{-1} m^{-2} at a density of 10^{20} m^{-3}; with full current drive at 0.5×10^{20} m^{-3}).

An important aspect is the capability of LHW to retain a high current drive efficiency in low and moderate β regions, owing to the strong Landau damping which occurs. This enabled the early constitution of an abundant database on LHCD, since it could be used for various purposes (current ramp-up with inductive flux saving, transformer recharging and sawteeth stabilization [175]), and yielded rather spectacular results in moderate size and low temperature tokamaks. This property, together with a weak sensitivity to electron trapping, supports the use of LHW to realize steady-state high performance operation in a reactor using "advanced" optimized shear scenarios. According to time-dependent simulations, this requires efficient current drive in the external half of the plasma column, both during the low density current ramp-up and the steady-state burn [166]. On the other hand, strong Landau damping will prevent the penetration of LHW to the core of high-β burning plasmas ($n_e T_e \leq 10–15 \times 10^{20}$ $m^{-3}keV$ must be satisfied at the location of innermost power deposition in ITER).

6.4.3. Current Profile Control and Improved Plasma Performance with LHCD

The effectiveness of LHCD for current profile control has been well documented in numerous experiments such as PLT, Petula, ASDEX, FTU, JT-60U: suppression of sawteeth, stabilization of the n=1, m=1-2 MHD modes, large variations of l_i [176-179]. For m = 2 modes, both a stabilizing and a destabilizing influence of LHCD were observed in some early experiments (PETULA, PLT, FT, ASDEX). Improved MHD stability at high beta with LHCD profile control has been shown on COMPASS [180].

Feedback control of the plasma internal inductance has been achieved in Tore Supra through variations of the launched power spectrum, $P(N_{||})$ [181]. Of potential interest for future applications, the use of composite spectra (ASDEX [182]) was shown to be effective in controlling the deposition zone (a low power component at large $N_{||}$ pulls out a suprathermal electron component, which then triggers the off-axis absorption of the main power fraction at lower-$N_{||}$). Similarly, two different launchers, producing respectively a narrow and a broad spectrum, were used in JT-60U to create reversed shear configurations with different radial locations, r_{qmin}, of the minimum of the safety factor q(r) (r_{qmin}/a from 0.4 to 0.75 [183]). In present-day tokamaks, even with low-$N_{||}$ narrow spectra, particular combinations of plasma profiles and operating parameters (n_e, I_p, B_t) can be chosen to prevent wave penetration into the plasma core and sustain reversed shear configurations with $r_{qmin} \approx$ 0.3-0.4 [172]. In elongated divertor plasmas, LH waves generally cannot propagate to the core region, which favours schemes requiring off-axis deposition. At JET, a large variety of q-profiles has been produced with LHCD using different power levels and pulse durations, with $q(0)$ up to 8 and $q_{min} \geq 4$ at the end of the current ramp-up [184].

Current profile modifications by LHCD were essential to reach some high performance regimes in recent experiments: optimized shear and improved hot-ion modes in JET [172], LHEP modes [185] with high-l_i, but either flat or hollow central current density in Tore Supra, and

reversed shear configurations with an internal confinement barrier (JET, Tore Supra, JT-60U, FT-U). Some of these configurations could be sustained in stable and stationary conditions. They can therefore provide a basis for optimized steady-state reactor scenarios, and the use of LHCD for producing and controlling transport barriers in reactor-grade plasmas deserves further investigations.

In JET, early LHCD is found to be the most efficient profile shaping method as compared to NBI and ICRH [184]. It provides an MHD stable route to high-β plasmas by establishing non-monotonic q-profiles at low-β, when the growth-rate of potentially deleterious MHD modes is small. The record performance shots in deuterium plasmas ($T_i(0)$ = 35 keV, $T_e(0)$ = 15 keV, core pressure of ~0.4 MPa) and D-T plasmas, are obtained with high power NBI and/or ICRH, following a short LHCD pulse during current ramp-up which forms a flat to slightly non-monotonic q-profile in the core.

In Tore Supra, FT-U and JT-60U, MHD stable reversed shear configurations have been sustained in stationary state (for durations longer than the current diffusion time) in partially driven and fully non-inductive discharges with conditions chosen so that the LH power deposition was well off-axis.

A global improvement of the confinement (with an enhancement factor, H_{89}, of up to 2) was obtained in LH-driven discharges in Tore Supra and TdeV. As an example, Fig. 6.4-2 represents the time traces of a 2 minute long LHEP discharge realized in Tore Supra, in which 90% of the current was driven non-inductively, with $T_e(0)$ = 7.5 keV, $n_e(0) = 2 \times 10^{19}$ m^{-3}, P_{LH} = 2.5 MW.

High bootstrap current fractions are achieved with combined LHCD and Fast Wave electron heating in Tore Supra. The bootstrap fraction rises to up to 50% and a confinement enhancement factor of about 2, relative to L-mode scaling, is then achieved. Finally, notched injection of LHW was successfully combined with repetitive pellet injection in ASDEX [186] and also on Tore Supra.

6.4.4. LH Power Coupling

Coupling of LHW to the plasma is achieved by antennas - or launchers - composed of multiple toroidal arrays of waveguides stacked in the poloidal direction, commonly named "grills" [187, 188]. The phasing of the waves at each waveguide aperture determines the phase velocity (or $N_{||}$) spectrum of the LH wave launched into the plasma. The coupling of LH waves from the launcher to the plasma is well understood and code predictions are in good agreement with detailed RF-field measurements at the launcher mouth in numerous experiments where local density measurements are available. Recent illustrations are provided by COMPASS, TdeV [189], Tore Supra, JET, and JT-60U. As was mentioned above the slow waves excited at the antenna with $N_{||} > 1$ can propagate into the plasma only if the density at the launcher mouth exceeds the cut-off density n_c. With normalization to the chosen LH frequency of 5 GHz on ITER, this can be expressed as follows:

$$n_c(\mathrm{m}^{-3}) = 3.1 \times 10^{17} \, (f_{\mathrm{GHz}} / 5)^2 \qquad (6.4.5)$$

Below this density, the wave is evanescent with a typical evanescent length which is of the order of a centimetre. As a consequence, a rapid decrease in the coupled power, and a corresponding increase in the reflected power, is found both in the experiments and in detailed code calculations as the plasma density at the launcher drops through the cut-off density. The electron density for which optimum coupling is achieved is roughly given by $n_{\mathrm{opt}} \approx n_c \, N_{||}^2$ [190], while the density range over which reflection coefficients are acceptable ($R \leq 5\%$) depends on the type of grill. This density range, relatively narrow in a conventional grill, is enlarged by the use of the multijunction concept [191, 192] where it spans about one order of magnitude (2 to 20 times the cut-off density). In the case of a Passive Active Multijunction [193], a weaker sensitivity near the cut-off density than with all-active waveguide multijunctions is predicted by numerical codes.

LHW antennas have been operated reliably at power densities (i.e. incident power / waveguide aperture area) which reach 25 MWm^{-2} at 3.7 GHz for low plasma reflection and which

scale roughly proportionally to the frequency (100 MWm^{-2} is achieved in routine operation at FT-U, working at 8 GHz [194]).

Under good coupling conditions (matched edge density), the full installed power could be used (Tore Supra, TdeV). Conversely, at large edge reflection, the maximum injected power is limited by the maximum value of the RF electric field inside the launcher structure. Statistical analyses of a large number of experiments, made independently at JET, Tore Supra, and TdeV, consistently yield a limit of 500 to 700 kVm^{-1} at 3.7 GHz.

Good coupling conditions have been achieved not only when the launcher was placed close to the plasma, so that the required density is 'naturally' provided by the scrape-off layer, but also at larger plasma-launcher distances (up to 15 cm in Tore Supra [195] and JT-60 [183, 196]). In such cases, the analysis in Tore Supra suggests that local absorption of LH power creates adequate plasma density for good coupling in front of the launcher. The LH power absorbed in the plasma edge region is small and does not affect the global plasma performance (e.g. the CD efficiency). Active control of the edge density by various means has also proved to be effective (proximity gas injection in JET [197] and TdeV, ECH resonant in the edge layers in COMPASS, positive divertor biasing in TdeV). The operating conditions for remote coupling need further investigation on present devices in order to provide a reliable basis for extrapolations to ITER.

In some conditions, "hot spots" have been observed on obstacles intersecting magnetic field lines connected to the launcher. Although a very small fraction of the total LH power is concerned, this lost power is concentrated in a narrow flux tube where the power density can reach several MWm^{-2}, so that action must be taken to avoid damage to plasma facing components. Experimental and theoretical investigations in progress [198,199] suggest that these hot spots result from small electrostatic spectral components at very large $N_{//}$ which accelerate cold edge electrons up to the keV energy range. New launcher developments aim at suppressing these parasitic effects by better geometrical shaping and by reducing the electric field at the antenna with a passive/active waveguide array.

6.4.5. LHW and H-mode Plasmas.

When the H-mode is triggered, the improvement in edge confinement leads to a steeper density gradient at the edge. This results in a smaller density decay length within the plasma scrape-off layer and, in general, the LHW coupling degrades. In JET, efficient coupling into H-modes ($R \leq 5\%$) was realized under close gas puffing, both in short ELM-free H-modes and in ELMy H-modes, with the launcher in the shadow of the poloidal limiters (7 to 8 cm from the separatrix). The amount of gas puffing necessary (2.5×10^{21} electrons/s) is 4 times less than the flow at which confinement begins to deteriorate in JET [197]. During ELMs, particles are expelled from the plasma and a fast modification of the density in the scrape-off layer occurs. However, reasonable coupling can be maintained in "grassy" ELMy H-mode ($R \leq 5\%$). Detailed analysis of the coupling data suggests that during the ELMs, transient high-density bursts may limit the power transmission capability [200]. In JT-60U standard operation, i.e. with a launcher-plasma distance of 6-8 cm, a large degradation of coupling has been observed at the L-H transition. However, good coupling was recovered, even in ELM-free H-modes, by shifting the plasma towards the launcher.

An ELM-free H-mode with LHW alone was reported on JT-60 in the limiter configuration for 3.3 s [201]. The power threshold for the H-mode was found to be low, around 1.5 MW. More recently, a reproducible ELMy H-mode was obtained on JET with 2.0-2.5 MW of LH power in D and D-T plasmas, without major coupling modifications during the L-to-H transition [202].

6.4.6. Interaction of LHW with Fast Ions

In ITER the LHW frequency must be large enough to avoid absorption by 3.5 MeV α-particles and *a fortiori* by any other ion population with lower velocities. A frequency of 5 GHz has thus been selected, based on theory and experiments [175, 203], and also on technological constraints (power sources, launcher design). In some low-frequency/high-density experiments,

evidence of LHW interaction with fast ions could be inferred through the generation of suprathermal ion tails and/or of 2.45 MeV neutrons produced by D-D reactions. More recently, with a frequency of only 2 GHz in JT-60U, the interaction of LHW with 350 keV ions originating from negative-ion-based neutral beams was expected and clearly demonstrated. The hard X-ray emission which characterizes the fast electron population produced by the LHW was strongly reduced in the central part of the plasma when neutral beam injection was applied and the plasma density was above a threshold which is consistent with theoretical calculations.

6.4.7. Theoretical Progress and Model Validation

The situation generally encountered in present-day tokamaks (multiple-pass damping) has long been a handicap to a detailed understanding of the propagation and absorption of LHW, due to a large sensitivity to small variations of the parameters. Standard ray-tracing/Fokker-Planck (RTFP) techniques have been implemented in large computer codes [204], but the stochastic nature of LH wave propagation in a toroidal plasma [205, 206] generally demands very extensive calculations to obtain reliable modeling with such codes in moderate temperature plasmas. This was fully appreciated only recently and led to significant progress [207-209]. The development of a theory [210] integrating stochastic wave diffusion and a Fokker-Planck treatment (WDFP), provided a paradigm for describing how the spectral gap between the velocities of the launched waves and of the pre-existing thermal electron population could easily be bridged in tokamaks through a self-regulating mechanism, and offered a numerically attractive alternative to ray-tracing in the regime of weak single-pass damping. In practice, both RTFP and WDFP techniques show that in such conditions, the wave energy actually fills-up, by multiple bouncing within the plasma cavity, the entire $(\boldsymbol{r}\text{-}\boldsymbol{k})$ domain between the wave propagation boundaries and the absorption limits.

The consequences of this theory on the temperature dependence of the current drive efficiency have been analyzed [211]. A weak temperature dependence can be explained by the fact

that the lower bound of the quasi-linear plateau in the electron distribution function is a few times larger than the thermal velocity and is determined by the onset of strong Landau damping. However, this effect is insufficient to explain the apparent linear dependence of current drive efficiency on temperature observed in many low temperature ($<T_e>$ below 1.5 keV) experiments. A second effect can be attributed to non-resonant absorption, or other edge losses, during the numerous reflections experienced by the wave in the low temperature, high Z, outer plasma layers, in weak single-pass damping conditions. The combination of these two effects in both the ray-tracing analysis and the wave diffusion model provides results which are in a good agreement with the observations [211]. The situation is simpler in ITER-like burn conditions, where single-pass resonant absorption prevails and, therefore, only the slow but continuous rise due to quasi-linear Landau effects and relativistic corrections remain.

These developments, as well as the progress of diagnostic techniques (X-ray cameras, magnetic and current profile measurements) and of their interpretative modeling, led to the present situation, in which RTFP and/or WDFP codes, with 2D-relativistic Fokker-Planck computations, can be routinely applied to model LHW discharges successfully in a number of devices (JET, Tore Supra, FT-U, TdeV, PBX-M) and a variety of plasma situations (including reversed-shear conditions). A comparison of measured and calculated LH deposition profiles for central and off-axis absorption is shown in Fig. 6.4-3. The agreement between experimental results and modeling now covers not only global parameters such as V_l, q_0, l_i, the current drive efficiency η, and X-ray emission profiles and spectra, but also their time evolution and the evolution of the plasma profiles [212, 213]. This agreement gives confidence in predictive modeling for ITER, but a better understanding of plasma transport is still necessary to fully assess the effect of magnetic shear optimization in tokamaks.

6.4.8. Heating and Current Drive in ITER

Projections of LHCD in ITER have indeed been made using time dependent computer simulations with the same transport model, both for sawteeth stabilization in an ignited 21 MA scenario and for advanced steady state operation at reduced plasma current [166]. In the pulsed high current case, current profile optimization can be achieved by LHCD. Ramping up the LH power to 50 MW during a 0.15 MAs^{-1} current rise phase provides non-monotonic *q(r)* profiles with a wide central region of flat, or slightly reversed, magnetic shear at the beginning of the current flat-top phase. Then, in the burning phase, due to the long resistive diffusion time, the weak or negative shear region shrinks slowly and the current profile reverts to a monotonic shape, although q-values can be kept above unity over the whole plasma cross-section for up to 600-1000 s, depending on various assumptions. Sawteeth could therefore be avoided in the simulations throughout the whole discharge duration. The q-profiles during flat-top at t = 500 s are compared in Fig. 6.4-4 for Ohmic ramp-up only and LH-assisted ramp-up, for cases in which 50 MW ICRH heating starts at the begin of the current flat-top. The ohmic power during ramp-up is also significantly reduced with LHCD thanks to the large enhancement of the current drive efficiency from the electric field in the outer half of the plasma.

In a steady-state advanced scenario with a plasma current of 13 MA, off-axis LHCD in the region r/a = 0.5-0.8 is used to create a wide magnetic shear reversal zone and to provide full current drive together with the bootstrap current. The transport model used in the JETTO calculations links the heat conductivities to the magnetic shear, reducing transport in the region of flat shear. A fusion power output of order 1 GW is thereby produced in steady state.

The sensitivity of these results to various assumptions on the transport models regarding, for example, the effect of shear reversal is studied by analyzing similar scenarios with codes such as ASTRA and CRONOS. When the dependence of transport coefficients on shear is suppressed, slightly lower temperatures are obtained and the sawtooth-free period is found to be reduced to about 800 s. For steady-state scenarios, access to optimized MHD-stable profiles and prescribed

fusion yields will require simultaneous control, on the resistive time scale, of the off-axis (LH) current generation, of the central heating and current drive power, and of the plasma fuel density. Assuming that real time estimates of the internal loop voltage can be obtained from magnetic equilibrium reconstructions, appropriate feedback loops on the heating and current drive systems would possibly allow the plasma to be controlled and maintained in the desired steady-state high-Q equilibrium. An example of such a scenario from a CRONOS simulation is shown in Fig. 6.4-5.

6.4.9. Technological Issues

The design of an LHCD system for ITER is based on a novel compact launcher with an alternate passive/active waveguide array facing the plasma, connected to large oversized hyperwaveguides which are fed at the rear from poloidal mode converters [214]. Standard circular waveguides transmit the power to the launcher from 1 MW unit CW klystrons operating at 5 GHz. Design of all components of the power plant and transmission line is based on existing technology. The new launcher elements of hyperwaveguides and mode converters have been qualified in testbed operation. An assessment of the coupling properties of passive/active grill arrays and integrated plasma tests of the new LHCD launcher concept on high performance elongated divertor plasmas in the ITER plasma operation regimes are still required.

A major issue is the coupling of the power from the grill antenna to the plasma, while maintaining low reflection, throughout the plasma build-up and burn phases. The electron density in front of the antenna must be kept above the cut-off density of $n_e=3.1 \times 10^{17}$ m^{-3} (for 5 GHz), independently of plasma configuration and changing plasma edge conditions. Long distance coupling has certainly been achieved on several machines with gas injection in the vicinity of the antenna and RF enhanced ionization. However, reliable coupling in the ITER operating regimes, with the antenna kept at a safe distance behind protection limiters, remains to be demonstrated.

6.5. NEUTRAL BEAM HEATING AND CURRENT DRIVE

6.5.1. Introduction

Neutral Beam (NB) injection has been successful in producing high temperature, high fusion performance plasmas in all of the large tokamaks operating world-wide. It has also demonstrated the capacity to drive current in the plasma and to produce plasma rotation. Furthermore, detailed experimental measurements of the basic processes by which the beams are trapped and subsequently couple their energy and momentum to the plasma are well understood and in good agreement with theoretical predictions. The high coupling efficiency is insensitive to the initial shape and/or configuration of the plasma and its (hydrogenic) isotopic composition. NB offers the flexibility of being able to heat the hydrogen plasmas envisaged during the initial phases of ITER operation by using beams of hydrogen atoms. It is also unaffected by any changes which may result from heating the plasma, e.g. ELM and sawtooth behaviour, transitions to different modes of confinement and subsequent changes to the plasma profile etc. During the D and D-T phases in the thermonuclear ignition and burn control scenarios the injectors would supply up to 50 MW of deuterium beams at 1 MeV. NB systems are designed to be capable of operation at full performance independently of the tokamak by using a calorimeter within the injector to intercept and measure the beam power and its profile. This feature has been, and will continue to be, a major factor in achieving the consistently high operational reliability obtained when the system is required to inject into the tokamak plasma.

The major criticism of NB systems relates to the limited range of target plasma density over which the power is deposited in the central region of the plasma. However, the range of operating density does not appear to have presented any serious restrictions to the applicability of NB injection in present systems. The heating characteristics do depend on plasma density: strong central ion heating is observed at low density and this has been advantageous for accessing high fusion performance in present generation devices. In high density H-modes (with strongly

coupled ions and electrons) confinement is similar for NB and centrally RF heated plasmas due to the dominant effect of the edge confinement barrier [215].

Nevertheless, the application of NB to ITER requires a fundamental change in the means by which the beams of energetic neutral atoms are produced. This is because of the requirement that the beams should penetrate to the centre of the large ITER plasma and this requires beam energies in the range of 250–500 keV/amu (0.5–1.0 MeV D^0). Neutral beams in this energy range cannot be produced by accelerating positive ions, due to the poor efficiency of neutralisation. Negative ion based systems must, therefore, be employed.

The high energy beams of negative ions are converted into fast atoms by electron stripping reactions with thermal gas molecules. The efficiency of this conversion process is ~60% (which is higher than that in the present high energy positive ion based systems). Efficiencies of ~80% are feasible should it become possible to use a highly ionized plasma instead of thermal gas molecules for the stripping reaction. It should also be noted, that, unlike positive-ion systems, there are no molecular negative ions and therefore there are no half and third energy components in the neutral beam, which is thus all at the full energy. Although the change to negative ion based neutral injection (N-NB) requires that a different emphasis is placed on some technological aspects, especially those related to the efficient generation and acceleration of high power and high voltage negative ion beams, the overall technology of the N-NB injector components is remarkably similar to that employed in current positive ion systems.

Major progress has already been achieved in the development and application of N-NB systems, in particular at JAERI, where a complete N-NB injector is already operational on the JT-60U tokamak. This N-NB system was designed to deliver up to 10 MW of neutral power at a beam energy of 500 keV for 10 s. It has already delivered 3.2 MW to the plasma, from one of the two sources on the beam line at a voltage of 350 keV using H^-, and a total of 4 MW for 2 s at 400 keV using D^- [216].

6.5.2. Interaction of Neutral Beams with Plasmas

Neutral beams injected into a tokamak plasma interact with the plasma through various processes. Several basic processes influencing heating and current drive performance of NB will be discussed in this section. The spatial dependence of the deposition of the beam power inside the plasma is determined mainly by the ionization cross-section of the neutral beam and the plasma electron density profile. The fast ions produced in the plasma slow down by interaction with the plasma electrons and ions. Fast ions are also observed to be lost via toroidal magnetic field ripple and interaction with MHD and other instabilities. These loss mechanisms are well understood theoretically. For example, the losses of beam-ions due to ripple trapping and stochastic diffusion of particles in banana-orbits in JT-60U (which has up to 3% TF ripple at the outer midplane) are typically <10%, as predicted theoretically and measured experimentally [217]. Ripple losses are largely avoided at low ripple amplitude or by optimising the injection geometry. For example, in the ITER EDA (24 coil) configuration the ripple loss fraction is computed to be from 0.8% to 12% for a 600keV D^0 beam, as the tangency radius is varied from 6m to zero [218].

Fast particle losses resulting from excitation of the Toroidal Alfvén Eigenmode (TAE) resonance have been investigated in present devices. For example, the effect on triton burn-up fraction in deuterium plasmas [219] was investigated, and the expected threshold, $v_{||} \approx v_A$, for significant fast particle loss was observed (where $v_{||}$ and v_A are the fast ion parallel velocity and the Alfvén velocity respectively). In D-T experiments [220] the stabilising effect of fast beam-ions on α-particle driven TAE modes was demonstrated, confirming the theoretical understanding of the underlying physics. In ITER, it would be possible to avoid the condition $v_{||} \approx v_A$ through the choice of beam energy and injection angle, and the ripple losses of beam-ions are expected to be <5% at plasma densities of $10^{20} m^{-3}$ by avoiding too perpendicular an injection angle. Minimisation of TAE loss is possible, except for the case of a high energy (>1 MeV) system optimised for central current-drive [218].

6.5.2.1. Neutral beam ionization cross-section

Neutral beam particles are basically deposited in plasmas by electron impact ionization, charge exchange and ion impact ionization in collisions with plasma electrons, ions and impurities [221]. There is abundant evidence showing that the ionization of the beams is well predicted with the already compiled cross-sections for these processes [222].

In addition to these atomic processes, neutral beams with energies of several hundreds of keV or higher, as required for ITER, suffer multi-step ionization, which arises from excitation of the beams and the subsequent ionization of already excited neutral atoms [223]. As a result, the effective ionization cross-sections are enhanced by the multi-step processes and theoretically the cross-sectional enhancement rises with increasing beam energy, E_b, or plasma electron density, n_e. The enhancement in the beam ionization by the multi-step processes has been observed in TFR [224], TFTR [225], JT-60 [226] and JET [227]. These experiments done with low energy (34-140 keV/amu) beams did not provide sufficient confidence to believe theoretical predictions on the multi-step ionization, as they occur at an energy range below the main increase in cross section. Recent shinethrough measurements of a 350 keV hydrogen beam in JT-60U [228] validated the theoretical enhancement, in that the enhancement in the beam stopping cross section (δ) of 0.8-1.05 obtained in the experiment was in good agreement with the theory by Janev [229]. Here, δ is defined by $\sigma_s = \sigma_s^{(0)} (1 + \delta)$, with σ_s being the effective beam stopping cross section taking multi-step processes into account, and $\sigma_s^{(0)}$ is the beam stopping cross-section if only impact and charge-exchange ionization from the ground state is considered. A comparison of the experimental enhancement with the prediction by Janev is shown in Fig. 6.5-1. Fairly good agreement is seen between theory and the experimental data, giving confidence in the use of the theory to estimate the beam ionization of 1 MeV deuterium beams (500 keV/amu) on ITER.

Computations of shine-through on ITER-FDR have been carried out using the ASTRA code over a wide range of conditions, which encompass the range of pre-ignited to ignited plasmas, using various assumed energies of the injected deuterium beam in order to examine the

overall parameter regimes for NB on ITER. Only under extreme conditions would the shinethrough fraction exceed 1%, for example at very high electron temperatures (40 keV) combined with low density ($0.35 \times 10^{20} m^{-3}$). However, such conditions would not arise in practice, because the α-heating power would be small at this low density (for example, during the non-ignited start-up phase, when the electron temperature would be much lower). In all ignited regimes, shinethrough is very low: 1% shine-through is small in terms of the NB performance. However, the power density on the first wall is not negligible and it must be carefully evaluated from the engineering point of view.

6.5.2.2. Beam-ion thermalization and plasma heating

The theory of the mechanism by which the fast ions heat the plasma, i.e. that of "classical slowing-down", is well developed. Classical slowing-down means that fast test particles in a plasma are decelerated by Coulomb interactions with plasma ions and electrons. Many years of experience have shown that NB ions generally heat tokamak plasmas with high efficiency. Reductions in heating efficiency have, however, been observed experimentally in non-optimal circumstances, due to various classes of orbit losses (e.g. from toroidal field ripple, or collective instabilities such as TAEs). However, such losses have been found to be in accord with theoretical expectations and, as noted earlier, can be minimised in the design.

Based on earlier work of Spitzer [230] and Sivukhin [231], Stix [232] derived the following formula for the slowing-down rate of beam ions in a plasma:

$$\frac{dE}{dt} = -\frac{2E}{\tau_s}\left[1+\left(\frac{E_{crit}}{E}\right)\right]^{3/2} \qquad (6.5.1)$$

where τ_s is the characteristic Spitzer slowing down time on field electrons and E_{crit} is the so-called critical energy. These are given by:

$$\tau_s = \frac{3\sqrt{2\pi}T_e^{3/2}}{\sqrt{m_e}m_b A_D}\ , \quad A_D = \frac{ne^4 \ln\Lambda}{2\pi\varepsilon_0^2 m_b^2} \tag{6.5.2}$$

$$E_{crit} = (\frac{3\sqrt{\pi}}{4})^{2/3}(\frac{m_i}{m_e})^{1/3}\frac{m_b}{m_i}T_e \tag{6.5.3}$$

For a pure hydrogen plasma (ion mass m_i),

$$E_{crit} = 14.8\frac{A_b}{A_i^{2/3}}T_e \tag{6.5.4}$$

The average time, τ, required for slowing injected ions of energy E_b down to thermal energy is

$$\tau = \frac{\tau_s}{3}\ln\left[1+\left(\frac{E_b}{E_{crit}}\right)^{3/2}\right] \tag{6.5.5}$$

For high energies of the beam ions the energy loss is mainly due to collisions with plasma electrons. The collisions with ions become more important when the beam ions are slowed down. At $E = E_{crit}$ the energy loss on ions and electron is equal. Below this energy ion collisions are dominant. The total energy transfer to plasma ions and electrons are equal for an injection energy of $E = 2.41\ E_{crit}$ [233]; at higher injection energies the electrons are predominantly heated [234].

Experimental tests. There are mainly two diagnostics giving information on the slowing-down of ions. Both use neutral particles originating from the ions and leaving the magnetic confinement field:

(1) Slowing-down ions are neutralized by charge exchange (CX) collisions with "cold" neutrals which are present in the plasma either as background or as a diagnostic beam. The energy distribution of the slowing-down ions can be inferred from the distribution of the CX neutrals. The slowing-down time can be determined directly by measuring the time lag between, for

example, the beginning of injection and the occurrence of a certain energy below the injection energy.

(2) Fast D^+ or T^+ ions can undergo nuclear reactions with plasma ions, thereby producing neutrons. Both the stationary neutron rate and the time constant of the neutron rate after switching the beam off can be checked for consistency with the concept of classical slowing-down.

The interpretation of such measurements is intricate because:

– the beams (usually consisting of hydrogen isotopes from positive ion sources) contain an energy spectrum with peaks at full, one half and one third energies, and neutron production depends very strongly on energy;

– the neutron production depends on the ion composition of the plasma;

– slowing-down depends on n_e, T_e, the hydrogenic composition and the fraction and charge state of impurity ions, which vary with the plasma radius;

– the deposition profile for each beam energy component has to be taken into account;

– "classical" losses of fast ions to either charge exchange or non-confined orbits have to be taken into account, and the orbits are sometimes not determined solely by the magnetic field but also by a "radial" electric field.

It is therefore not sufficient to take central or average parameters if theoretical values are to be compared with experiment. Instead, all the effects mentioned above have to be combined in a computer code which solves the Fokker-Planck equation for the whole profile as is done, for example, in FREYA [235] and incorporated in TRANSP [236].

In the earlier, smaller tokamaks, CX losses played a greater role than in the present generation experiments. Therefore, the main diagnostic was CX analysis. The beam ion spectra measured with this method agreed with spectra computed from classical theory within a factor of 2 [237-240].

Neutron measurements, as described by Jarvis [241], have become the main method for checking beam distributions in present large devices. In all tokamaks the measurements support the concept of classical slowing-down, for example in PLT [242], TFTR [243], DIII-D [237, 244,

245] and ASDEX Upgrade [246]. In JET, very good agreement with classical expectations was achieved, not only with deuterium beams, but also with tritium beams [247, 248]. An impressive extension of the comparison of calculation and experiment was made on JT-60U, where deuterium beams with energies up to 350 keV were used for injection [217]. The neutron emission rate and the decay time were measured during and after the negative ion based NBI (N-NBI) with a beam energy of 0.2 – 0.35 MeV. These quantities are compared with the theoretical predictions based on the classical slowing down of the injected beam ions, as shown in Fig. 6.5-2. In these experiments, E_b/E_{cr} was scanned from 13 to 34. Figure 6.5-2 indicates that the behaviour of the injected beam ions can be described by the classical slowing-down in the present experimental conditions. These experiments strongly support the assertion that N-NBI heating in ITER will also obey the classical theory.

The partition of energy deposition between ions and electrons has so far not been measured directly. The electron or ion energy balance in a plasma is so complicated that a direct determination of the power input is imprecise. In any case, the experiments involved are usually performed to determine heat diffusivities (χ_i and χ_e) and assume the classically-deposited beam power. Nevertheless, many experiments (e.g. [248]) show that the ion temperature and electron temperature in the plasma scale with the calculated beam input power and that, in the present generation of tokamaks, beams predominantly heat ions.

The simulations of heating next generation plasmas such as ITER have been described in [218, 249]. One of the main conclusions is that the minimum power required to reach ignition in the ITER EDA device is a slowly varying function of the D^0 beam energy $E(D^0)$ above about 400keV for beams with a tangency radius of 4m. In H-mode ignition scenarios, the principal determinant of the minimum power to reach ignition depends on the power needed to exceed the L-H transition threshold [250], which passes through a minimum at around 400 keV D^0 beam energy. In plasma conditions representative of the onset of ignition, the fraction of NB power delivered to the ions within $r/a \leq 0.45$ changes from about 70% at $E(D^0)$ = 400 keV to less than 30% at 2 MeV.

6.5.3. Neutral Beam Current Drive

6.5.3.1. Introduction

Several mechanisms for producing current parallel to the magnetic field in a tokamak plasma, in addition to conventional inductive drive, have been elaborated theoretically and confirmed experimentally. Any agency which is capable of producing a relative displacement of the mean values of the velocity distributions of groups of particles possessing different charges in the plasma constitutes a current drive mechanism. In the case of NB current drive, it is the parallel velocity component of the injected suprathermal ions which is responsible for a toroidal current, but this is partially shielded by the collisional response of the thermal electrons, as modified by the presence of the thermal ions. The current drive efficiency is mainly determined by basic characteristics of the fast-ion thermalization process, as described by the classical slowing-down theory. The process is, however, also strongly influenced by the presence of ions and electrons in trapped banana orbits in tokamak plasmas of low collisionality. It is evident from these considerations that the NB driven current density has a radial profile which is determined by the beam energy, deposition profile and injection angle. It is possible to optimize these aspects to some extent towards achieving a desired NB driven current profile shape, and to maximize the global current drive efficiency relative to the injected power. The theory of NB current drive is well developed, and is reviewed in §6.5.3.2. Experimental measurements have been obtained on several present-generation tokamaks, confirming the validity of the theory and also demonstrating that large values of the plasma current can be driven, up to 100% of the total in some cases.

6.5.3.2. Theory of NB current drive

The first theoretical explicit treatment of current drive in toroidal plasmas by directed fast ions was given by Ohkawa [251]. The fluid theory of Ohkawa did not, however, describe correctly the dependence of the driven current on measured plasma parameters in experiments [252], because it does not take into account several important effects which can only be treated by kinetic theory. In general, the velocity dependence of the frictional force, due to Coulomb collisions, between the fast ions and the electrons is different from that between the thermal ions and electrons, and this leads to a distortion of the electron velocity distribution compared with a Maxwellian. Secondly, electron-electron collisions, which result in a frictional drag between trapped and circulating electrons in toroidal geometry, are not taken into account. The latter effect, together with the reduction in the number of current-carrying electrons due to electron trapping, inhibits the opposing electron current flow. Since there can be near cancellation of the fast ion and electron currents, accurate calculation of the net current is only possible if the electron current is correctly determined. It may be noted that departure from a Maxwellian electron velocity distribution also occurs under the influence of a parallel electric field, as discussed in the fundamental Spitzer theory of plasma resistivity [253, 254]. In addition, the treatment of electron trapping and electron-electron interactions is analogous to the modification of Spitzer theory necessary to derive the neoclassical resistivity for toroidal plasmas.

In order to illustrate how the different physics effects mentioned above influence the net beam driven current, it is instructive firstly to examine the following simple relation, which expresses the result of an analytic Fokker-Planck treatment of the electrons [255], to give the beam driven current for a toroidal plasma in the large aspect ratio approximation and in the low collisionality banana regime, where it is assumed that the inequality $v_b << v_e$ holds for the fast ions and electrons respectively:

$$\frac{I}{I_f} = 1 - \frac{Z_f}{Z_{eff}} + 1.46\sqrt{\varepsilon}\,\frac{Z_f}{Z_{eff}}\,A\left(Z_{eff}\right) \qquad (6.5.6)$$

Here, I / I_f is the ratio of the net current to the fast ion current and $\varepsilon = r/R$ is the inverse aspect ratio. $A(Z_{eff})$ is a function whose value ranges from 1.67 for $Z_{eff} = 1$, to 1.18 for $Z_{eff} = 4$, and Z_f is the charge of the fast beam ions. In Eq. (6.5.6), the second term represents the electron current in the absence of trapped electrons and is in fact similar to the Ohkawa result, since the approximation of a displaced Maxwellian electron distribution holds for $v_b << v_e$. The third term is the reduction in the magnitude of the electron current due to the presence of trapped electrons. This term is minimum in the plasma center and tends to zero on-axis. The inequality $v_b << v_e$ is valid for hot plasmas such as those in NB current drive experiments in medium sized and large tokamaks, although more complete numerical solutions of the Fokker-Planck equation for the electrons have been performed (e.g. [256]) which is valid for any value of v_b / v_e.

The expression (6.5.6) may be applied locally in the plasma, thereby characterizing the beam driven current density at a given magnetic flux surface. In actual calculations of the beam driven current, it is necessary to use a NB power deposition code to determine the radial profile of the beam-ion source function. In computing the local fast-ion current density, j_f, 2-D Fokker-Planck or Monte Carlo calculation of the beam ion velocity distribution is normally performed, incorporating the effects of trapping of the unthermalized ions. The expression (6.5.6) is then used to compute the local ratio of net beam driven current to fast-ion current, j / j_f. The effect of fast-ion trapping is to reduce the local value of j_f: the proportion of the beam ions in trapped orbits depends on injection angle and deposition profile. In the absence of trapping, an analytic solution to the Fokker-Planck equation for the beam ions can be written as follows [257].

$$j_f = \frac{S\tau_s e Z_f v_o}{(1+u_c^2)} \int_0^1 f_1(u) u^3 du \qquad (6.5.7)$$

where τ_s is the fast ion slowing down time on the electrons, S is the local fast-ion source rate due to beam-deposition and u is the fast-ion velocity normalized to the injection velocity, v_0. The

distribution function, f_1, is the first-order Legendre polynomial component of the fast-ion velocity distribution and is given by,

$$f_1 = u^{2\beta}\left[\frac{1+u_c^3}{u^3+u_c^3}\right]^{1+2\beta/3} \tag{6.5.8}$$

with

$$\beta = \frac{m_i Z_{eff}}{2m_f \bar{Z}}\ , \quad u_c^3 = \frac{3\sqrt{\pi}}{4}\frac{m_e \bar{Z} v_{Te}^3}{m_i v_0^3}\ \text{, and} \quad \bar{Z} = \sum_i \frac{m_f n_i Z_i^2}{m_i n_e} \tag{6.5.9}$$

where the subscripts i and f refer to the plasma and fast ions, respectively.

The efficiency for generating the fast ion current is defined as the ratio of fast ion current density, j_f, to NB power deposited per unit volume, P_d (= $m_f v_0^2 S/2$). Evaluation of the above expressions shows that the highest efficiency is achieved by operating at the highest electron temperature and lowest density, in order to maximize τ_s, and by choosing the fast-ion energy to be close to the critical energy at which the effects of collisions with electrons and collisions with thermal ions are approximately equal. In practice, however, the choice of beam energy is determined by beam penetration requirements, particularly at the parameters proposed for ITER.

There are additional contributions to the total driven current arising from bulk rotation of the plasma ions due to unbalanced beam momentum input. This results in a parallel drift velocity, u_i, by the thermal ions in the same direction as the fast ion velocity. The effect of the rotating thermal ions is evaluated in [255], where it is shown that the thermal ion velocity distribution can be taken to be a displaced Maxwellian in the absence of electron trapping. The additional current arising from the parallel motion of the thermal ions is then exactly canceled by an additional electron current. In the presence of trapped electrons and under the condition $v_b << v_e$, an additional contribution to the driven current should be added to the right hand side of expression (6.5.6) equal to $\frac{nu_i}{Z_f n_b v_b} A(Z_{eff})$.

As pointed out in [255], this contribution can also be thought of as a component of the bootstrap current driven by the thermal ion flow. A complete kinetic description of the electrons would additionally have to include simultaneously the effects of the other driving terms of the bootstrap current (i.e., radial electric field and radial gradients of densities and temperatures). In the presence of beam-induced rotation, the fast ion current term, I_f, in Eq. (6.5.6) is reduced due to the down-shifting of the beam energy in the plasma frame [258] (hence lower τ_s). This is then the dominant effect on the total driven current, but the reduction is only significant if the toroidal rotation velocity, v_ϕ, is a significant fraction of v_b, unlike the situation in ITER. Further influences on beam driven current efficiency can, in principle, arise from redistribution of the fast ions, both radially and in velocity space due to the effects of MHD instabilities such as TAE, sawteeth, fishbones etc.

6.5.3.3. NB current drive experiments

The basic principles were first demonstrated experimentally in the Levitron device [252]. It may be noted that the Levitron results exhibited temperature and power scaling of the net driven current in agreement with the results from the numerical solution of the Fokker-Planck equation in which the inequality $v_b << v_e$ did not obtain. First tokamak results from DITE [259] demonstrated the expected density scaling of the driven current. Furthermore, currents driven by both co- and counter-injected beams were observed. Subsequently, in TFTR [258], of order of 0.34 MA NB driven current was obtained using 11.5 MW NB in low density plasmas, while in DIII-D [260] it was reported that the entire plasma current of 0.35 MA was maintained non-inductively using 10 MW of NB. Experiments on NB current drive have also been conducted in JET [261] and JT-60U [262]. On these devices, the injection angle is not sufficiently tangential to obtain high current drive efficiency, although two of the positive ion injectors on JT-60U were re-oriented to increase the tangential component. The recent realization of a tangentially oriented

500 keV, 10 MW negative ion NB system on JT-60U has greatly increased the potential for investigating and demonstrating NB current drive on that device.

Comparison of theoretical predictions and experimental measurements.

In experiments on non-inductive current drive, a significant change to the current profile following application of the externally driven current can only be expected over a timescale which is long compared with the resistive diffusion timescale. This is due to the fact that the driven currents induce local return currents in the plasma, via changes in the local toroidal electric field, which decay on a resistive timescale governed by radial diffusion of the poloidal magnetic field. The global field diffusion time required for j(r) to equilibrate everywhere (usually subject to the constraint that the total plasma current remains constant, under feedback control of the poloidal field system) is typically several seconds in present devices. However, local modification to j(r) can occur on a much faster timescale. The total non-inductive plasma current can in principle be computed from the expression:

$$I_{NI} = I - \int \sigma_{nc} E_{//} dA \qquad (6.5.10)$$

where I is the measured plasma current, σ_{nc} is the neoclassical conductivity, and the integral is over a poloidal cross-section. However, the local time-dependent parallel electric field, $E_{//}$, may not be directly available from measurements.

The non-inductive beam-driven current is usually inferred from the measured and predicted surface loop voltage and a realistic assumption about field diffusion. For example, in the JET experiments [261] a fully time dependent calculation of the surface loop voltage was carried out for a reference discharge using the TRANSP code [263], in which the NB and bootstrap driven currents were computed from the measured plasma profiles and from a numerical solution of the Fokker-Planck equation for the fast ions. This agreed well with the measured loop voltage,

indicating the validity of the non-inductive current computation. Equation (6.5.10) was also evaluated for many other NB-heated discharges, assuming radially constant $E_{//}$ derived from the measured loop voltage. The resultant interpreted non-inductive currents agreed well with the summed theoretical values of beam-driven and bootstrap contributions, computed for the measured plasma and beam deposition profiles. These JET results are illustrated in Fig. 6.5-3 [261].

The results from TFTR [258] were analyzed in a similar way, but in those experiments the bootstrap current was the dominant component. Up to 0.84 MA was driven non-inductively in a 0.9 MA discharge with 11.5 MW of NB, of which 61 % of the power was co-injected. The estimated contributions from beam driven and bootstrap currents were 0.34 MA and 0.50 MA respectively in this case.

In JT-60U [264], co- and counter-tangential beams were injected into low density ohmic plasmas, and the beam driven current was deduced from the difference in the loop voltage between co- and counter-NB, taking into account the difference in the bootstrap current between the two cases. There was good agreement between the experimentally deduced and the calculated driven currents, where the calculation is made by using the ACCOME code [265]. Within a limited database of NB current drive in JT-60U, the temperature and the beam energy dependence are also consistent with the theoretical predictions. Recent studies in DIII-D [266] used the EFIT code to identify the driven current profile, based on the measurement of the spatial profile of the loop voltage inside the plasma. The measured profile is consistent with numerical calculations without MHD modes.

Current drive with high-energy negative-ion NB.

Most of the present NB current drive experiments have been performed with the beam energy less than 150 keV, and underpin the validity of the present theory based on the classical slowing-down. In JT-60U, heating and current drive by using N-NB with a beam energy of around 0.35 MeV have been examined [217]. The measured N-NB driven current is compared

with the ACCOME code prediction in Fig. 6.5-4, where 2 MW of N-NB with a beam energy of 0.35 MeV was injected into a low current and low density discharge (I_p = 0.6 MA, $n_e = 0.7 \times 10^{19}$ m^{-3}). The ACCOME code predicted 80 kA of N-NB driven current, while the EFIT analysis showed 100 kA of beam driven current. A strongly peaked N-NB driven current was also identified by the EFIT analysis. Within the error bars, the identified driven current profile agrees with the ACCOME calculation, suggesting the reliability of the present theoretical prediction.

Exploitation of NB current drive towards steady-state operation and high performance plasmas.

The ability to modify the current profile and its evolution in order to produce plasmas with enhanced confinement and stability has been exploited in several devices. The high-β_p regime has been obtained with high proportions of total current driven by neutral beams. In DIII-D [260], the plasma current was sustained at 0.34 MA for 1.5 s at zero loop voltage. The estimated global L/R time of the plasma was estimated to be of order 2 s and it was concluded that the current was mainly due to the beam driven contribution, since the theoretical value was in the range 0.3 to 0.4 MA and the bootstrap contribution was estimated to be only 10-20% due to the flat density profile. In JT-60U the highest fusion performance has been obtained in the high-β_p mode, including the production of the highest fusion triple product of any experiment. These high performance scenarios have substantial non-inductive current components, of order 50%, dominated by bootstrap current [267]. At lower currents, in the region of 0.5 MA, high-β_p plasmas with full non-inductive current drive were obtained [262] in which 40 % of the current was driven by the tangential neutral injector. These plasmas displayed favourable confinement and stability characteristics: $\beta_p \approx$ 2.5-3, $\beta_N \approx$ 2.5-3.1 and $H_{89} \approx$ 1.8-2.2.

6.5.3.4. ITER predictions for NB current drive

In [218] the NB current drive efficiency was computed as a function of deuterium beam energy and tangency radius for the EDA ITER concept as it stood in 1993. Summary results are shown in Fig. 6.5-5 for a reference plasma with central parameters T_{e0}=25 keV, $n_{e0} = 1.5 \times 10^{20} m^{-3}$ and Z_{eff}=2, in terms of the current drive efficiency, $\eta_{CD} = n_e R_0 I_{CD}/P_{CD}$, where n_e is the line-averaged density ($10^{20} m^{-3}$), the driven current is in MA and the power, P_{CD}, in MW. η_{CD} is shown to be about 0.4 for a well optimised system. To drive 15 MA at $n_e = 10^{20} m^{-3}$ in such a plasma would therefore require some 300 MW of NB power, confirming that, for steady-state scenarios, a substantial bootstrap current component is required.

6.5.4. Plasma Rotation Induced by Neutral Beam

Plasma rotation is a universal phenomenon observed in tokamak plasmas heated by NB where the beams are injected at an angle to the radial direction from the major axis, i.e. where the tangency radius, R_T, is non-zero. The rotation occurs because of the transfer of the angular momentum of incident beam particles, measured in the tokamak rest frame, to the plasma particles. For the system as a whole, the initial angular momentum of the fast beam particles must be conserved by simple classical physics considerations.

NB is the only form of tokamak additional heating which imparts significant toroidal momentum to the plasma. Strongly rotating plasmas (up to several hundred krad/s) have been observed on many devices [268-271], usually by measuring Doppler shifted spectral lines from impurities rotating with the bulk plasma. The rotation speeds are universally much lower than would be predicted from neoclassical estimates of the radial momentum transfer via plasma viscosity [268] and therefore the literature has generally assumed that momentum transport in plasmas is anomalously high in a similar manner to energy transport [272]. Momentum confinement is discussed in detail in Chapter 2. An additional source of toroidal rotation arises

through E×B terms in the ion pressure balance, which are significant in regions of strong ion pressure gradient, such as in the H-mode transport barrier. In H-mode experiments in JET at moderate plasma current with RF heating [120], this contribution to the rotation is a factor of 2-3 less than that arising from direct NB momentum input at the same power.

6.5.4.1. Momentum transfer from beam ions to bulk plasma

The trajectory of an incoming neutral beam particle intercepts each flux surface at the midplane with a pitch angle (ξ) which varies with minor radius (r). Beam particles can either be ionized on the outboard of the plasma, in which case they become trapped ions, or further inboard, in which case they become passing ions circulating around the plasma toroidally. The criterion for trapping of ions at a flux surface is dependent on the inverse aspect ratio $\varepsilon = r / R$. For passing particles,

$$\xi = \frac{R_T}{R} > \xi_t = \sqrt{\frac{2\varepsilon}{1+\varepsilon}} \tag{6.5.11}$$

The absorbed toroidal angular momentum per beam particle is independent of the major radius of the birthplace of the fast ion (R_f) and is given solely by the beamline geometry:

$$L_f = m\xi v_b R_f = m v_b R_T \tag{6.5.12}$$

where m is the beam particle mass and v_b the beam particle velocity.

The transfer of this angular momentum from the NB ions to the main plasma proceeds by two mechanisms (both of which are observed in experiments):

– for all of the banana particles' angular momentum, by instantaneous torque due to radial movements of fast ions during their first orbit in the plasma, i.e. radial electric current

which produces j×B toroidal torque [273] (a small part of the passing particle momentum is also transferred in this way),

– for passing particles, mainly by collisional torque due to slowing-down of fast ions by Coulomb collisions on the background plasma [232, 274].

6.5.4.2. Observed time variation of plasma rotation with NB

Zastrow et al [275] have observed the time variation of rotation of JET plasmas subjected to strong NB heating. The rotation is observed from Doppler shifted line measurements of C^{6+} charge exchange recombination radiation. Figure 6.5-6 (a)-(c) shows the radial variation of the rotation of the plasma during the first ~250 ms of NB heating. Also shown are the calculated instantaneous torque from trapped beam fast ions (which is nearly the same for all three time slices), and the collisional slowing-down torque, which gradually builds up. It can be seen that the periphery of the plasma (where trapped particles dominate) is first to rotate, and that the rotation profile only begins to peak strongly once the slowing down of the beam is achieved. The transformation torque shown is the result of adding the mass of the beam ions once slowed down (i.e. rotating with the plasma) to the angular momentum of the plasma. The time variation in Fig. 6.5-6 (a)-(c) is good evidence of the two separate timescales for the two momentum transfer mechanisms.

6.5.4.3. Projected toroidal rotation from NBI momentum input in ITER

In [276], the plasma rotation in ITER produced by NB momentum input has been computed for various beam energies and target plasma densities. The computation requires a model for the radial transport of momentum, and the momentum diffusivity is assumed to be equal to the ion heat diffusivity, as observed experimentally [268, 270]. In [276], the underlying transport model is assumed to be of the mixed Bohm/gyro-Bohm type, which has been extensively

benchmarked on JET data. Results of these predictive calculations are shown in Figs. 6.5-7(a) and (b). The central angular velocity appears to be rather insensitive to beam energy, whilst the velocity at the location of the q=2 surface is quite strongly dependent on beam energy due to reduced penetration and higher specific momentum input per unit power input.

6.5.5. Negative-Ion Based Neutral Beam Development

Neutral beams with high energy, e.g. 1 MeV deuterium, are needed for ITER. Studies [276, 218] have shown that the minimum NB power to ignite ITER is not strongly dependent on beam energy above the 300-500 keV range (for deuterium). Nevertheless, these energies are much higher than those used in present systems. Fast ions are neutralized before being injected into a tokamak and the neutralization efficiency for fast ions is significantly different for positive and negative hydrogenic ions at beam energies beyond ~100 keV, as shown in Fig. 6.5-8. The neutralization efficiency of positive hydrogenic ions decreases rapidly for beam energies (keV/amu) above 100 keV. Therefore, the ITER NBI system must be based on negative-ion beam (N-NB) technology.

The major developments in N-NB have been carried out at JAERI in Japan, in conjunction with significant contribution from the group at CEA Cadarache, France. The operation of the N-NB injector on the JT-60U tokamak started in 1996 and has indicated both the feasibility and credibility of high energy, high power systems required for ITER.

6.5.5.1. N-NB on JT-60U

The design values for the first N-NB system on JT-60U are 10 MW of injected power for 10 s at 500 keV using negative ions of hydrogen or deuterium. Two ion sources plus accelerators, which are 25 m from the tokamak, are incorporated into a single beam line. The injection power has gradually increased and presently 3.6 MW at 350 keV for 0.6 s with

deuterium and 3.2 MW at 350 keV for 1 s with hydrogen have been achieved [278]. This promising early demonstration of the total system is fully consistent with the design values and further progress is expected. In addition to the technical success, the first operational periods have confirmed that the neutralization efficiency of a high power beam is 60%, as expected from cross-section data, and as shown in Fig. 6.5-8.

6.5.5.2. Development program

The N-NB reference design for ITER requires 40 A of D^- at 1.0 MeV and the major goals of the development program are to demonstrate the acceleration of a negative ion beam having good optics to 1 MeV and, in parallel, to develop a large negative ion source which will deliver a current density of D^- of 20 mA/cm^2 at an operating pressure in the source of < 0.3 Pa. Considerable progress has been achieved in both areas.

Beam acceleration. Using a conventional multi-aperture, multi-gap approach the group at JAERI has accelerated a beam to 975 keV with a total power supply drain current of 57 mA. The group at Cadarache has developed an alternative design of accelerator in which a group of beamlets are accelerated through a single aperture using a single gap [279]. This has produced a high quality beam of 40 mA at 860 keV.

Negative ion production. The JAERI group has developed a high efficiency ion source which has produced the required 20 mA/cm^2 at the required low filling pressure of 0.3 Pa. It also fulfils the requirement of having a low value of extracted electron current, which is measured to be 50% of the extracted negative ion current. Recent work has demonstrated that stable long-pulse operation is not a problem: a source has been operated continuously for 140 hours without difficulty. This work has also demonstrated that the consumption rate of Cs (which is introduced in order to enhance the yield of negative ions) is sufficiently low that a single dosage of 600 mg was sufficient for more than 120 hours of operation. Measurements made after 140 hours of continuous operation, and also after 8 months of intermittent operation, of the JT-60U N-NB

system revealed that approximately 90% of the Cs was retained inside the plasma generator. Surface contamination was measured to be ~1 $\mu g cm^{-2}$ at a distance of one meter from the source, which is acceptable.

Plasma neutralizer. The development of a plasma neutralizer for ITER is being carried out at the Kurchatov Institute. If successful, this would enable the efficiency of conversion of the negative ions to fast neutrals to be increased from the present value of 60% to ~80%. Plasma production is by a microwave discharge and, following the successful demonstration of the technique in a system 0.6 m long, a larger 2.4 m long system is being designed. Using a microwave source at 7 GHz, the maximum value of target thickness will be $\sim 1.5 \times 10^{14}$ cm^{-2} .

Technology. The large ion source/accelerator structures require very large diameter alumina insulators which exceed the presently available manufacturing technology. A new fabrication technique which is scaleable to 3 m diameter has been developed. The high-voltage bushing for the 1 MeV transmission line is a critical component and a model bushing is therefore being fabricated for HV testing.

6.5.6. Conclusion

The kinetic theory of beam plasma heating, current drive and plasma rotation is well developed. The validity of theoretical predictions has been successfully established by comparison with a large number of experiments, from the first confirmation of the basic effects in the Levitron device, through demonstration of quantitative agreement of the theory with measurements from all the major tokamaks, to the most recent results with ITER-relevant injector parameters using N-NB on JT-60U. Experiments have shown that NB plasma heating is generally efficient. In addition, NB current drive is able to support a large proportion of the total current, up to 100% in some cases, and it can be used to help sustain current profiles leading to enhanced plasma performance. The majority of the physics database used to design ITER has been acquired from present generation tokamaks using NB based on positive ion systems. The advances made in the

production and acceleration of high energy negative ion systems lead to the conclusion that NB with beam energies in the region of 1 MeV can play a major role on ITER as a credible and predictable method of heating the plasma to ignition. The provision of central current drive by high energy beams has been shown to be consistent with predictions and could also be applied to the advanced scenarios of ITER. An additional unique capability, which may be crucial to ITER, is the proven capability of NB to produce rotation of the plasma in order to prevent the growth of locked modes.

REFERENCES

[1] H-MODE DATABASE WORKING GROUP, Nucl. Fusion **36** (1996) 1217.

[2] WILHELM, R., Plasma Phys. Contr. Fusion **40** (1998) A1.

[3] START, D.F.H. et al., Phys. Rev. Lett. **80** (1998) 4681.

[4] ERCKMANN, V. and GASPARINO, U., Plasma Phys. Control. Fusion **36** (1994) 1869.

[5] LLOYD, B., Proc. 10th Joint Workshop on ECE and ECH, Ameland, World Scientific, Singapore (1997) 443.

[6] PRATER, R., J. of Fusion Energy **9** (1990) 19 - 30.

[7] ALIKAEV, V.V., et al., Plasma Physics and Controlled Nuclear Fusion Research 1994, (Proc. 15th Int. Conf., Seville, 1994) Vol. 1, IAEA, Vienna (1995) 157.

[8] BORNATICI, M., et al., Nucl. Fusion **23** (1983) 1153.

[9] LITVAK, A.G., *High-Frequency Plasma Heating*, American Institute of Physics, New York, 1992.

[10] JAMES, R.A., et al., Phys. Rev. **A45** (1992) 8783.

[11] ALIKAEV, V.V., et al., Nucl. Fusion **32** (1992) 1811.

[12] GASPARINO, U., et al., Proc. Int. Workshop on Theory of Fusion Plasmas, Varenna, Italy (1990) 195.

[13] LUCE, T.C., et al., "Current profile Modification with Electron Cyclotron Current Drive in the DIII-D Tokamak", Fusion Energy 1998, (Proc. 17th Int. Conf. Yokohama, 1998), paper IAEA-F1-CN-69/CD2/EX9/5 (to be published).

[14] COHEN, R.H., Phys. Fluids **30** (1988) 2442.

[15] FISCH, N.J., Rev. Mod. Phys. **59** (1987) 175.

[16] GIRUZZI, G., et al., "Current Drive and Profile Control in NET Plasmas", FOM-Instituut voor Plasmafysica, Rijnhuizen, Nieuwegein, 1989.

[17] SMITH, G.R., et al., Phys. Fluids **30** (1987) 3633.

[18] HARVEY, R.W., et al., Phys. Rev. Lett. **62** (1989) 426.

[19] HARVEY, R.W. and McCOY, M.G., "The CQL3D Fokker-Planck Code", General Atomics, 1992.

[20] O'BRIEN, M.R., et al., ., Proc. IAEA Tech. Committee Meeting on Advances in Simulation and Modelling of Thermonuclear Plasmas (Montréal, 1992), Vol. 1, IAEA, Vienna (1992) 527.

[21] WESTERHOF, E., Proc. 9th Joint Workshop on ECE and ECH, Borrego Springs, World Scientific, Singapore (1995) 39.

[22] TODD, T.N., et al., Plasma Phys. Control. Fusion **35** (1993) B231.

[23] POLMAN, R.W., et al., Controlled Fusion and Plasma Physics, (Proc. 23rd Euro. Conf., Kiev, 1996) Vol. 20C, Part II, European Physical Society, Geneva (1996) 934.
[24] ALIKAEV, V.V., et al., Nucl. Fusion **35** (1995) 369.
[25] POLMAN, R.W., et al., Controlled Fusion and Plasma Physics, (Proc. 24th Euro. Conf., Berchtesgaden, 1997) Vol. 21A, Part II, European Physical Society, Geneva (1997) 605.
[26] ERCKMANN, V., et al., Plasma Phys. Control. Fusion **34** (1992) 1917.
[27] ERCKMANN, V., et al., Fusion Engineering and Design **26** (1995) 141.
[28] HARVEY, R.W., et al., Nucl. Fusion **37** (1997) 69.
[29] JAHNS, G.L., et al., Nucl. Fusion **26** (1986) 226.
[30] BAGDASAROV, A.A., et al., Plasma Physics and Controlled Nuclear Fusion Research 1990, (Proc. 13th Int. Conf., Washington, 1990) Vol. 1, IAEA, Vienna (1991) 523.
[31] GIANNONE, L., et al., Nucl. Fusion **32** (1992) 1985.
[32] GORINI, G., et al., Phys. Rev. Lett. **71** (1993) 2038.
[33] LUCE, T.C., et al., in *Local Transport Studies in Fusion Plasmas*, Villa Monastero, Varenna, Editrice Compositori, Bologna, 1993, 155.
[34] RYTER, F., et al., Controlled Fusion and Plasma Physics, (Proc. 23rd Euro. Conf., Kiev, 1996) Vol. 20C, Part II, European Physical Society, Geneva (1996) 11.
[35] LUCE, T.C., et al., Plasma Physics and Controlled Nuclear Fusion Research 1990, (Proc. 13th Int. Conf., Washington, 1990) Vol. 1, IAEA, Vienna (1991) 631.
[36] LOHR, J., et al., Phys. Rev. Lett. **60** (1988) 2630.
[37] HOSHINO, K., et al., Phys. Rev. Lett. **69** (1992) 2208.
[38] FIELDING, S.J., et al., Plasma Phys. Control. Fusion **38** (1996) 1091.
[39] ERCKMANN, V., et al., Phys. Rev. Lett. **70** (1993) 2086.
[40] PRATER, R., et al., Plasma Physics and Controlled Nuclear Fusion Research 1988, (Proc. 12th Int. Conf. Nice, 1988) Vol. 1, IAEA, Vienna (1989) 527.
[41] FIELDING, S.J., et al., Plasma Phys. Control. Fusion **40** (1998) 731.
[42] LLOYD, B., et al., Nucl. Fusion **31** (1991) 2031.
[43] PEREVEREV, G.V., Plasma Physics and Controlled Nuclear Fusion Research 1988, (Proc. 12th Int. Conf. Nice, 1988) Vol. 1, IAEA, Vienna (1989) 739.
[44] MAROLI, C. and PETRILLO, V., Nuovo Cimento **10D** (1988) 677.
[45] FIDONE, I. and GRANATA, G., Nucl. Fusion **34** (1994) 743.
[46] LLOYD, B., et al., Plasma Phys. Control. Fusion **38** (1996) 1627.
[47] JOTAKI, E. and ITOH, S., "ECR Discharge Cleaning for TRIAM-1M", Kyushu University Report FURKU 97-03(44), 1997.

[48] SAUTER, O., et al., Phys. Plasmas **4** (1997) 1654.
[49] WESSON, J.A., et al., Nucl. Fusion **29** (1989) 641.
[50] WESTERHOF, E., Nucl. Fusion **30** (1990) 1143.
[51] KISLOV, D.A., et al., Nucl. Fusion **37** (1997) 339.
[52] ZOHM, H., et al., "Experiments on Neoclassical Tearing Mode Stabilisation by ECCD in ASDEX Upgrade", Nucl. Fusion 1999 (accepted for publication).
[53] McCARDLE, G.J., et al, Proc. 9th Joint Workshop on ECE and ECH, Borrego Springs, World Scientific, Singapore (1995) 271.
[54] ZOHM, H., Phys. Plasmas **4** (1997) 9.
[55] ZOHM, H., Plasma Phys. Control. Fusion **38** (1996) 105.
[56] LOHR, J., et al., "The Effect of Edge Resonant Electron Cyclotron Heating on Edge Localized Modes in a Tokamak", General Atomics, San Diego, 1991.
[57] MORRIS, A.W., et al., Plasma Physics and Controlled Nuclear Fusion Research 1994, (Proc. 15th Int. Conf., Seville, 1994) Vol. 1, IAEA, Vienna (1995) 365.
[58] ZAKHAROV, L., et al., "The Theory of Stabilization of Sawtooth Oscillations in TFTR Supershots", Princeton Plasma Physics Laboratory, 1993.
[59] BHATNAGAR, V.P., et al., Nucl. Fusion **34** (1994) 1579.
[60] WHITE, R.B., et al., in *Magnetic Reconnection and Turbulence*, Editions de Physique, Orsay, 1995.
[61] EDGECOMBE, C.J., *Gyrotron Oscillators, Their Principles and Practice*., Taylor & Francis, London, 1993.
[62] NELSON, S.D., et al., Proc. 11th Topical Conf. on Radio Frequency Power in Plasmas, Palm Springs (1995) 441.
[63] SAKAMOTO, K., et al., Phys. Rev. Lett. **73** (1994) 3532.
[64] KOSMAHL, H.G., Proc. IEEE **70** (1982) 1325.
[65] BRAZ, O., et al., Proc. 22nd Int. Conf. on Infrared and Millimeter Waves, Wintergreen (1997) 144.
[66] ADAM J., Plasma Phys. Control. Fusion **29** (1987) 443.
[67] KOCH, R. and VAN EESTER, D., Plasma Phys. Contr. Fusion **35** (1993) A211.
[68] BRAMBILLA, M., *Kinetic Theory of Plasma Waves – Homogeneous Plasmas*, Clarendon Press, Oxford (1998).
[69] STIX, T.H., *Waves in Plasmas*, American Institute of Physics (1992).
[70] SWANSON, D.G., *Plasmas Waves*, American Institute of Physics (1989).
[71] CAIRNS, R.A., *Radio Frequency Heating of Plasmas*, Adam Hilger, Bristol (1991).
[72] KOCH, R., Second Carolus Magnus Summer School on Plasma Physics, Aachen, 1995, Transactions on Fusion Technology **29** (1996) 241.

[73] FAULCONER, D.W., Second Carolus Magnus Summer School on Plasma Physics, Aachen, 1995, Transactions on Fusion Technology **29** (1996) 237.

[74] BÉCOULET, A., Plasma Physics and Controlled Fusion **38** (1996a) A1.

[75] MAYBERRY, M.J., et al., Nucl. Fusion **30** (1990) 579.

[76] CARTER, M.D., et al., Nucl. Fusion **36** (1996) 209.

[77] TELESCA, G., et al., Radio Frequency Heating and Current Drive of Fusion Devices, (Proc. 1st Euro. Topical Conf., Brussels, 1992) Vol. 16E, European Physical Society, Geneva (1992) 133.

[78] JACQUINOT, J., et al., Plasma Phys. Control. Fusion **33** (1991) 1657.

[79] D'IPPOLITO, D.A., "Analysis of RF Sheaths for the ITER Ion Cyclotron Antenna", Final Report for ITER Task D211.2, ITER Document Nº ITER/US/96/IV-RF-03 (1996).

[80] MESSIAEN, A.M., et al., Plasma Phys. Control. Fusion **31** (1989) 921.

[81] KIMURA, H., et al., Plasma Phys. Control. Fusion **35** (1993) 845.

[82] NOTERDAEME, J.-M., et al Radio Frequency Heating and Current Drive of Fusion Devices, (Proc. 2nd Euro. Topical Conf., Brussels, 1998) Vol. 22A, European Physical Society, Mulhouse (1998) 9.

[83] START, D.F.H., et al., Proc. 11th Topical Conf. on Radio Frequency Power in Plasmas, Palm Springs, AIP, New York (1995) 355.

[84] VAN NIEUWENHOVE, R., et al., Nucl. Fusion **32** (1992) 1913.

[85] NOTERDAEME, J.-M., et al., Proc. 11th Topical Conf. on Radio Frequency Power in Plasmas, Palm Springs, AIP, New York (1995) 47.

[86] SAIGUSA, M., et al., Nucl. Fusion **34** (1994) 276.

[87] NOTERDAEME, J.-M., et al., Controlled Fusion and Plasma Physics, (Proc. 23rd Euro. Conf., Kiev, 1996) Vol. 20C, Part II, European Physical Society, Geneva (1996a) 723.

[88] KIMURA, H., et al., Fusion Energy 1996, (Proc. 16th Int. Conf., Montréal, 1996), Vol. 3, IAEA, Vienna (1997) 295.

[89] GOULDING, R.H., et al., Proc. 11th Topical Conf. on Radio Frequency Power in Plasmas, Palm Springs, AIP, New York (1995) 397.

[90] BEAUMONT, B., et al., "Support to ICRF System Design", CEA NOTE TECHNIQUE: NT/CH/97/02, Rapport Final ERB 5000 CT 950118 (1997a).

[91] SIMON, M., et al., Radio Frequency Heating and Current Drive of Fusion Devices, (Proc. 2nd Euro. Topical Conf., Brussels, 1998) Vol. 22A, European Physical Society, Mulhouse (1998) 105.

[92] KOCH, R., et al., Plasma Phys. Control. Fusion **40** (1998) A191.

[93] BRAMBILLA, M. Computer Phys. Reports **4** (1986) 1.

[94] KOCH, R., et al., Computer Physics Communications **40** (1986) 1.

[95] ITOH, K., et al., Nucl. Fusion **24** (1984) 13.

[96] VILLARD, L., et al., Computer Physics Reports **4** (1986) 95.

[97] EDERY, P., et al., "Numerical Modelling of RF Waves in the Ion Cyclotron Range of Frequency for Tokamak Plasmas", Rep. EUR-CEA-FC-1334, Association Euratom-CEA. St. Paul lez Durance (1987).

[98] BRAMBILLA, M. and KRÜCKEN, T., Nucl. Fusion **28** (1988) 1813.

[99] BÉCOULET, A., "Validation Exercise on Power Deposition Profile Codes ', CEA NOTE TECHNIQUE : P/CH/96/003, Rapport Final ERB 5000 CT 950063 (1996b).

[100] KESNER, J., Nucl. Fusion **18** (1978) 781.

[101] KERBEL, G.D. and McCOY, M.G., Phys. Fluids **28** (1985) 3629.

[102] SUCCI, S., et al., Computer Physics Communications **40** (1986) 137.

[103] KENNEL, C.F. and ENGELMANN, F., Phys. Fluids **9** (1966) 2377.

[104] KOVANEN, M.A., et al., Nucl. Fusion **32** (1992) 787.

[105] CARLSSON, J., et al., Theory of Fusion Plasmas, (Proc Joint Varenna-Lausanne Workshop, Varenna, 1994), Editrice Compositori, Bologna (1994) 351.

[106] HEIKKINEN, J.A. and SIPILÄ, S.K., Nucl. Fusion **37** (1997) 835.

[107] BOUCHER, D., Proc. IAEA Tech. Committee Meeting on Advances in Simulation and Modelling of Thermonuclear Plasmas (Montréal, 1992), Vol. 1, IAEA, Vienna (1992) 142.

[108] LOUCHE, F. and KOCH, R., "Final Report on ITER subtask D350.1: Modelling of ICRH system heating performances with PION/PRETOR package", LPP-ERM/KMS Brussels Report nº116 (1999).

[109] ERIKSSON, L.-G., et al., Nucl. Fusion **33** (1993) 1037.

[110] ERIKSSON, L.-G., et al., Proc. 1998 Int. Congress on Plasma Physics & 25th Euro. Conf. on Controlled Fusion and Plasma Physics, (Prague, 1998) Vol. 22C, European Physical Society, Mulhouse (1998) 1186.

[111] PINSKER, R.I., et al., Proc. 9th Topical Conf. on Radio Frequency Power in Plasmas, Charleston, AIP, New York (1991) 105.

[112] TAKASE, Y., et al., Phys. Plasmas **4** (1997) 1647.

[113] NOTERDAEME J.-M., et al., Fusion Energy 1996, (Proc. 16th Int. Conf., Montréal, 1996) Vol. 3, IAEA, Vienna (1997) 335

[114] MESSIAEN, A.M., et al., Plasma Phys. Control. Fusion **32** (1990) 889.

[115] KIMURA, H., et al., Fusion Eng. and Design **26** (1995) 95.

[116] BEAUMONT, B., et al., Proc. 12th Topical Conf. on Radio Frequency Power in Plasmas, Savannah, AIP, New York (1997b) 23.

[117] WILSON, J.R., et al., Proc. 10th Topical Conf. on Radio Frequency Power in Plasmas, Boston, AIP, New York (1993) 36.

[118] BHATNAGAR, V.P., et al., Proc. 9th Topical Conf. on Radio Frequency Power in Plasmas, Charleston, AIP, New York (1991) 115.

[119] MESSIAEN, A.M., et al., Proc 12th Topical Conf. on Radio Frequency Power in Plasmas, Savannah, AIP, New York (1997) 41.

[120] ERIKSSON, L.-G., et al., Plasma Phys. Control. Fusion **39** (1997) 27.

[121] GREENWALD, M., et al., "H-mode Regimes and Observations of Central Toroidal Rotation in Alcator C-Mod", Fusion Energy 1998, (Proc. 17th Int. Conf., Yokohama, 1998), paper IAEA-CN-69/EX1/4(C1,C2) (to be published).

[122] BHATNAGAR, V.P., et al., Nucl. Fusion **33** (1993) 83.

[123] McGUIRE, K.M., et al., Fusion Energy 1996, (Proc. 16th Int. Conf., Montréal, 1996), Vol. 1, IAEA, Vienna (1997) 19.

[124] ROGERS, J.H., et al., Fusion Energy 1996, (Proc. 16th Int. Conf., Montréal, 1996) Vol. 3, IAEA, Vienna (1997) 317.

[125] START, D.F.H., et al., Plasma Phys. Control. Fusion **40** (1998) A87.

[126] ITER CONFINEMENT DATABASE AND MODELING WORKING GROUP (presented by J.G. CORDEY) Plasma Phys. Control. Fusion **39** (1997) B115.

[127] JACQUINOT, J., et al., Controlled Fusion and Plasma Physics, (Proc. 24th Euro. Conf., Berchtesgaden, 1997), Vol. 21A, Part IV, European Physical Society, Geneva (1997) 1865.

[128] BHATNAGAR, V.P., et al., Controlled Fusion and Plasma Physics, (Proc. 24th Euro. Conf., Berchtesgaden, 1997), Vol. 21A, Part I, European Physical Society, Geneva (1997) 77.

[129] FISCH, N.J., Rev. Mod. Phys. **59** (1987) 175.

[130] BHATNAGAR, V.P., et al., Nucl. Fusion **34** (1994) 1579.

[131] HELLSTEN, T., et al., Phys. Rev. Lett. **74** (1995) 3612.

[132] BHATNAGAR, V.P., et al., Proc. 1998 Int. Congress on Plasma Physics & 25th Euro. Conf. on Controlled Fusion and Plasma Physics, (Prague, 1998) Vol. 22C, European Physical Society, Mulhouse (1998) 1402.

[133] NOTERDAEME, J.-M., et al., "Comparing high power ion cyclotron resonance frequency heating with neutral injection in ASDEX Upgrade: differences, similarities and synergies", Fusion Energy 1998, (Proc. 17th Int. Conf., Yokohama, 1998), paper IAEA-CN-69/CDP/11 (to be published).

[134] PORKOLAB, M., et al., Plasma Phys. Control. Fusion **40** (1998) A35.

[135] VAN EESTER, D. and KOCH, R., Plasma Phys. Control. Fusion **40** (1998) 1949.

[136] GORMEZANO, C., Plasma Phys. Control. Fusion **40** (1998) A171.

[137] GORMEZANO, C., et al., Fusion Energy 1996, (Proc. 16th Int. Conf., Montréal, 1996), Vol. 1, IAEA, Vienna (1997) 487.

[138] USHIGUSA, K., et al., "RF heating and current drive studies in JT-60U", Proc. 12th Topical Conf. on Radio Frequency Power in Plasmas, Savannah, AIP, New York (1997) 111.

[139] PRATER, R., et al., Fusion Energy 1996, (Proc. 16th Int. Conf., Montréal, 1996) Vol. 3, IAEA, Vienna (1997) 243.

[140] KOCH, R., et al., Plasma Phys. Control. Fusion **37** (1995) A291.

[141] SAOUTIC, B., et al., Phys. Rev. Lett. **76** (1996) 1647.

[142] MAJESKI, R., et al., Proc 12th Topical Conf. on Radio Frequency Power in Plasmas, Savannah, AIP, New York (1997) 73.

[143] ONO, M., Phys. Fluids **B5** (1993) 241.

[144] LEBLANC, B., et al., Proc. 1998 Int. Congress on Plasma Physics & 25th Euro Conf. on Controlled Fusion and Plasma Physics, (Prague, 1997) Vol. 22C, European Physical Society, Mulhouse (1998) 1218.

[145] EQUIPE TORE SUPRA (presented by B. Saoutic), Plasma Phys. Control. Fusion **3 6** (1994) B123.

[146] PETTY, C.C., et al., Phys. Rev. Lett. **69** (1992) 289.

[147] PETTY, C.C., et al., Proc. 9th Topical Conf. on Radio Frequency Power in Plasmas, Charleston, AIP, New York (1991) 96.

[148] MURAKAMI, M., et al., Proc 10th Topical Conf. on Radio Frequency Power in Plasmas, Boston, AIP, New York, (1993) 48.

[149] BÉCOULET, A., et al., Phys. Plasmas **1** (1994) 2908.

[150] EQUIPE TORE SUPRA (presented by X. Litaudon), Plasma Phys. Control. Fusion **38** (1996) A251.

[151] MAJESKI, R., et al., Phys. Rev. Lett. **76** (1996) 764.

[152] KIMURA, H., et al., Proc. IAEA Tech. Committee Meeting on FWCD in reactor scale tokamaks, Arles (1991) 260.

[153] PRATER, R., et al., Proc. IAEA Tech. Committee Meeting on FWCD in reactor scale tokamaks, Arles (1991) 308.

[154] LYSSOIVAN, A.I., et al., Nucl. Fusion **32** (1992) 1361.

[155] LYSSOIVAN, A.I., et al., Radio Frequency Heating and Current Drive of Fusion Devices, (Proc. 2nd Euro. Topical Conf., Brussels, 1998) Vol. 22A, European Physical Society, Mulhouse (1998) 85.

[156] DE LA CAL, E. and GAUTHIER, E., Plasma Phys. Control. Fusion **39** (1997) 1083.

[157] LYSSOIVAN, A.I., et al., Controlled Fusion and Plasma Physics, (Proc. 24th Euro. Conf., Berchtesgaden, 1997), Vol. 21A, Part IV, European Physical Society, Geneva (1997) 1741.

[158] GOULDING, R.H., et al., "Advanced ICH Antenna Designs for Heating and CD on ITER and NSTX", Fusion Energy 1998, (Proc. 17th Int. Conf., Yokohama, 1998), paper IAEA-CN-69/FTP/22 (to be published).

[159] ITER Final Report for Task No G 51 TT 07, "ICRF Antenna Technology and Vacuum Transmission Line Development" (ITER Technology Task T361) (1998)

[160] KUMAZAWA, R., et al., Fusion Technology 1996, (Proc. 19th Symp., Lisbon, 1996) Vol. 1, Elsevier, Amsterdam (1997) 617.

[161] WÉGROWE, J.-G., Fusion Tech. **7** (1985) 250.

[162] FISCH, N.J., Phys. Rev. Lett. **41** (1978) 873.

[163] KARNEY, C.F.F., Phys. Fluids **20** (1978) 1084.

[164] WÉGROWE, J.-G., et al., Comments on Plasma Phys. and Control. Fusion **8** (1984) 6.

[165] GOLANT, V.E., Zhurnal Tekhnicheskoi Fiziki **41** (1971) 2492.

[166] BOUCHER, D., et al., Fusion Energy 1996, (Proc. 16th. Int. Conf., Montréal, 1996) Vol. 2, IAEA, Vienna (1997) 945.

[167] GORMEZANO, C., et al., Controlled Fusion and Plasma Heating, (Proc. 13th Euro. Conf., Schliersee, 1986) Vol. 10C, Part II, European Physical Society, Geneva (1986) 311.

[168] IKEDA, Y., et al., Plasma Physics and Controlled Nuclear Fusion Research 1994, (Proc. 15th Int. Conf., Seville, 1994) Vol. 1, IAEA, Vienna (1995) 415.

[169] SÖLDNER, F.X. et al., Plasma Physics and Controlled Nuclear Fusion Research 1994, (Proc. 15th Int. Conf. Seville, 1994) Vol. 1, IAEA, Vienna (1995) 423.

[170] ITOH, S., et al., Fusion Energy 1996, (Proc. 16th. Int. Conf., Montréal, 1996) Vol. 3, IAEA, Vienna (1997) 351.

[171] KARNEY, C.F.F. and FISCH, N.J., Phys. Fluids **22** (1979) 9.

[172] EKEDAHL, A., et al., Nucl. Fusion **38** (1998) 1397.

[173] GORMEZANO, C., et al., Proc. 10th. Topical Conf. on Radio Frequency Power in Plasmas, Boston, AIP, New York (1993) 87.

[174] FISCH, N.J. and RAX, J.M., Phys. Rev. Lett. **69** (1992) 612.

[175] POST, D.E., et al., "ITER Physics ", ITER Documentation Series No. 21, IAEA, Vienna (1991).

[176] STEVENS, J.E., et al., Controlled Fusion and Plasma Physics, (Proc. 12th Euro. Conf., Budapest, 1985) Vol. 9F, Part II, European Physical Society, Geneva (1985) 192.

[177] PARLANGE, F., et al., Controlled Fusion and Plasma Physics, (Proc. 12th Euro. Conf., Budapest, 1985) Vol. 9F Part II, European Physical Society, Geneva (1985) 172

[178] SÖLDNER, F.X., et al., Phys. Rev. Lett. **57** (1986) 1137.

[179] SÖLDNER, F.X., et al., Nucl. Fusion **34** (1994) 985.

[180] VALOVIC, M., et al., Radio Frequency Heating and Current Drive of Fusion Devices, (Proc. 2nd Euro. Topical Conf., Brussels, 1998) Vol. 22A, European Physical Society, Mulhouse (1998) 217.

[181] WIJNANDS, T., et al., Nucl. Fusion **37** (1997) 777.

[182] SÖLDNER, F.X., et al., Nucl. Fusion **34** (1994) 7.

[183] IDE, S., et al., Fusion Energy 1996, (Proc. 16th. Int. Conf., Montréal, 1996) Vol. 3, IAEA, Vienna (1997) 253.

[184] SÖLDNER, F.X., Plasma Phys. Control. Fusion **39** (1997) B353.

[185] MOREAU, D., Strong Microwaves in Plasmas, (Proc. 3rd Int. Workshop, Moscow-St Petersburg, 1996) Vol. 1, A.G. Litvak (Ed.), Institute of Applied Physics, Russian Academy of Sciences (1997) 51.

[186] SÖLDNER, F.X., et al., Plasma Phys. Control. Fusion **33** (1991) 405.

[187] LALLIA, P.P., Radio Frequency Plasma Heating (Proc. 2nd Topical Conf., Lubbock) (1974) C3.

[188] BRAMBILLA, M., Nucl. Fusion **16** (1976) 47.

[189] JACQUET, P., et al., Proc. 12th. Topical Conf. on Radio Frequency Power in Plasmas, Savannah, AIP, New York (1997) 161.

[190] STEVENS, J., et al., Nucl. Fusion **21** (1981) 1259.

[191] MOREAU, D. and NGUYEN, T.K., "Couplage de l'onde lente au voisinage de la fréquence hybride basse dans les grands Tokamaks", Report EUR-CEA-FC-1246, Association Euratom-CEA, Centre d'Etudes Nucléaires de Grenoble (1984).

[192] GORMEZANO, C., et al., Nucl. Fusion **25** (1985) 419.

[193] BIBET, P., et al., Nucl. Fusion **35** (1995) 1213.

[194] TUCCILLO, A., et al., Proc. 12th Topical Conf. on Radio Frequency Power in Plasmas, Savannah, AIP, New York (1997) 121.

[195] PEYSSON, Y., et al., Fusion Energy 1996, (Proc. 16th. Int. Conf., Montréal, 1996) Vol. 3, IAEA, Vienna (1997) 265.

[196] IDE, S., et al., Plasma Phys. Control. Fusion **38** (1996) 1645.

[197] EKEDAHL, A., et al., Proc. 12th Topical Conf. on Radio Frequency Power in Plasmas, Savannah, AIP, New York (1997) 169.

[198] FUCHS, V., et al., Phys. Plasmas **3** (1996) 4023.

[199] RANTAMÄKI, K., et al., Phys. Plasmas **5** (1998) 2553.

[200] LENNHOLM, M., *et al.*, Fusion Engineering 1995, (Proc. 16th IEEE/NPSS Symp., Urbana-Champaign, 1995) Vol. 1, IEEE, Piscataway (1996) 754.

[201] JT60 TEAM, Plasma Phys. Control. Fusion **32** (1990) 853.

[202] SÖLDNER, F.X., et al., Proc. 1998 Int. Congress on Plasma Physics & 25th Euro Conf. on Controlled Fusion and Plasma Physics, (Prague, 1998) Vol. 22C, European Physical Society, Mulhouse (1998) 1190.

[203] PILIYA, A.D. and SAVELIEV, A.N., Proc. 1998 Int. Congress on Plasma Physics & 25th Euro Conf. on Controlled Fusion and Plasma Physics, (Prague, 1998) Vol. 22C, European Physical Society, Mulhouse (1998) 1234.

[204] BONOLI, P.T. and ENGLADE, R.C., Phys. Fluids **29** (1986) 2937.

[205] BONOLI, P.T. and OTT, E., Phys. Fluids **25** (1982) 359.

[206] MOREAU, D., et al., Plasma Phys. Control. Fusion **31** (1989) 1895.

[207] BIZARRO, J.P. and MOREAU, D., Phys. Fluids **B5** (1993) 1227.

[208] BARANOV, Y.F., et al., Nucl. Fusion **36** (1996) 1031.

[209] PEYSSON, Y., et al., Phys. Plasmas **3** (1996) 3668.

[210] KUPFER, K., et al., Phys. Fluids **B5** (1993) 4391.

[211] KUPFER, K. and MOREAU, D., Nucl. Fusion **32** (1992) 1845.

[212] LITAUDON, X., et al., Fusion Energy 1996, (Proc. 16th. Int. Conf., Montréal, 1996) Vol. 1, IAEA, Vienna (1997) 669.

[213] FISCHER, B. et al., Controlled Fusion and Plasma Physics, (Proc. 22nd Euro. Conf., Bournemouth, 1995) Vol. 19C, Part III, European Physical Society, Geneva (1995) 361.

[214] FROISSARD, P., et al., Fusion Technology 1998, (Proc. 20th Symp., Marseille, 1998) Vol. 1 (1998) 351.

[215] JACQUINOT, J., et al., Nucl. Fusion **39** (1999) 235.

[216] OIKAWA, T., et al., "Heating and Non-inductive Current Drive by Negative-ion based NBI in JT-60U", Fusion Energy 1998, (Proc., 17th Int. Conf., Yokohama, 1998), paper IAEA-F1-CN-69/CD1/1 (to be published).

[217] USHIGUSA, K., et al., Fusion Energy 1996, (Proc. 16th Int. Conf., Montréal. 1996), Vol. 1, IAEA, Vienna (1997) 37.

[218] DE ESCH, H.P.L., et al., Fusion Eng. and Design **26** (1995), 589.

[219] DIII-D TEAM, Plasma Physics and Controlled Nuclear Fusion Research 1992, (Proc. 14th Int. Conf., Würzburg, 1992), Vol. 1, IAEA, Vienna (1993) 41.

[220] KEILHACKER, ,M., et al., Nucl. Fusion **39** (1999) 209.

[221] WESSON, J.A., *Tokamak*s, Oxford Engineering Science Series, OUP (1997) (see p223).

[222] JANEV, R.K., et al., *Elementary Processes in Hydrogen-Helium Plasmas*, Springer series on Atoms and Plasmas, Vol. 4, Springer, Berlin (1987).

[223] BOLEY, C.D., et al., Phys. Rev. Lett. **52** (1984) 534.

[224] EQUIPE TFR, Plasma Phys. Contr. Fusion **29** (1989) 2125.

[225] PARK, H.K., Nucl. Fusion **32** (1992) 1042.

[226] TOBITA, K., et al., Plasma Phys. Contr. Fusion **32** (1990) 492.

[227] VON HELLERMANN, M.G. and SUMMERS, H.P., Rev. Sci. Instrum. **63** (1992) 5132.

[228] NEMOTO. M., et al., J. Plasma Fusion Research **73** (1997) 1374.

[229] JANEV, R.K., et al., Nucl. Fusion **29** (1989) 2125.

[230] SPITZER, L., *Physics of Fully Ionized Gases*, Interscience Publishers Inc., New York, (1956).

[231] SIVUKHIN, D.V., "Coulomb collisions in a fully ionized plasma", in *Review of Plasma Physics* , Vol. 4, Consultation Bureau, New York, (1966) 88.

[232] STIX, T.H., Plasma Phys. **14** (1972) 367.

[233] OTT, W., "Neutral beam modulation for heating profile measurements", Laboratory Report IPP4/276, Max-Planck-Institut für Plasmaphysik, (May 1997).

[234] ibid [221] (see p226).

[235] LISTER, G.G., et al.., 3rd Symp. Plasma Heating in Toroidal Devices, Varenna, 1976 (ed, E. Sindoni), Editrice Compositori, Bologna (1976) 303.

[236] BUDNY, R.V., et al., Nucl. Fusion **35** (1995) 1497.

[237] HEIDBRINK, W.W., et al., Nucl. Fusion **28** (1988) 1897.

[238] SPETH, E., Rep. Prog. Phys. **52** (1989) 57.

[239] CORDEY, J.G., et al., Nucl. Fusion **15** (1975) 441.

[240] EUBANK, H., et al., Plasma Physics and Controlled Nuclear Fusion Research 1978, (Proc. 7th Int. Conf., Innsbruck, 1978), Vol. 1, IAEA Vienna (1979) 167.

[241] JARVIS, O.N., Plasma Phys. Control. Fusion **36** (1994) 209.

[242] STRACHAN, J.D., et al., Nucl. Fusion **21** (1981) 67.

[243] HENDEL, H.W., et al., J. Fusion Energy **5** (1986) 231.
[244] KIM, J., Bull. Am. Phys. Soc. **30** (1990) 1500.
[245] HEIDBRINK, W.W., Phys. Fluids **B2** (1990) 4.
[246] KASS, T., "Untersuchungen zum Verhalten hochenergetischer Ionen in magnetisch eingeschlossenen Plasmen", Laboratory Report IPP1/298, Max-Planck-Institut für Plasmaphysik, (April 1996).
[247] JET TEAM, Nucl. Fusion **32** (1992) 187.
[248] THOMPSON, E., et al., Phys. Fluids **B5** (1993) 2468.
[249] "Technical Basis for the ITER Final Design Report, Cost Review and Safety Analysis (FDR)", ITER EDA Documentation Series No. 16, IAEA, Vienna (1998).
[250] DE ESCH. H.P.L., Proc. 1998 Int. Congress on Plasma Physics & 25th Euro Conf. on Controlled Fusion and Plasma Physics, (Prague, 1998) Vol. 22C, European Physical Society, Mulhouse (1998) 1198.
[251] OHKAWA, T., Nucl. Fusion **10** (1970) 185.
[252] CORDEY, J.G., et al., Nucl. Fusion **19** (1979) 249.
[253] COHEN, R.S., et al., Phys. Rev. **80** (1950) 230.
[254] SPITZER, L. and HÄRM, L., Phys. Rev. **89** (1953) 977.
[255] CONNOR, J.W. and CORDEY, J.G., Nucl. Fusion **14** (1974) 285.
[256] START, D.F.H., et al., Plasma Phys. **22** (1979) 303.
[257] ibid [221] (see p133).
[258] ZARNSTORFF, M.C., et al., Phys. Rev. Lett. **60** (1988) 1306.
[259] CLARK, W.H.M., et al., Phys. Rev. Lett. **45** (1980) 1101.
[260] SIMONEN, T., et al., Phys. Rev. Lett. **61** (1988) 1720.
[261] CHALLIS, C.D., et al., Nucl. Fusion **29** (1989) 563.
[262] KAMADA, Y., et al., Nucl. Fusion **34** (1994) 1605.
[263] GOLDSTON, R.J., et al., J. Comput. Phys. **43** (1981) 61.
[264] MATSUOKA, M., et al., Fusion Eng. and Design **26** (1995) 59.
[265] TANI, K. and AZUMI, M., J. Computational Physics **98** (1992) 332.
[266] FOREST, C., et al., Phys. Rev. Lett. **79** (1997) 427.
[267] NISHITANI, T.., et al., Nucl. Fusion **34** (1994) 1069.
[268] SCOTT, S.D., et al., Phys Fluids **B2** (1990) 1300.
[269] BURRELL, K.H., et al., General Atomics Report GA-C20051 (May 1990).
[270] DE ESCH, H.P.L., et al., Nuclear Fusion and Plasma Heating, (Proc 17th Euro. Conf., Amsterdam, 1990) Vol. 14B, Part I, European Physical Society, Geneva (1990) 90.
[271] KALLENBACH, A., et al., Plasma Phys. Contr. Fusion **3**, (1991) 595.

[272] CONNOR, J.W., et al., Plasma Phys. Contr. Fusion **31** (1989) 1469.

[273] HINTON, F.L. and ROBERTSON, J.A., Phys. Fluids **27** (1984) 1243.

[274] ibid [221] (see p224-229).

[275] ZASTROW, K.D., et al., Nucl. Fusion **37** (1997) 257.

[276] DE ESCH, H.P.L., "Routes to Ignition in ITER by means of Neutral Beam Injection", JET Report JET-R(97)16 (1997).

[277] KOIDE, Y., et al., Phys. Plasma **4** (1997) 1623.

[278] KURIYAMA, M., et al., Fusion Engineering 1997, (Proc. 17th IEEE/NPSS Symp., San Diego, 1997) Vol. 1, IEEE, Piscataway (1998) 405.

[279] PAMELA, J., et al., Fusion Eng. and Design **26** (1995) 407.

LIST OF TABLES

Table 6.1-I: Salient Features of the Four Auxiliary Heating Systems in use on Tokamaks

Table 6.3-I: The Present ICRF Systems of Various Tokamaks

Table 6.4-I: The Present LHW Systems on Various Tokamaks

LIST OF FIGURES

FIG. 6.2-1. Comparison of predicted on-axis current drive and experimental results. The curves (marked by O and Δ) are simulations showing the influence of temperature profiles and divergence of the wave due to diffractive effects. Experimental results from T-10 and DIII-D are also shown (marked by ∇ and square box). Corrections for density profiles and Z_{eff} have been made for both experimental results and marked by the corresponding filled symbols [28].

FIG. 6.2-2. The current drive figure-of-merit for 24 MA, 6 T target plasmas with T_{e0} = 20 keV and T_{e0} = 30 keV. The figure-of-merit, $<\eta>$, is plotted against toroidal launch angle for selected frequencies between 160 and 220 GHz [28]. Note that these calculations were performed for an earlier version of the ITER EDA design, but the results are still in essence valid.

FIG. 6.3-1. Comparison of the experimental neutron rate, in a JET D-T discharge with second harmonic tritium ICRF heating alone, with simulations using PION. The two NBI pulses are diagnostic pulses for the measurement of T_i (they cause large excursions in the neutron rate because the injection energy is close to the maximum of the fusion cross-section). (From [110], Fig. 4).

FIG. 6.3-2. FWCD efficiency versus central electron temperature in both DIII-D and Tore Supra experiments: circles - L-mode on DIII-D; triangles - L-mode on Tore Supra; squares - VH-mode on DIII-D; stars - NCS L-mode on DIII-D. The lines are the lower and upper bounds of the simulations (ray-tracing code CURRAY and full-wave code ALCYON).

FIG. 6.4-1. Current drive figure of merit for LHCD in various experiments as a function of the JT60 scaling $12<T_e>/(5+Z_{eff})$ (keV). (produced by JT-60U Team).

FIG. 6.4-2. Two minute LHCD shot in Tore Supra, showing global improved confinement, LHEP regime and temperature transition:
(left) time traces for lower hybrid power, P_{LH}, plasma current, I_p, loop voltage, V_l, total thermal energy, W_{Tot}, thermal energy predicted by the ITER96L-P L-mode confinement scaling, $W_{tot,ITER96}$, central electron temperature, T_e(r/a=0), and mid-radius electron temperature, T_e(r/a=0.4);
(right) electron temperature, T_e, and safety factor, q_ψ, profiles at 2 time slices.

FIG. 6.4-3. Lower Hybrid deposition profiles for on-axis and off-axis deposition conditions in JET, as determined from Fast Electron Bremsstrahlung (FEB) measurements and ray tracing calculations.

FIG. 6.4-4. q profiles at t=500 s for simulated ohmic and LH-assisted plasma current ramp-up in ITER.

FIG. 6.4-5. Results of a simulated ITER steady-state advanced scenario showing:
(left) time traces for the plasma current, I_p, bootstrap driven current, I_{bs}, lower hybrid driven current, I_{lh} fast wave driven current, I_{fw}, lower hybrid power, P_{lh}, fast wave electron heating power, P_{fweh}, and fast wave current drive power, P_{fwcd};
(right) safety factor profiles at several time slices.

FIG. 6.5-1. Comparison of the experimental enhancement in stopping cross section with theory (shaded area). The spread in the theoretical curve reflects the range of values of plasma parameters (n_e, T_e, T_i, Z_{eff}), as well as the underlying energy dependence, which is indicated in the figure. For the individual experiments indicated, the appropriate values of T_e, T_i and Z_{eff} have been taken.

FIG. 6.5-2. Comparison of experimental data with the theoretical prediction of the post-NBI decay time of the neutron rate during and after an N-NBI pulse in JT-60U. The calculation was made with a transport code based on classical slowing-down.

FIG. 6.5-3. Interpreted non-inductive current, I_{NI}, versus sum of predicted (beam driven current + bootstrap) current, I_{bb}, for several JET pulses with co-NB and counter-NB [261]. The magnitude of the beam-driven and bootstrap currents is similar, about 250 kA, in these JET discharges.

FIG. 6.5-4. Measured and computed N-NB driven current profile in JT-60U: 2.0 MW of hydrogen N-NB (0.36 MeV) is injected into a hydrogen plasma with I_p = 0.6 MA, $n_e = 0.7 \times 10^{19}$ m^{-3}.

FIG. 6.5-5. NBI current drive efficiency η_{CD} contours for ITER: the average values are shown for each region.

FIG. 6.5-6. (a) Top: Toroidal angular frequency of C^{6+} averaged over first 50 ms after the start of strong NB heating of a JET plasma [275]. Bottom: Calculated torque density profiles for the same time interval, showing instantaneous and slowing down (collisional) torque. (b) Same as (a), but averaged from 50–100 ms after the start of NB. The slowing down (or collisional) torque is now becoming comparable to the instantaneous torque. The transformation torque has begun to appear (due to the mass of injected ions now rotating with the bulk plasma). (c) Same as (a) and (b), but averaged from 200–250 ms after the start of NB. Collisional torque is now dominant and the profile takes on the characteristic peaked shape.

FIG. 6.5-7. (a) Simulated toroidal rotation profiles during the density ramp along the route to ignition in ITER for an ELMy H-mode with 60 MW of NBI into a plasma with $n_e=6.5 \times 10^{19}$m^{-3}. Various beam energies from 125 keV to 1 MeV are simulated. (b) as in (a), but simulated during the flat-top density phase in ITER for an ELMy H-mode with 60 MW of NBI for $n_e=10^{20}$ m^{-3}

FIG. 6.5-8. Neutralization efficiency as a function of beam energy (keV/amu). The solid lines are theoretical predictions and circles show the measured values for negative deuterium ions in the JT-60U experiment [277].

AUTHORS' AFFILIATIONS

[1] JET Joint Undertaking, Abingdon OXON OX14 3EA, UK

[2] Faculty of Engineering, Okayama University, Okayama 700-8530, Japan

[3] Kurchatov Institute of Atomic Energy, Ploshchad'Akademika Kurchatova 46, Moscow 123182, Russia

[4] Japan Atomic Energy Reseach Institute (JAERI), Naka Fusion Research Establishment, 801-1 Mukouyama Naka-machi, Naka-gun, Ibaraki-ken, 311-01, Japan

[5] Lawrence Livermore National Laboratory, P.O. Box 808, Livermore, CA 94550, USA

[6] Ente Nazionale per l'Energia Atomica (ENEA), Via Enrico Fermi 27, C.P. 65, I-00044, Frascati, Italy

[7] Institute for Fusion Studies, University of Texas at Austin, Austin, Texas, USA

[8] Princeton Plasma Physics Laboratory (PPPL), Princeton University, P.O. Box 451, Princeton, NJ 08543, USA

[9] Ecole Royale Militaire/Koninklijke Militaire School, 30 av. de la Renaissance, B-1000 Brussels, Belgium

[10] Centre d'Etudes de Cadarache, CEA - DRFC/STID, B.P. No. 1, F-13108 Saint Paul-lez-Durance, France

[11] European Commission, Rue de la Loi 200, B-1049 Brussels, Belgium

[12] Oak Ridge National Laboratory, P.O. Box 2009, Oak Ridge, TN 37831, USA

[13] Centre Canadien de Fusion Magnetique, Varennes, Que., Canada

[14] Lodestar Research Corporation, Boulder, Colorado 80301, USA

[15] The NET Team, c/o Max-Planck-Institut für Plasmaphysik, Boltzmannstr. 2, D-85748 Garching, Germany

[16] CompX, 12839 Via Grimaldi, Del Mar, CA, USA 92014

[17] VTT Energy, P.O. Box 1606, FIN-02044 VTT, Finland

[18] Alfvén Laboratory, Royal Institute of Technology, S-10044 Stockholm, Sweden

[19] UKAEA Fusion, Culham Science Centre, Abingdon, Oxon OX14 3DB, UK

[20] General Atomics, P.O. Box 85608, San Diego, CA 92186-5608, USA

[21] Max-Planck-Institut für Plasmaphysik, Boltzmannstr. 2, D-85748 Garching, Germany

[22] Intevac, Inc. Santa Clara, California USA 95054

[23] FOM-Instituut voor Plasmafysica "Rijnhuizen", Edisonbaan 14, Postbus 1207, NL-3430 BE Nieuwegein

[24] Institut für Plasmaforschung, University of Stuttgart, Pfaffenwladring 31, D-70569 Stuttgart, Germany

[25] Plasma Physics Laboratory, Kyoto University, Gokasho, Uji, KYOTO 611, Japan

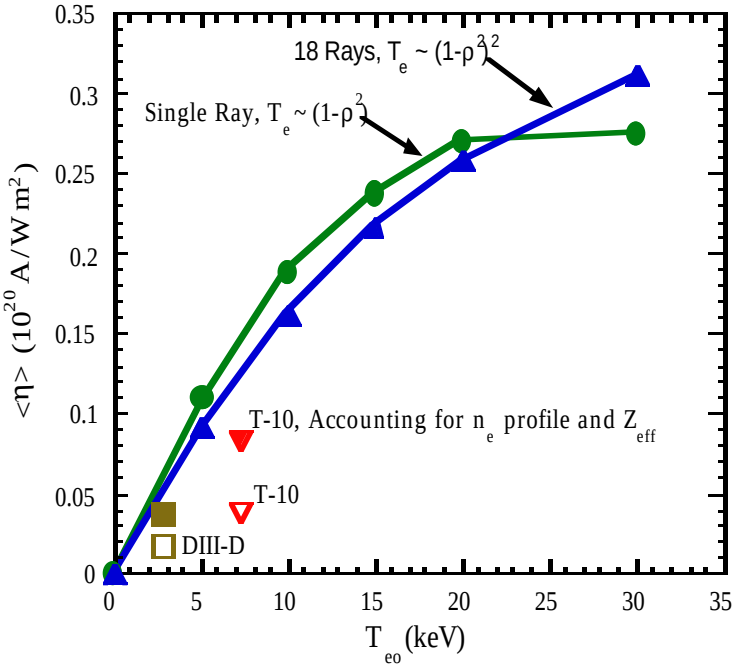

FIG. 6.2-1. Comparison of predicted on-axis current drive and experimental results. The curves (marked by O and Δ) are simulations showing the influence of temperature profiles and divergence of the wave due to diffractive effects. Experimental results from T-10 and DIII-D are also shown (marked by ∇ and square box). Corrections for density profiles and Z_{eff} have been made for both experimental results and marked by the corresponding filled symbols [28].

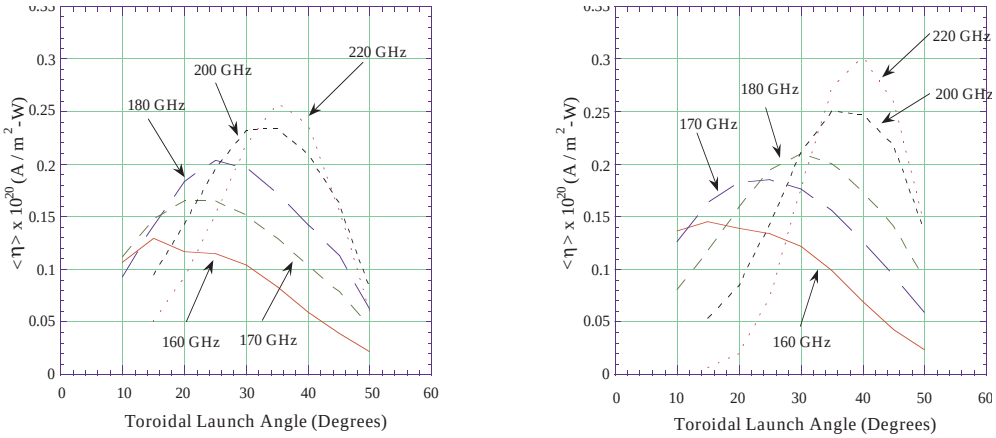

FIG. 6.2-2. The current drive figure-of-merit for 24 MA, 6 T target plasmas with T_{e0} = 20 keV and T_{e0} = 30 keV. The figure-of-merit, $\langle\eta\rangle$, is plotted against toroidal launch angle for selected frequencies between 160 and 220 GHz [28]. Note that these calculations were performed for an earlier version of the ITER EDA design, but the results are still in essence valid.

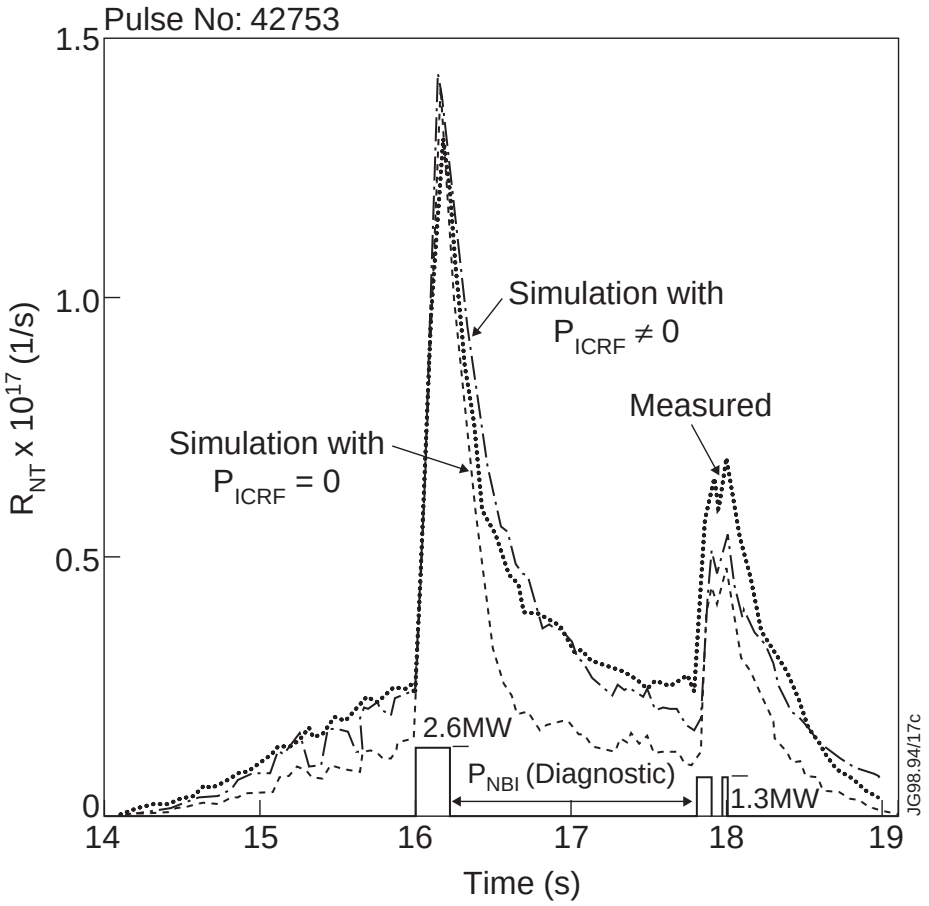

FIG. 6.3-1. Comparison of the experimental neutron rate, in a JET D-T discharge with second harmonic tritium ICRF heating alone, with simulations using PION. The two NBI pulses are diagnostic pulses for the measurement of T_i (they cause large excursions in the neutron rate because the injection energy is close to the maximum of the fusion cross-section). (From [110], Fig. 4).

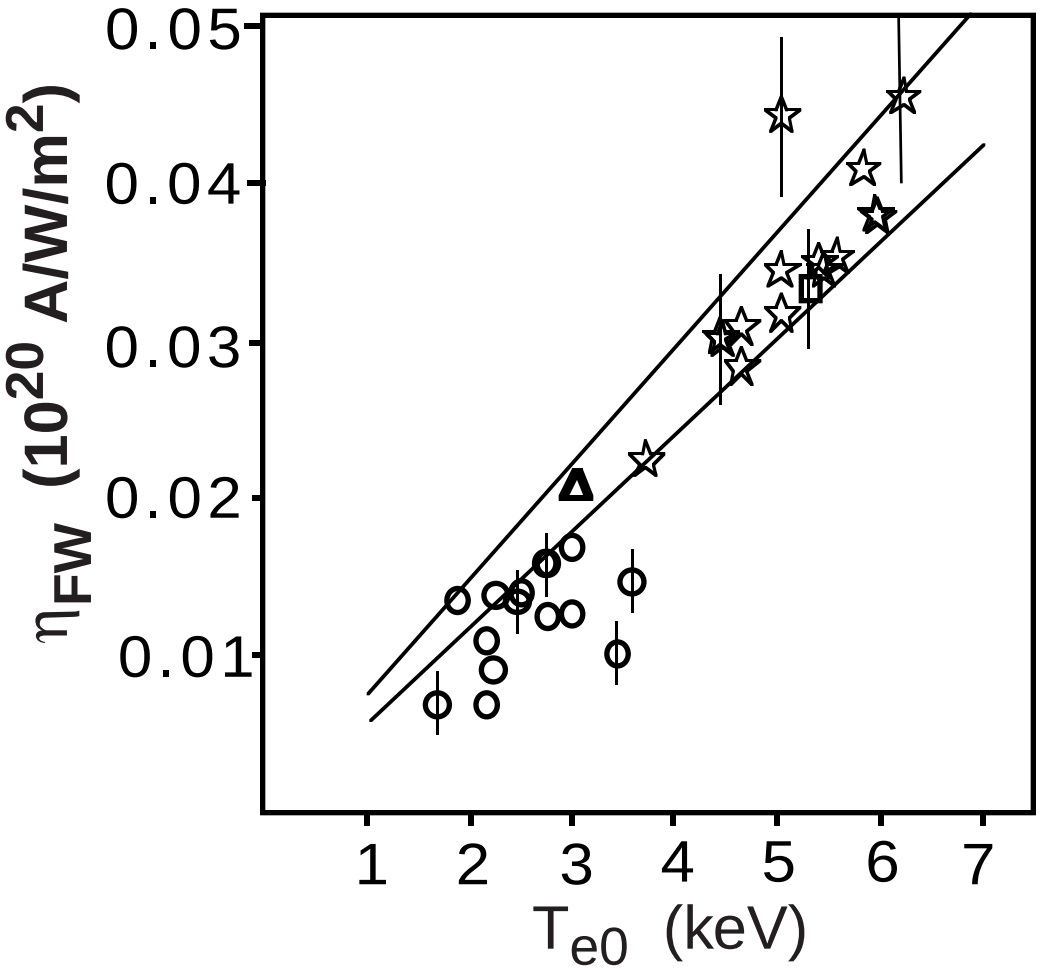

FIG. 6.3-2. FWCD efficiency versus central electron temperature in both DIII-D and Tore Supra experiments: circles - L-mode on DIII-D; triangles - L-mode on Tore Supra; squares - VH-mode on DIII-D; stars - NCS L-mode on DIII-D. The lines are the lower and upper bounds of the simulations (ray-tracing code CURRAY and full-wave code ALCYON).

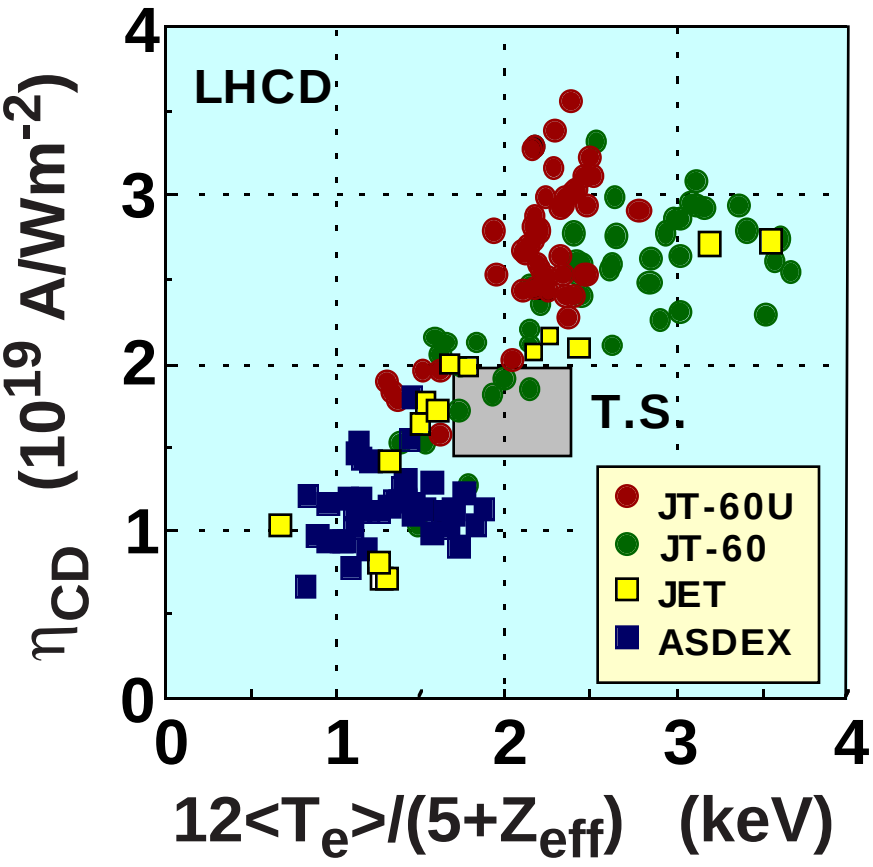

FIG. 6.4-1. Current drive figure of merit for LHCD in various experiments as a function of the JT60 scaling $12<T_e>/(5+Z_{eff})$ (keV). (produced by JT-60U Team).

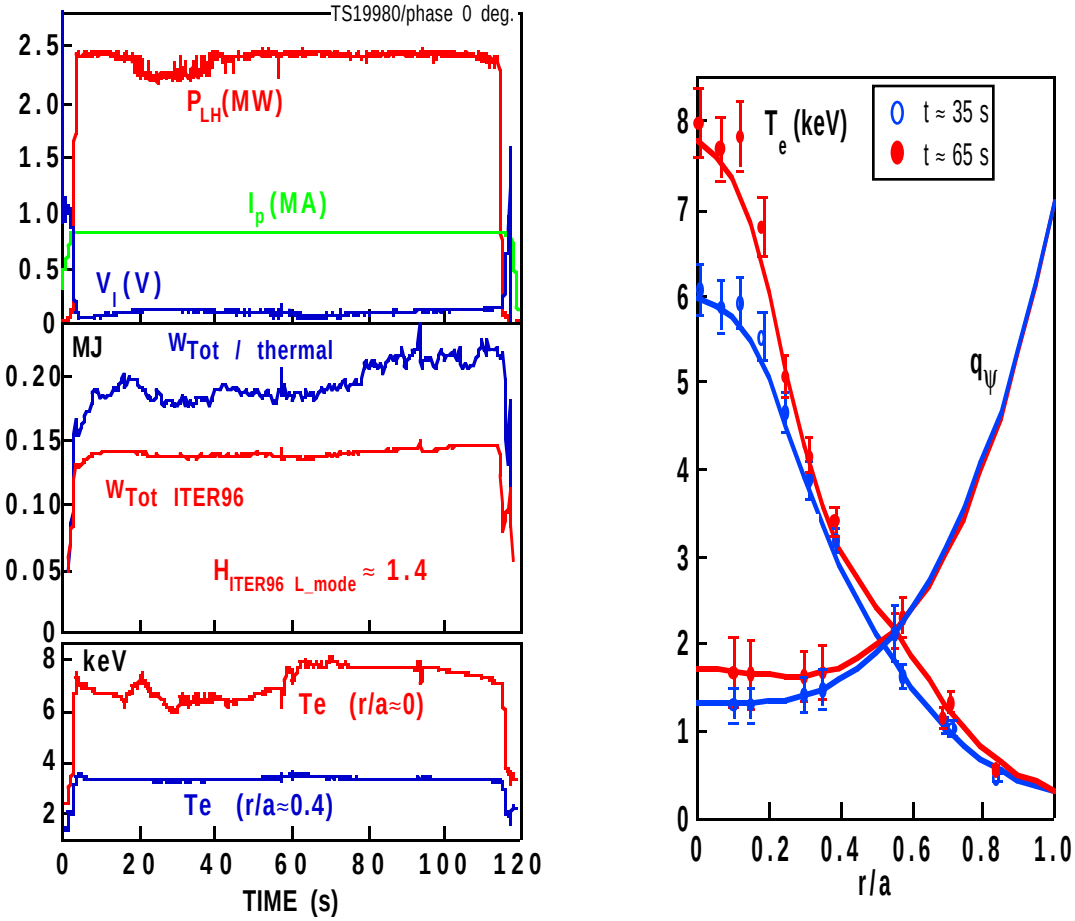

FIG. 6.4-2. Two minute LHCD shot in Tore Supra, showing global improved confinement, LHEP regime and temperature transition:

(left) time traces for lower hybrid power, P_{LH}, plasma current, I_p, loop voltage, V_l, total thermal energy, W_{Tot}, thermal energy predicted by the ITER96L-P L-mode confinement scaling, $W_{tot,ITER96}$, central electron temperature, T_e(r/a=0), and mid-radius electron temperature, T_e(r/a=0.4);

(right) electron temperature, T_e, and safety factor, q_ψ, profiles at 2 time slices.

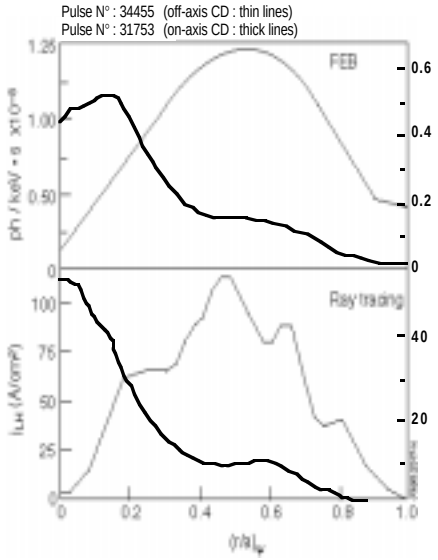

FIG. 6.4-3. Lower Hybrid deposition profiles for on-axis and off-axis deposition conditions in JET, as determined from Fast Electron Bremsstrahlung (FEB) measurements and ray tracing calculations.

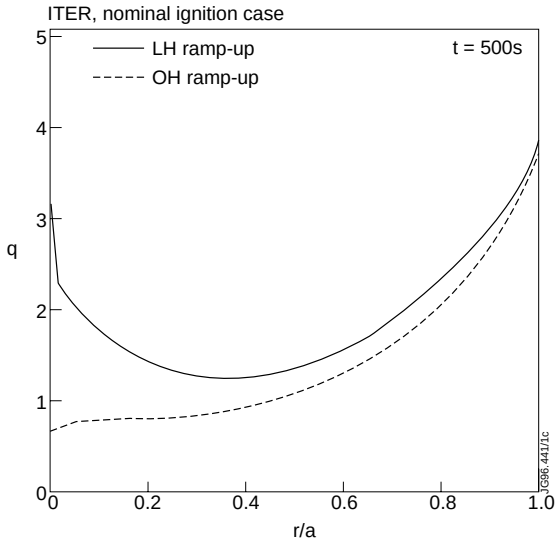

FIG. 6.4-4. q profiles at t=500 s for simulated ohmic and LH-assisted plasma current ramp-up in ITER.

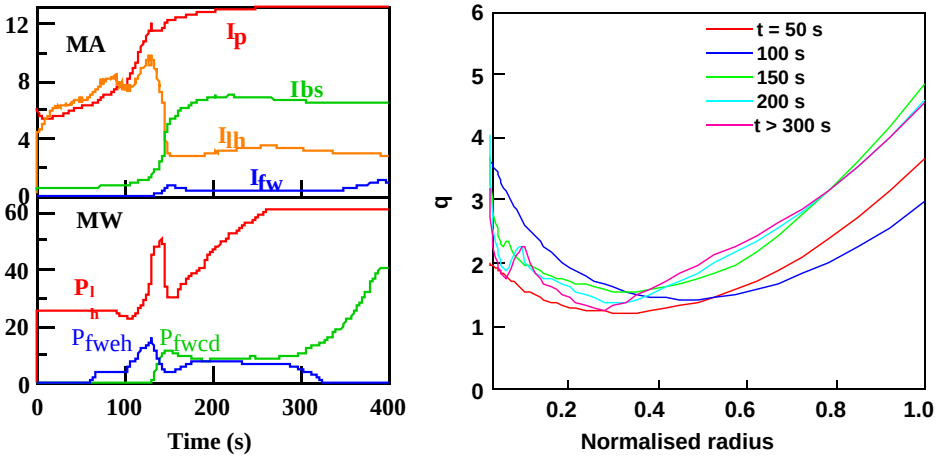

FIG. 6.4-5. Results of a simulated ITER steady-state advanced scenario showing:
(left) time traces for the plasma current, I_p, bootstrap driven current, I_{bs}, lower hybrid driven current, I_{lh} fast wave driven current, I_{fw}, lower hybrid power, P_{lh}, fast wave electron heating power, P_{fweh}, and fast wave current drive power, P_{fwcd};
(right) safety factor profiles at several time slices.

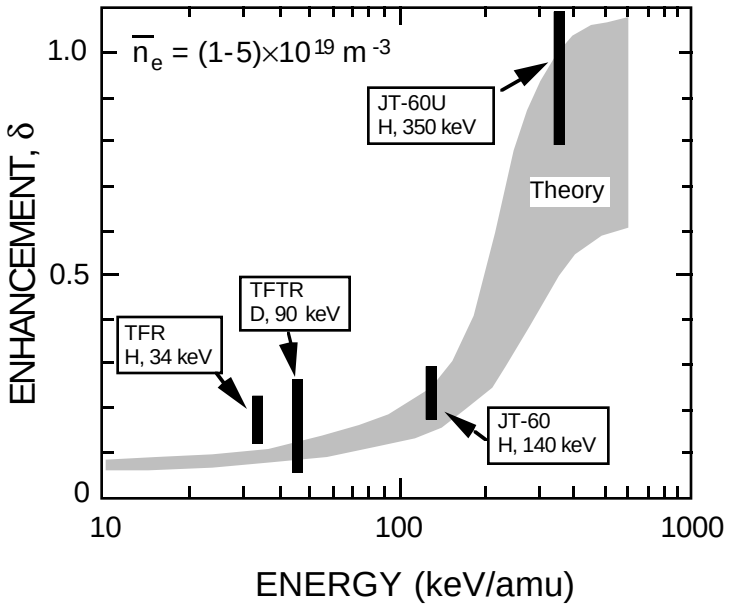

FIG. 6.5-1. Comparison of the experimental enhancement in stopping cross-section with theory (shaded area). The spread in the theoretical curve reflects the range of values of plasma parameters (n_e, T_e, T_i, Z_{eff}), as well as the underlying energy dependence, which is indicated in the figure. For the individual experiments indicated, the appropriate values of T_e, T_i and Z_{eff} have been taken.

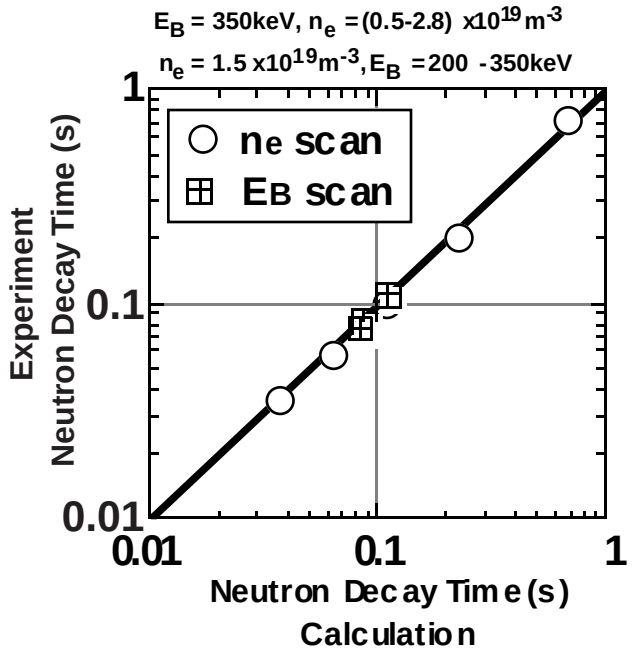

FIG. 6.5-2. Comparison of experimental data with the theoretical prediction of the post-NBI decay time of the neutron rate during and after an N-NBI pulse in JT-60U. The calculation was made with a transport code based on classical slowing-down.

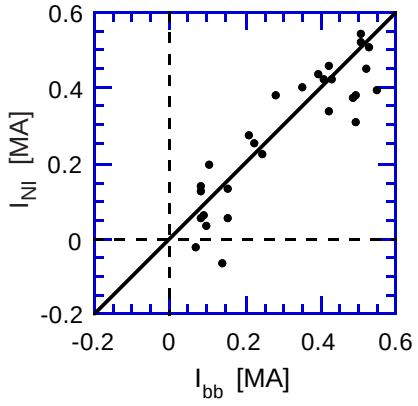

FIG. 6.5-3. Interpreted non-inductive current, I_{NI}, versus sum of predicted (beam driven current + bootstrap) current, I_{bb}, for several JET pulses with co-NB and counter-NB [261]. The magnitude of the beam-driven and bootstrap currents is similar, about 250 kA, in these JET discharges.

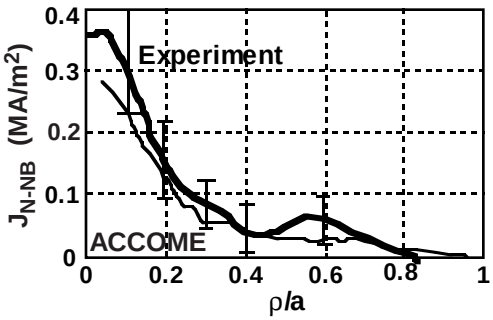

FIG. 6.5-4. Measured and computed N-NB driven current profile in JT-60U: 2.0 MW of hydrogen N-NB (0.36 MeV) is injected into a hydrogen plasma with I_p = 0.6 MA, $n_e = 0.7 \times 10^{19}$ m^{-3}.

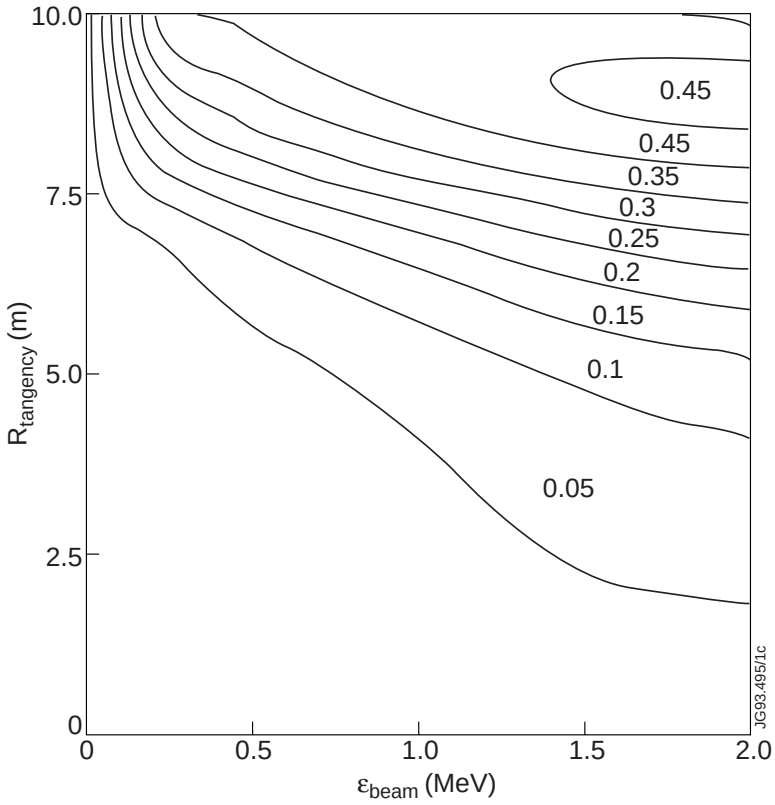

Fig. 6.5-5. NBI current drive efficiency η_{CD} contours for ITER: the average values are shown for each region.

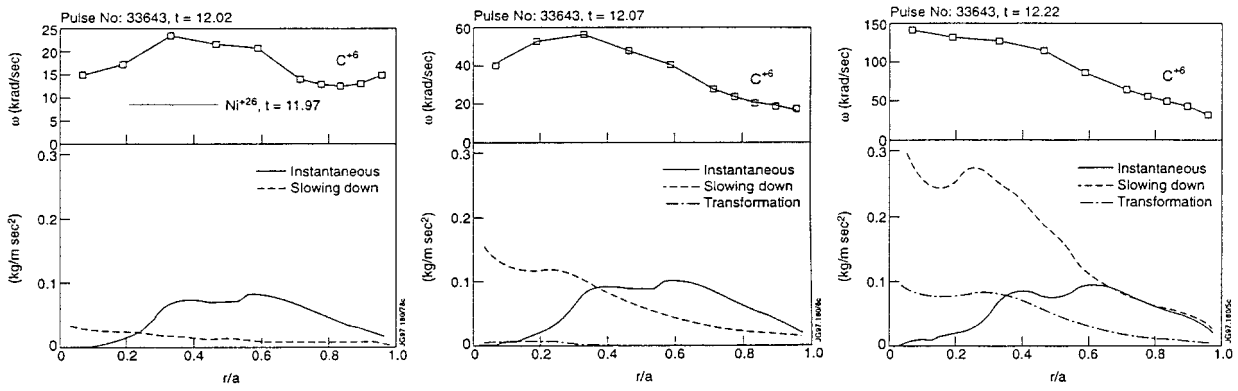

(a) (b) (c)

FIG. 6.5-6. (a) Top: Toroidal angular frequency of C^{6+} averaged over first 50 ms after the start of strong NB heating of a JET plasma [275]. Bottom: Calculated torque density profiles for the same time interval, showing instantaneous and slowing down (collisional) torque. (b) Same as (a), but averaged from 50–100 ms after the start of NB. The slowing down (or collisional) torque is now becoming comparable to the instantaneous torque. The transformation torque has begun to appear (due to the mass of injected ions now rotating with the bulk plasma). (c) Same as (a) and (b), but averaged from 200–250 ms after the start of NB. Collisional torque is now dominant and the profile takes on the characteristic peaked shape.

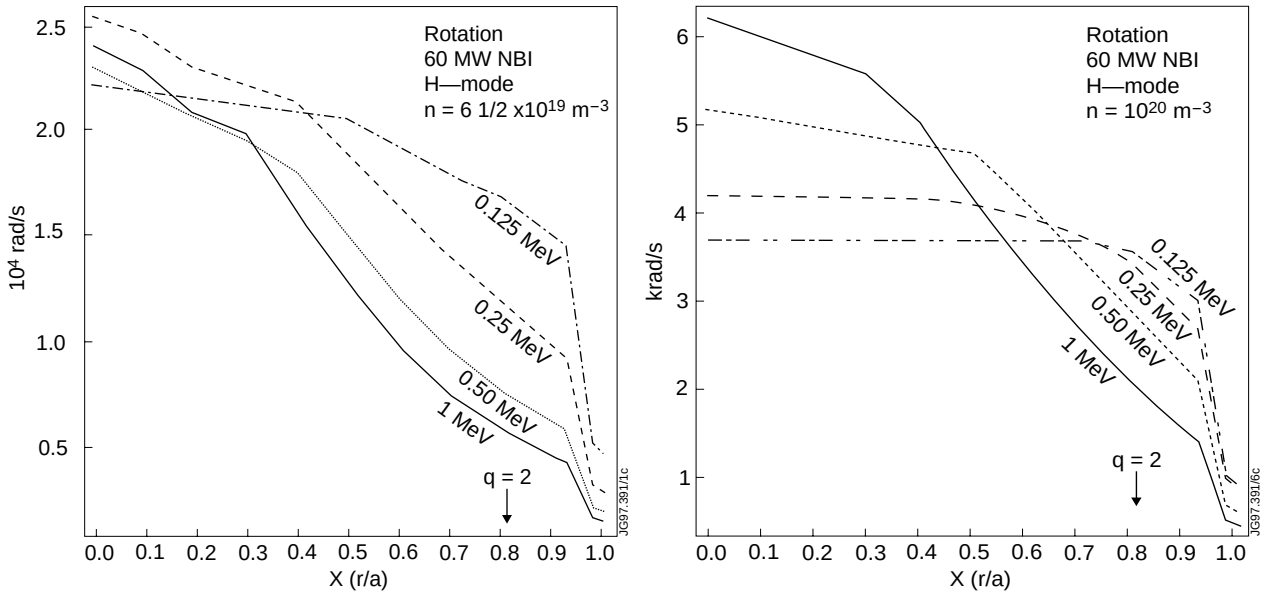

Fig. 6.5-7. (a) Simulated toroidal rotation profiles during the density ramp along the route to ignition in ITER for an ELMy H-mode with 60 MW of NBI into a plasma with $n_e=6.5 \times 10^{19} m^{-3}$. Various beam energies from 125 keV to 1 MeV are simulated. (b) as in (a), but simulated during the flat-top density phase in ITER for an ELMy H-mode with 60 MW of NBI for $n_e=10^{20}\ m^{-3}$

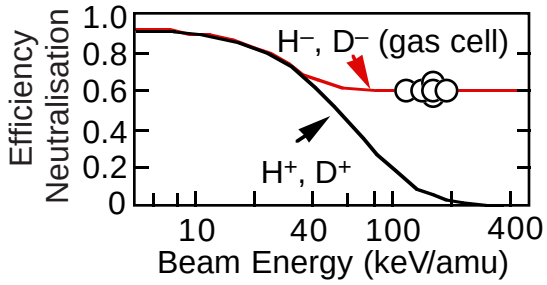

FIG. 6.5-8. Neutralization efficiency as a function of beam energy (keV/amu). The solid lines are theoretical predictions and circles show the measured values for negative deuterium ions in the JT-60U experiment [277].